

Prototype Studies and Simulations for a Forward Si-W Calorimeter at the Large Hadron Collider

A catalogue record is available from the Utrecht University Library.

ISBN: 978-90-393-6911-1

Copyright © 2017 by Hongkai Wang

All rights reserved. No part of this book may be reproduced, stored in a database or retrieval system, or published, in any form or in any way, electronically, mechanically, by print, photo-print, microfilm or any other means without prior written permission of the author.

Cover design: Hongkai Wang

Typeset using L^AT_EX

Printing: Ridderprint BV | www.ridderprint.nl.

Prototype Studies and Simulations for a Forward Si-W Calorimeter at the Large Hadron Collider

Prototype Studies en Simulaties van een Voorwaardse Si-W Calorimeter bij de Large Hadron Collider

(met een samenvatting in het Nederlands)

Proefschrift

ter verkrijging van de graad van doctor aan de Universiteit Utrecht op gezag van de rector magnificus, prof. dr. G.J. van der Zwaan, ingevolge het besluit van het college voor promoties in het openbaar te verdedigen op maandag 15 januari 2018 des middags te 2.30 uur

door

Hongkai Wang

geboren op 4 november 1987 te Shanxi, Volksrepubliek China

Promotor: Prof. dr. T. Peitzmann

Copromotoren: Dr. ir. G. J. L. Nooren
Dr. ir. M. van Leeuwen

The research was accomplished with financial support by the China Scholarship Council(CSC).

Contents

Contents	I
1 Introduction	1
1.1 Heavy Ion Physics	1
1.2 Quark Gluon Plasma	2
1.3 Gluon Saturation	3
1.4 Probes of the Initial and Early States of Nuclear Collisions . .	5
1.4.1 Direct photons	5
1.4.2 Quarkonium	7
1.5 ALICE Experiment	7
1.6 Proposed Forward Calorimeter	9
1.6.1 FoCal-E	9
1.6.2 FoCal-H	10
1.7 Summary of Chapters	12
2 FoCal Prototype	13
2.1 Introduction	13
2.2 Calorimetry	13
2.2.1 Properties of electromagnetic shower	14
2.2.2 Properties of hadronic shower	15
2.3 FoCal Prototype Design	16
2.3.1 General design	17
2.3.2 MIMOSA sensor	18
2.4 Data Acquisition System	19
2.4.1 Data read out	19
2.4.2 Software	20
2.5 Cosmic Setup	21

2.6	Beam Test Setup	22
2.6.1	DESY beam test setup	23
2.6.2	CERN beam test setup	23
2.7	Data Collection and Statistics	24
2.7.1	Beam test data statistics	24
2.7.2	Track statistics	25
3	Analysis Methodology	27
3.1	Introduction	27
3.2	Coordinate System	27
3.3	Pixel Mask and Noise Level	29
3.4	Track Reconstruction	30
3.4.1	Tracking algorithm	31
3.5	Alignment	32
3.5.1	Alignment based on residuals	32
3.5.2	Algorithm	33
3.6	Shower Position Determination	34
3.7	Inclination Correction	36
3.8	Sensor Calibration and Dead Zone Correction	37
3.9	Parameters for MC Simulations	39
3.9.1	Primary particles	39
3.9.2	Shower position definition	40
3.9.3	Charge sharing model	40
3.9.4	Noise	41
3.9.5	Misaligned sensors in simulation	41
4	MIP Analysis	43
4.1	Introduction	43
4.2	Alignment Verification in the Simulation	43
4.2.1	Track selection	45
4.2.2	Residuals	45
4.2.3	Alignment accuracy	47
4.3	Alignment Verification with Cosmic Muons	48
4.3.1	Track Selection	48
4.3.2	Sensor geometry	50
4.3.3	Alignment parameters	50
4.3.4	Residuals	51

4.4	Alignment Verification with Pions	54
4.5	Inclination of the Beam	56
4.6	Multiple Scattering	57
4.7	Sensor Efficiency Measurements	59
4.7.1	Effect of non-active areas	59
4.7.2	Secondary particles	60
5	Shower Analysis	63
5.1	Introduction	63
5.2	Shower Position Reconstruction	63
5.2.1	Parameter optimization	64
5.2.2	Reconstruction quality	67
5.3	e/π Separation	69
5.3.1	Pion contamination in test beam	70
5.3.2	Longitudinal parameters	72
5.3.3	Transverse parameters	74
5.3.4	Determination of separation parameters	79
5.3.5	Separation power verification	85
5.4	Calibration Optimization	87
5.4.1	Motivation of optimization	87
5.4.2	Optimization procedure	89
5.4.3	Calibration quality	90
6	Results and Discussion	93
6.1	Introduction	93
6.2	Measured Sensor Efficiency	93
6.3	Detector Response	94
6.4	Linearity and Energy Resolution	95
6.5	e/π Separation	98
6.6	Shower Position Resolution	101
7	Quarkonia Measurements with FoCal	105
7.1	Introduction	105
7.2	Simulation Situation	106
7.2.1	Detector construction	106
7.2.2	Clustering and shower reconstruction	106
7.3	Expected Quarkonia Yield	107

7.3.1	Quarkonia production	108
7.3.2	Branching ratio	109
7.3.3	Glauber model scaling	109
7.3.4	Quarkonia yields	109
7.4	Background Estimate	110
7.5	Quarkonia Performance	112
8	Conclusion and Outlook	115
8.1	Conclusion and discussion	115
8.2	Outlook	117
	Appendix A	123
	Nederlandse Samenvatting	126
	Acknowledgments	129
	Curriculum Vitae	131

Chapter 1

Introduction

1.1 Heavy Ion Physics

The key feature of heavy ion collisions is that a large amount of energy is deposited in a small space and short time scale. At CERN LHC, heavy ions can be accelerated to 3 TeV per nucleon in the centre of mass system. For Pb-Pb collisions, the total energy in the centre of mass system can reach up to 1262 TeV [1, 2].

The first question for such high energy density is, how does the energy distribute in the system. From the results of the experiments conducted in the past decades, the A-A collision is inelastic, in other words, inelastic processes play a significant part in the total cross section. In a nucleon-nucleon collisions, both colliding nucleons lose about half of the energy after colliding. This part of the energy is deposited in the small collision volume and will be used to produce new particles, e.g π . The A-A collision system consists of a large number of nucleon-nucleon collisions. The total energy deposition can be seen as the superposition of the nucleon-nucleon collision systems. The more collisions take place, the higher the energy deposition in this region. Moreover, due to Lorentz contraction, the nuclei appear very thin such that to make the all the nucleon-nucleon collisions take place in a small volume. Considerable energy will be instantaneously deposited in a small volume to make the energy density to be several GeV/fm^3 [3]. It can help to transform the quarks and gluons into a new state called *Quark Gluon Plasma* (QGP). This is the major topic of heavy ion physics today. It will be discussed in the following section.

1.2 Quark Gluon Plasma

Matter at low energy densities is composed of neutrons, protons and electrons. If the temperature of the system is increased, it will produce light strongly interacting particles such as pions. As we know, protons and neutrons consist of quarks and gluons. With the increase of the energy density, protons and neutrons and other particles overlap. Above a certain critical temperature, their constituents can freely roam without being confined inside hadrons. [4] At this energy density, the status of the system is a new state of matter which is called *Quark Gluon Plasma* (QGP). As the energy density, and consequently the temperature, get very large, the coupling strength is reduced in this state.

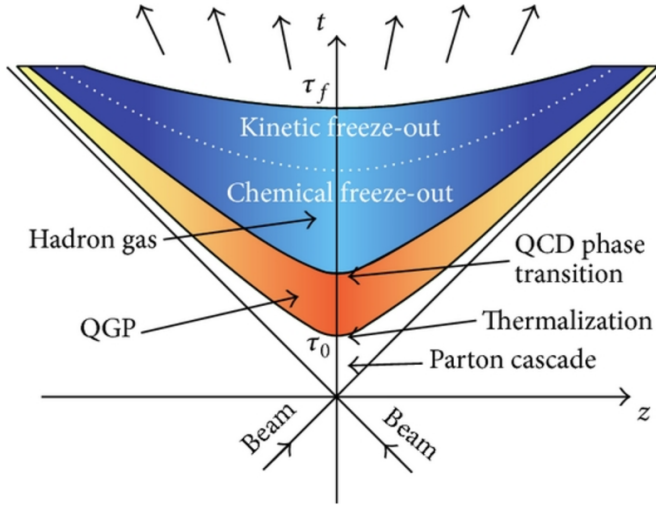


Figure. 1.1: Scheme of QGP transition

According to the calculation of lattice QCD, the formation of QGP matter occurs if critical temperature ($T_c \approx 173 \pm 15$ MeV) and critical energy density ($\epsilon \approx 0.7 \pm 0.3$ GeV/fm³) are reached. Figure 1.1 shows the evolution of the heavy-ion collision in the case of QGP formation. The different phases can be listed as follows:

- **Pre-equilibrium** ($t \lesssim 1$ fm/c): partons scatter among each other and give rise to an abundant production of quarks and gluons. High transverse momentum particles ($p_T \gg 1$ GeV/c) are produced at this stage. A large quantity of photons is also produced, such as direct photons, real or virtual.

- **Thermalization** ($t \sim 1$ to 10 fm/c): elastic and inelastic interactions between partons in QGP lead to the thermalization. Inelastic interactions can modify the flavour composition of particles. Due to its internal pressure, the system rapidly expands. While expanding, the system begins to convert into hadron gas, which leads to a mixed phase.
- **Hadronization** ($t \sim 20$ fm/c): during its expansion, the system cools down. When it reaches again the critical energy density, the hadronization begins and quarks and gluons of the QGP matter form new hadrons. There are two possible reaction mechanisms for hadronization: fragmentation i.e. when a high p_T parton fragments in lower p_T hadrons and coalescence that involves partons with lower momenta which combines to form larger p_T hadrons.
- **Freeze-out**: when the mean distance between the hadrons becomes greater than the range of inelastic collisions. At this stage, inelastic collisions cease, thus fix the chemical abundances of particles (chemical freeze-out), which from this moment can only be changed as a result of particle decays. After the chemical freeze-out, particles continue to interact through elastic collisions until their mean free path is larger than the size of the system. The system is so dilute that the elastic collisions also cease (kinetic freeze-out).

1.3 Gluon Saturation

The yield of produced particles in the final state has a relatively trivial dependence on the number of particles available in the initial state before the collisions. Thus it is important for the interpretation of observables in heavy-ion collisions to understand the state of the constituents of the incoming nuclei as precisely as possible.

Quarks and gluons are the constituents of hadrons. Each of them can carry a varying fraction of the momentum of the hadron. This is usually quantified via the variable x introduced by Bjorken:

$$x = \frac{p_{\text{constituent}}}{p_{\text{hadron}}} \quad (1.1)$$

For high beam momentum, contributions from smaller values of x become important.

The different contributions of the constituents are usually described by the parton distribution functions, which give the probability to find a given parton

(quark or gluon) inside the hadron with a certain momentum fraction x . As an example, the gluon density is given by $xG(x, Q^2)$.

Figure.1.2 shows examples of parton distribution functions. One can see that the gluon density rises rapidly at small x . The density depends on the momentum transfer Q^2 in the collisions, and the small- x components increase with increasing Q^2 , which means the low momentum gluon density grows when the energy of the hadron increases. While for moderate values of x and Q^2 the dependence on Q^2 is described by linear QCD evolution (DGLAP), for very small values of x non-linear effects should become important, and DGLAP evolution may no longer apply. The so called *gluon saturation* or *color glass condensate* takes place when the gluon density $\rho \sim xG(x, Q^2)/\pi r^2$ times the gluon fusion cross section is greater than unity. This leads to the expectation that gluon saturation is reached when Q is less than the saturation scale Q_s given by [5, 11–13]

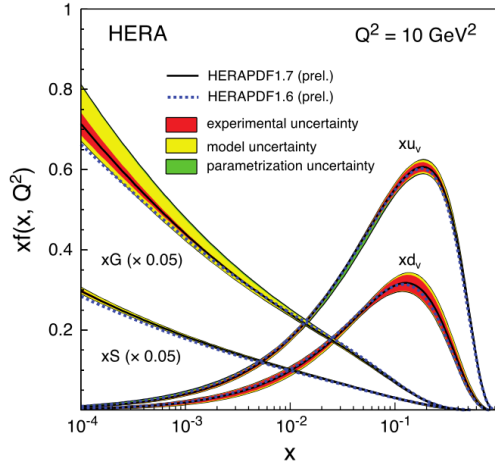


Figure. 1.2: Gluon density as a function of x

$$Q_s^2 \sim \frac{\alpha_s xG(x, Q^2)}{\pi r^2} \sim A^{\frac{1}{3}} \frac{1}{x^{0.3}} \quad (1.2)$$

However, at the small values of x relevant for gluon saturation, the parton distributions, and in particular the gluon distribution, are only poorly constrained experimentally.

1.4 Probes of the Initial and Early States of Nuclear Collisions

How can we study the initial state and the early thermal stage in these collisions? In general, one uses two different types of probes in heavy-ion collisions, soft and hard probes. While soft probes yield mostly information about the later stages of the collision, hard probes are more sensitive to the early times and the initial state. We will therefore focus on hard probes in this thesis. The main hard probes considered so far are

- High p_T electromagnetic signals (real or virtual photons)
- Heavy flavours and quarkonia ($Q\bar{Q}$ pairs)
- Jets (energetic partons)

Some of them will be discussed in detail in the following subsections.

1.4.1 Direct photons

Direct photons as electromagnetic probes can yield crucial information about the early stages of the collisions, because they are not affected by re-interactions during the later evolution of the system. One of the most interesting sources of direct photons is thermal radiation. Its spectrum contains information on the early phase of the collision, where most likely a quark-gluon plasma is produced. We will, however, not discuss this in more detail here.

More relevant for this thesis, direct photon production also contains information on the initial state parton distributions in the colliding systems, and is therefore also sensitive to effects of gluon saturation. Many experimental phenomena are consistent with the existence of gluon saturation in high energy scattering, however, no clear evidence has been found to proof it so far, which may in part be due to the limitation of the available collision energy of previous experiments.

The increase in \sqrt{s} of LHC compared with previous colliders supplies the chance to probe the PDFs in a wider range of x and Q^2 . For leading-order processes, the values of x reachable can be related to \sqrt{s} and the final state kinematic variables y and p_T via:

$$x = \frac{2p_T}{e^y \sqrt{s}} \quad (1.3)$$

However, because the gluon is uncharged and can be only constrained indirectly, the gluon PDFs have large uncertainties in the low- x and low Q^2 region.

At leading order (LO), the photons are directly produced at the parton interaction vertex, and the dominant process is quark-gluon Compton scattering. In higher order diagrams, photons can be generated from bremsstrahlung and fragmentation of one of the outgoing partons. Although the majority of prompt photons are generated in fragmentation processes, these can be suppressed by applying appropriate isolation cuts. Consequently, direct photons at large rapidity are a good probe for the gluon distributions at small x . Possible evidence for saturation can most likely best be found in a comparison of proton-nucleus with proton-proton collisions, because saturation effects should be stronger in nuclei.

In principle this is also true for Drell-Yan pair production at next-to-leading order via the virtual Compton process, however, the much smaller cross section for Drell-Yan will not allow conclusive measurements for the luminosity expected in p-Pb collisions at the LHC. This leaves direct photons measurements at forward rapidity as a promising probe of gluon saturation down to $x = 10^{-5}$. Figure 1.3 on the left shows the expected sensitivity regions in x and Q probed by DIS measurements and direct photon measurements at the LHC. Measurements of direct photons for $y > 4$ as a possible region which should be covered by measurements with the proposed Forward Calorimeter [7].

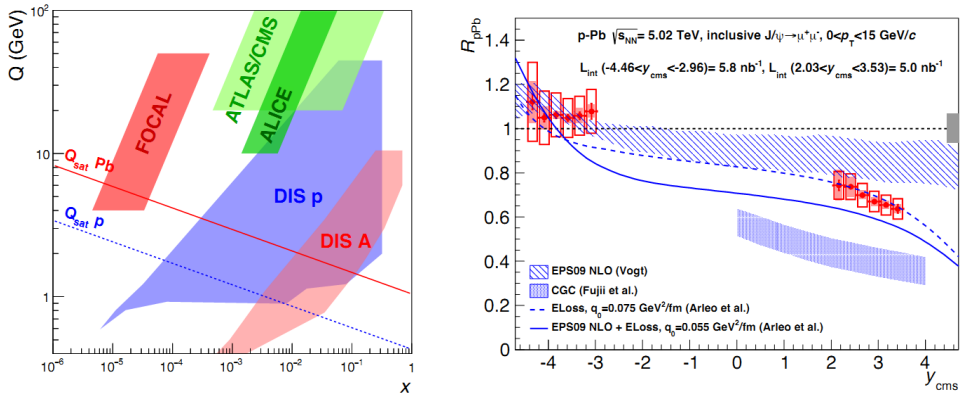


Figure. 1.3: Left: Approximate sensitivity regions in x and Q probed by DIS measurements and direct photon measurements at the LHC. The estimated saturation scale is also indicated. Right: Nuclear modification factor R_{pPb} for J/ψ as a function of y , the experimental data is shown as red symbols and are compared to several theoretical predictions

1.4.2 Quarkonium

Charm and bottom quarks are attractive as probes of the hot matter created in nucleus-nucleus collisions because their large mass prevents them from being created thermally in the hot medium. They are created only in hard processes that occur during initial scatterings. In nuclear collisions, the energy loss of heavy quarks is one of the most important signatures of the hot strongly interacting medium. In more elementary collisions, the production of heavy quarks could also serve as a probe of the parton distributions and of gluon saturation.

The use of heavy quarks and quarkonia to probe the hot matter created in nuclear collisions would be straightforward if heavy flavor production scaled with the number of nucleon-nucleon collisions, because then the initial distributions could be obtained from measurements in $p + p$ collisions. However there are a number of effects in $p + A$ collisions that modify the initial distributions of open heavy flavor and quarkonia, including shadowing. Among those so-called *cold nuclear matter* (CNM) effects, which are thought to be caused by initial state modifications, an additional effect would be gluon saturation. However, recently further nuclear modifications have been observed in $p+A$ collisions [8], which may be interpreted as modifications due to the final state. Because of this, the interpretation of hadronic observable as probes of the initial state is difficult.

Figure 1.3 right shows the suppression of forward quarkonium production as observed by ALICE (A Large Ion Collider Experiment) at CERN. This phenomenon maybe helpful to describe a series of cold nuclear matter effects, but, as discussed above, the possibility of final state modifications in $p+A$ may make final conclusions from such a measurement difficult. As a forward calorimeter, FoCal may provide the capability to measure quarkonium in the di-electron channel.

1.5 ALICE Experiment

There are four large experiments at the LHC. ATLAS and CMS are dedicated to the search of new elementary particles with very low production yields in proton-proton collision. LHCb experiment has been designed for searching for CP-violation in the B-system, while ALICE is a general purpose heavy-ion detector at the CERN LHC, which is dedicated for studies of QCD and the strong interaction. The main goal of ALICE is to study the properties of the hot and dense matter, the QGP, produced in heavy ion collisions. It will help

people to understand the physics of the deconfined state of matter which existed a few microseconds after the Big Bang, with comprehensive studies like Anisotropic Flow and Jet Quenching. The ALICE detector is optimized for tracking and identifying charged particles at midrapidity for a wide range of transverse momenta, from 100 MeV/c to 100 GeV/c. It works in a very high multiplicity environment, where the charged particle multiplicity is expected to be in the range from $dN/d\eta = 2000$ up to almost $dN/d\eta = 8000$ in central Pb–Pb collisions.

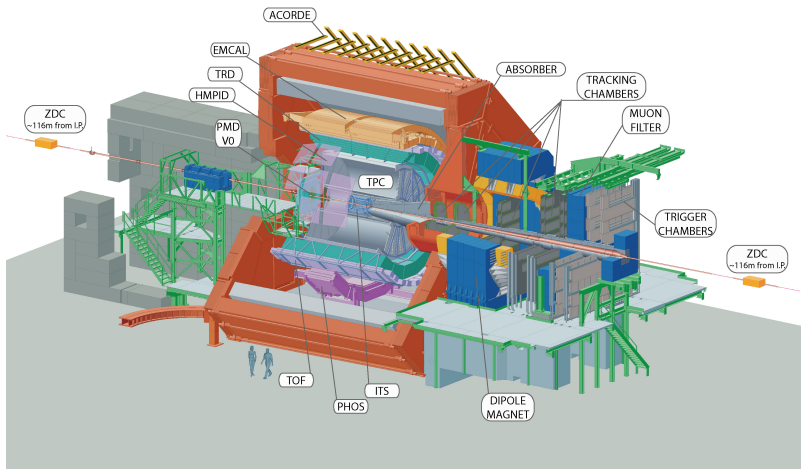


Figure. 1.4: Schematic drawing of ALICE detector, The experiments consists two main parts: Central Barrel contained in L3 magnet (red) and Muon Arm.

The dimensions of the ALICE detector are $16 \times 16 \times 26\text{m}^3$, its weight is approximately 10 000 t. The detector is shown in Figure 1.4. It consists of a central barrel detector, which is located inside a large solenoid magnet reused from the L3 experiment at LEP, with full azimuthal coverage in the pseudorapidity range $-0.9 < \eta < 0.9$ and a small angle muon spectrometer.

The ALICE detector contains many sub-detectors, from the inside to the outside, they are the Inner Tracking System (ITS), the Time-Projection Chamber (TPC), the Time-of-Flight (TOF), the Ring Imaging Cherenkov (HMPID), the Transition Radiation (TRD) detector, the electromagnetic calorimeters, which are PHOS and EMCAL, and several other detectors (ZDC, PMD, FMD, T0, V0) designed for various physics purposes [15–18].

1.6 Proposed Forward Calorimeter

A forward calorimeter (FoCal) is proposed to be built as an upgrade of the ALICE detector. It will extend the capability to perform studies of the properties of hot and dense partonic matter. The key feature of FoCal is not only to separate direct photons and decay photons from neutral pions at forward rapidity, but also provides the capability to measure jets [14].

The main purpose of FoCal is the measurement of photons, so an electromagnetic calorimeter (FoCal-E) is the most crucial part. For studies of photon isolation and for the measurement of jets, however, a hadronic section (FoCal-H) is desirable. Given the mechanical constraints an installation of FoCal-H in this location seems very difficult. The preferred option is to place the detector at $z = 7-8$ m, where both FoCal-E and FoCal-H can be installed. The construction of the FoCal-E would likely not depend on the specific location and is discussed in the following section.

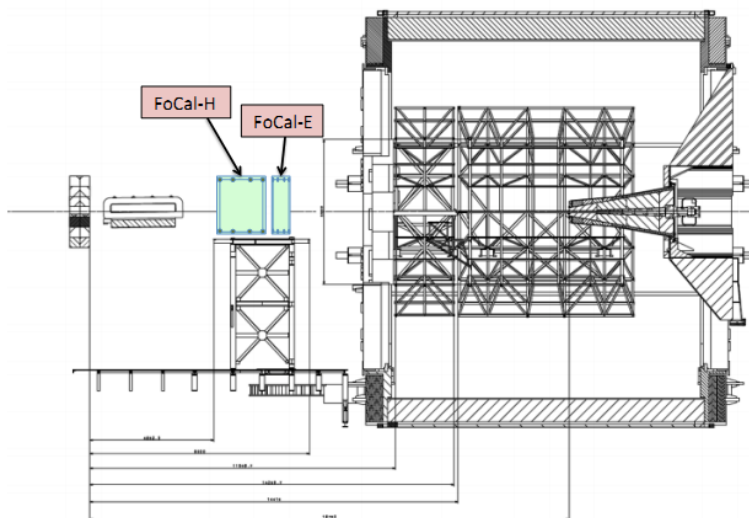


Figure. 1.5: Schematic view of the proposed installation position of FoCal in ALICE

1.6.1 FoCal-E

The proposed FoCal electromagnetic calorimeter (FoCal-E) is designed to measure photons, and in particular to separate direct photons and photons from

π^0 decay. With an inner radius of 8 cm, FoCal-E will cover 1.13 m^2 . The detector will consist of 20 - 25 physical layers. The thickness of every layer is equivalent to approximately $1 X_0$, which corresponds to 3.5 mm thick tungsten. This design will cover the full longitudinal depth of the electromagnetic shower. Different options for the mechanical structure of FoCal-E are under consideration.

The segments will consist of sampling layers of tungsten and silicon pads ($\approx 1 \text{ cm}$) summed longitudinally in towers, with a layer of silicon pixel or mini-pad ($\approx 1 \text{ mm}$) readout between longitudinal segments. The active part of the layers will be silicon sensors. There are 2 types of sensors with different granularities, in the *High Granularity Layers* (HGL) and *Low Granularity Layers* (LGL), respectively. The design is illustrated in Figure 1.6.

Low granularity layers (LGL)

The LGL consist of pad sensors, the sensor size is $8 \text{ cm} \times 8 \text{ cm}$ with a thickness of either 500 or 300 μm and with effective granularity of $1 \times 1 \text{ cm}^2$ for 64 readout pads per wafer. The sensor is attached to the tungsten with a carrier PCB mounted on top of the wafer.

High granularity layers (HGL)

The proposed effectively granularity of high granularity layers is $< 1 \text{ mm}^2$. There are several options. The main option for the sensors of the HGL are *Monolithic Active Pixel Sensors* (MAPS), which are silicon sensors based on standard CMOS process. One option is the MIMOSA series of sensors developed by IPHC [19] in Strasbourg, France. It meets the requirements for both ionizing radiation and developed front-end electronics, but the read out speed is not fast enough until now which may restrict its usage. The other option is the ALPIDE chip which is under development for the ALICE ITS upgrade [10]. With zero-suppression, the readout time decreases by the factor of 20 ($\approx 30 \mu\text{s}$), however, to be usable in the high rate environment, the bandwidth of the ALPIDE chip will have to be increased even further.

1.6.2 FoCal-H

The FoCal hadronic calorimeter (FoCal-H) is designed to improve photon isolation and jet measurement capabilities. The detector has a sampling structure and is proposed to cover the same pseudorapidity range as FoCal-E, which means it will be installed directly behind FoCal-E. For the applications

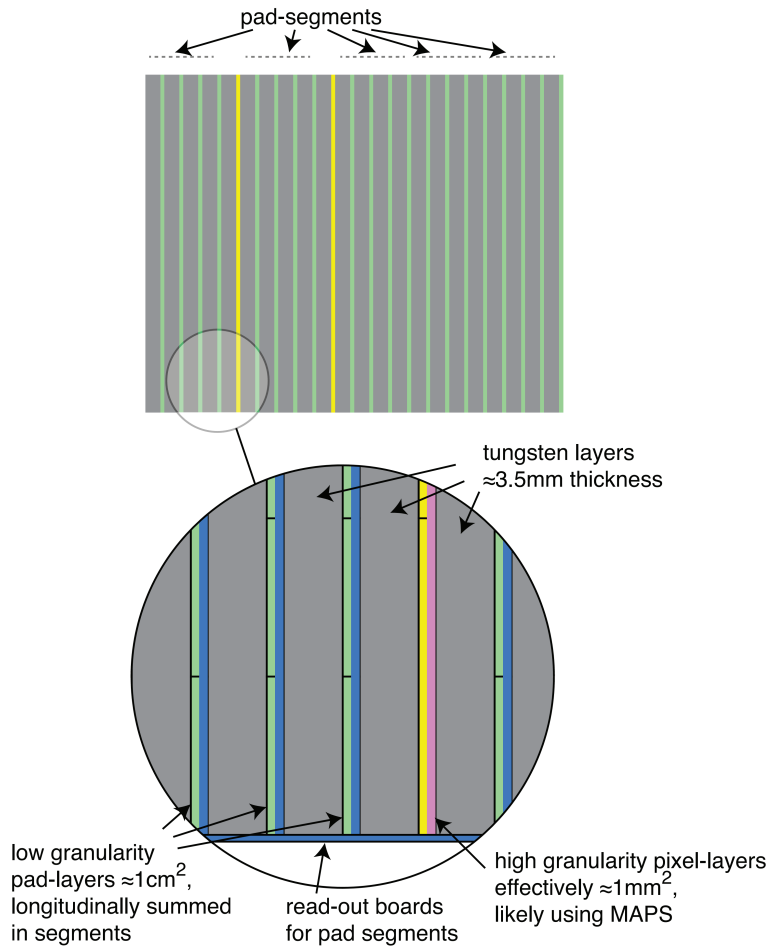


Figure. 1.6: Conceptual layout of FoCal LGL and HGL layers.

mentioned above and limited to the forward rapidity region occupied by the FoCal, the measured hadrons have very high energy and the constant term in the calorimeter resolution is expected to dominate. Pb, as a possible candidate for the absorber, has been shown to be a suitable material for E/H compensation and good hadron resolution. Therefore, the design of FoCal-H would be an Pb/scintillator sampling calorimeter.

The distance between the interaction point (IP) and FoCal-H will be around 10 m, and this leads to the requirement of the relocation of the present ALICE compensation magnet. The total length of the detector would be $8 \lambda_{had}$. The transverse area that FoCal-H will cover is the same as for FoCal-E.

1.7 Summary of Chapters

Chapter 2 first introduces the important glossary and terms frequently used in calorimetry. The design and construction of the FoCal prototype and the setup of different data collecting modes are also presented in this chapter.

Chapter 3 explains the methods and algorithms that have been used in both the MIP and shower analysis.

Chapter 4 gives the details of analysis based on minimum-ionizing particles. The two main application of the MIP data, alignment and the sensor efficiency are discussed.

Chapter 5 shows the analysis that is performed on the test beam data, both for electrons and for showering hadrons. In particular, methods for particle identification will be shown in this chapter.

Chapter 6 presents the main results obtained based on the analysis mentioned in chapters 4 and 5.

Chapter 7 discusses about the quarkonium production analysis based on full Monte-Carlo simulation with the future design of FoCal.

Chapter 8 is the last part of the thesis that draws conclusion from chapters 3 to 6 and an outlook of the future design, and discusses some of the unsolved questions of the prototype.

Chapter 2

FoCal Prototype

2.1 Introduction

As an important attempt for the further design of Forward Calorimeter in the upgrade of ALICE experiment, the properties of high granularity layers play an key role in the final design. In this chapter, the principle of calorimeter and some of information about the FoCal extremely high granularity prototype will be introduced, including the mechanics, data acquisition system, trigger system and software. The beam test setup and data collection which have been performed in DESY and CERN-SPS will be shown as well.

2.2 Calorimetry

Calorimeters are detectors in which particles to be measured are fully absorbed and their energy is transformed into a measurable quantity. With the development of high energy physics, the calorimeter has become an essential part of modern particle physics experiments. Calorimeters can be broadly divided into electromagnetic calorimeters, used to measure mainly electrons and photons through their electromagnetic interactions (bremsstrahlung, pair production), and hadronic calorimeters, used to measure mainly hadrons through their strong and electromagnetic interactions. They can be further classified according to their construction technique into sampling calorimeters and homogeneous calorimeters. Sampling calorimeters consist of alternating layers of an absorber, a dense material used to degrade the energy of the incident particle, and an active medium that provides the detectable signal. Homogeneous calorimeters, on the other hand, are built of only one type of material that performs both tasks, energy degradation and signal generation [20].

Typical calorimeters have the following features:

- They detect both charged and neutral particles.
- They have different responses to electrons, muons, and hadrons to provide particle separation power.
- They measure the incoming position of particles.
- The size of a calorimeter has to grow logarithmically for increasing energy of the incident particles.

2.2.1 Properties of electromagnetic shower

The length scale for the longitudinal development of an electromagnetic shower is determined by the radiation length, which is a characteristic of a material. It relates to the energy loss of high energy, electromagnetically interacting particles in it. It is defined as the mean distance during which a high energy electron loses $1/e$ of its energy by bremsstrahlung [29]. A parametrization of the material dependence is:

$$X_0 = \frac{716(\text{g}\cdot\text{cm}^{-2})A}{Z(Z+1)\ln(287/\sqrt{Z})} \approx 180A/Z^2(\text{g}\cdot\text{cm}^{-2}) \quad (2.1)$$

The critical energy is defined as the energy at which the collision loss rate equals the bremsstrahlung rate. The critical energy for electrons in solids is:

$$E_c = \frac{710\text{MeV}}{Z + 1.24} \quad (2.2)$$

The transverse development of an electromagnetic shower is usually described in terms of the Molière radius, which can be calculated from the radiation length. It is the mean lateral displacement from multiple coulomb scattering for electrons at the critical energy which pass through $1X_0$ of material [20].

$$R_M = \frac{21.2\text{MeV}}{E_c} X_0 \quad (2.3)$$

90% of the shower energy is contained inside a cylinder of radius R_M , and around 99% of the shower energy will be absorbed within $3.5 R_M$.

The average energy deposition of electromagnetic showers along the longitudinal depth can be expressed by the empirical formula [31]:

$$\frac{dE}{dt} = Eb \frac{(bt)^{a-1} e^{-bt}}{\Gamma(a)} \quad (2.4)$$

The average energy loss per radiation length dE/dt ($t = X/X_0$) is shown in this equation and the depth of shower maximum is $t_{max} = a - 1/b$. An approximation of the energy dependence of the shower maximum can be obtained by:

$$t_{max} \approx 1.0 \times [\ln(E/E_c) + c_i] \quad (2.5)$$

Here c_i is -0.5 for electrons and 0.5 for photons, respectively. After the shower reaches its maximum, the number of secondary particles will decrease exponentially. The depth that contains 95% energy in the absorbing materials is:

$$t_{95\%} \approx \frac{a-1}{b} + 0.08Z + 9.6 \quad (2.6)$$

2.2.2 Properties of hadronic shower

Hadronic shower development is based largely on nuclear interactions, and therefore the shower dimensions are governed by the nuclear interaction length, λ_{int} . The nuclear interaction length of an absorber medium is defined in equation 2.7, it is the average distance a high-energy hadron travels through the medium before a nuclear interaction occurs:

$$\lambda_{int} = A/(\sigma_{int}N_0\rho) \quad (2.7)$$

where A is the atomic mass, σ_{int} is the inelastic cross section, N_0 is the Avogadro number and ρ is the density of medium.

The longitudinal hadronic shower profile has some similarities to those induced by electrons and photons. It consists of an electromagnetic shower produced by π^0 and a remaining pure hadronic shower part. The longitudinal development of a hadronic shower is [21]:

$$\frac{dE}{dS} = K \left[W t^d e^{-et} + (1-W) t^f e^{-gt} \right] \quad (2.8)$$

where W is the fraction of electromagnetic components in the hadronic shower, t is the depth from the shower starting point in units of radiation length (X_0); l is also the depth, but units of nuclear interaction length (λ_{int}); d, e, f, g are parameters which can be fitted to the experimental data.

The empirical equation of the depth of the hadronic shower maximum t_{max}^h is :

$$t_{max}^h(\lambda_{int}) \approx 0.2 \times \ln E(\text{GeV}) + 0.7 \quad (2.9)$$

The depth which contains 95% of the energy is:

$$\lambda_{95\%}(\lambda_{int}) = t_{max}^h + 2.5\lambda_{hadron} \quad (2.10)$$

Here λ_{hadron} is the pure hadronic shower contribution after the shower maximum. λ_{hadron} is energy dependent, and there is an approximate relation between λ_{hadron} and λ_{int} :

$$\lambda_{hadron} \approx \lambda_{int}[E(\text{GeV})]^{0.13} \quad (2.11)$$

As mentioned, hadronic showers depend on $\lambda_{int} \propto A^{1/3}$, while in electromagnetic showers $X_0 \propto A/Z^2$, which means in a high Z medium λ_{int} is normally larger than X_0 . Therefore hadronic shower propagate much further than an electromagnetic shower in the longitudinal direction.

The effective material constants for the FoCal prototype used in this research as calculated from the proper mix of materials are listed in Table 2.1.

Table 2.1: Material properties of FoCal prototype

$X_0(\text{mm})$	L/X_0	$\lambda_{int}(\text{mm})$	L/λ_{int}	$E_c(\text{MeV})$	$R_M(\text{mm})$
4.0	28	114.3	0.98	8.107	10.5 mm

2.3 FoCal Prototype Design

In order to facilitate the design of the high granularity layers for the FoCal upgrade discussed in Section 1.6, a prototype with full *Monolithic Active Pixel*

Sensors (MAPS) has been manufactured and studied.

2.3.1 General design

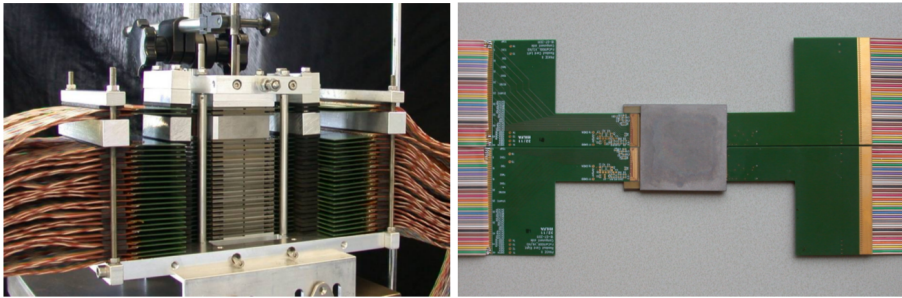


Figure. 2.1: FoCal prototype stack. Left: side view of the full stack. Right: full layer with two modules

The prototype is a sampling calorimeter with 24 sampling layers consisting of absorbers, silicon sensors, printed circuit boards (PCB) and glue (see Figure 2.1). We have compared the properties of a few possible absorber materials in Table 2.2. Out of these, tungsten, is favourable in particular due to its very small Moliere radius. The MAPS, as a unique technology for high granularity detectors in particle physics, is used as the sensitive component of the prototype.

Table 2.2: Properties of different heavy materials

Material	Density(g/cm ³)	X_0 (cm)	R_M (cm)
Cu	8.96	1.436	1.57
Pb	11.4	0.561	1.60
W	19.3	0.350	0.933

The small Moliere radius and radiation length of tungsten allow the FoCal prototype to be compact in both the transverse and longitudinal directions. The thickness of every layer is 4 mm, of which 3 mm is tungsten and the thickness is approximately equal to $0.97 X_0$. A tungsten block with 2 cm thickness is located just behind $20 X_0$, resulting in $\approx 28 X_0$ in total in the longitudinal direction of the detector. In the transverse direction, the size of the active area for every layer is approximately $4 \times 4 \text{ cm}^2$. Two identical modules, each with two sensors, are mounted in alternating orientations, with the sensors covering opposite halves

of the detector and facing each other. This design leads to a narrow gap between sensors along the x direction and an overlap along the y direction. The size of each sensor is $1.92 \times 1.92 \text{ cm}^2$.

Due to the large number of pixels in every sensor, a dedicated PCB was made. The PCB of the sensor is connected to the readout board via a flat cable.

A special cooling system for transporting the heat produced by the sensors was designed. The objective of the cooling system is not only to keep the detector working, but also to reduce thermal noise generated in the sensors.

2.3.2 MIMOSA sensor

The high granularity and thin sensitive volume provides potential capabilities to measure the position in extremely precise way. We use the MIMOSA-23 [19] pixel sensors from IPHC in Strasbourg, which allows the continuous readout of all pixels.

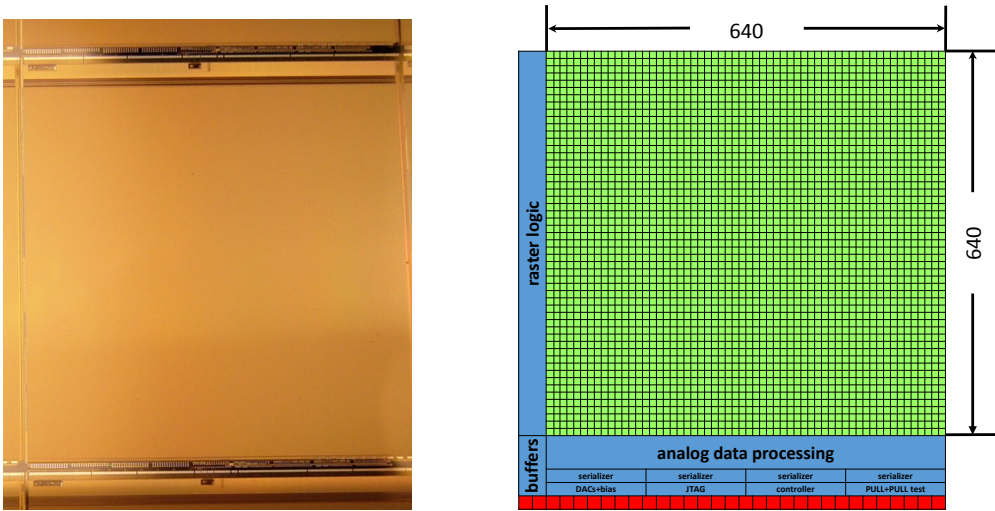


Figure. 2.2: Left: MIMOSA-23 sensor. Right: Chip architecture of MIMOSA-23

There are 96 PHASE2/MIMOSA-23 sensors with different thickness and resistivity of the epitaxial layer in the prototype. The architecture of the sensor is shown in Figure 2.2 on the right. 10 wafers with MIMOSA-23 sensors were produced for the prototype. Wafers with different resistivity and thickness of the epitaxial layer were produced to study and optimize noise levels and sensitivity. However, the yields of the thinning process were lower than expected

and a combination of sensors with different properties had to be used for the prototype. The different types of sensors can be found in Table 2.3 [37].

The full size of the sensor is $19.52 \times 20.93 \text{ mm}^2$, and $19.2 \times 19.2 \text{ mm}^2$ is taken up by the pixel matrix. The pixel matrix collects the charge deposited by a particle and converts it into digital signals (0 or 1). The size of the matrix is 640×640 , and each 160×640 pixels is grouped into a *channel*. Every channel works at 160 MHz. The readout time for every line is $1 \mu\text{s}$, every line is handled by a discriminator. All the lines are read out sequentially, which is called “rolling shutter”. The sensors are read out in parallel, which makes a total integration time of $640 \mu\text{s}$.

In order to adjust the sensitivity of every sensor, threshold voltages V_{ref1} and V_{ref2} are controlled via JTAG commands from the data acquisition computer.

Table 2.3: Type of sensors in the FoCal prototype

thickness (μm)	resistivity ($\Omega \cdot \text{cm}$)	number
15	400	46
20	400	31
14	10	19

2.4 Data Acquisition System

2.4.1 Data read out

Since a large amount of data ($\approx 8 \text{ GB/s}$) is generated by the prototype during data taking, fast data taking and transfer is required. The scheme of the read out chain can be seen in Figure 2.3, showing different components: the trigger module, the data reading module, the data interface module and the data transferring module, respectively. Their functions are as follows:

- The trigger system is responsible to indicate to the detector if there is a particle coming through the detector. It is constructed from several scintillators and NIM logic units. The trigger logic signals can provide a digital signal consisting of 15 bits to the FPGA boxes, of which 5 are trigger bits with combined coincidence signals and 10 of them are trigger counter bits.
- The data reading module handles data readout from the sensors. It consists of two parts. One is the readout PCBs attached to the MIMOSA sensors, which are responsible for reading out the data from the sensors. The other

part are the dedicated PCBs which are handling the power supply to the MIMOSA sensors. These PCBs also handle the control signals and clock synchronization between the sensors and FPGA boxes.

- The 24 layers are evenly distributed to the 2 FPGA boxes. 2 Spartan 6 XC6SLX150 and 1 Virtex 6 XC6VLX240T FPGAs are installed in each FPGA box. They are designed to interface and buffer the data between sensors, trigger logics and DAQ computers. 2 GB buffer RAM is installed in each box.
- Data is transferred via ethernet. When the buffer memory installed in the FPGA boxes are full, the data can be sent to the DAQ server according to the different setting modes. Due to the slow transferring speed of the ethernet, it takes 2 minutes to ship out the full buffer memory.

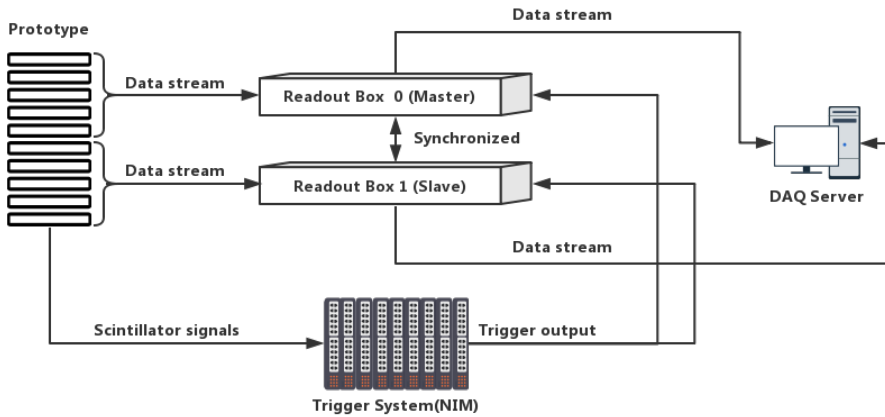


Figure. 2.3: A generalized schematic of data acquisition system.

2.4.2 Software

The two FPGA boxes are running an embedded Linux system, and the DAQ software was developed with ROOT based on C++. The data transfer protocol is using TCP/IP.

All control commands for the detector can be sent from the DAQ server through *ssh*. The permanent storage for the configuration files are the readout boxes and they are copied to the FPGA system when needed (the boxes mount the hard disk from the DAQ computer). There are 3 operating modes:

- **Beam Test Mode:** external-trigger mode, data from MIMOSA sensors fills the buffer until it is full (4 GB), then the data will be transferred to the DAQ server, and the data taking is suspended during transferring.
- **Pedestal Mode:** self-trigger mode, data can be continuously transferred to the buffer in the FPGA box. When the buffer is full, the data will be transported to the DAQ server, and the data taking is suspended during transferring.
- **Cosmic Mode:** external-trigger mode. When external trigger is received, 3 adjacent frames are shipped out immediately to the DAQ server.

2.5 Cosmic Setup

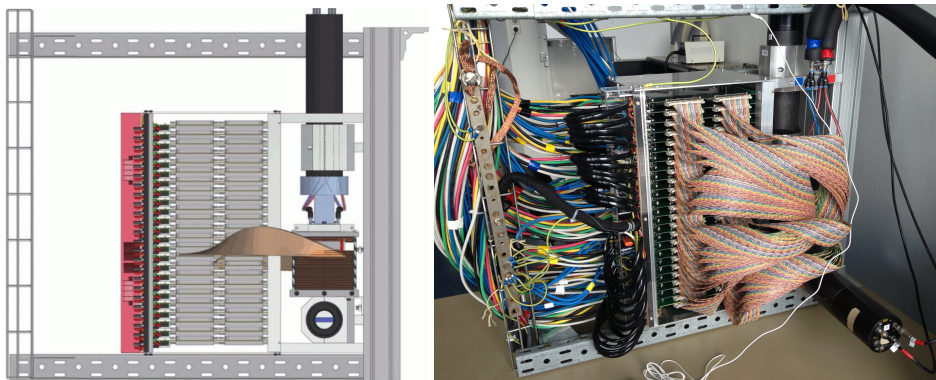


Figure. 2.4: Cosmic setup in Utrecht University, (left) the side view schematic and (right) experimental setup .

For cosmic measurements the detector has been set up in the laboratory at Utrecht University. It is a set up to detect cosmic rays for calibration and alignment of the detector. It is shown schematically in Figure 2.4 on the left, and a photo is shown on the right. The setup consists of the prototype and two NE102a scintillators. Signals extracted from the scintillators are sent to the coincidence logic via BNC cables, which provide a trigger for cosmic muons

travelling through the detector. Both of the F and B scintillators have a size of $40 \times 40 \text{ mm}^2$ and they cover the full active area where the sensors are located in the detector.

The whole setup is on a level table. The two scintillators are mounted in front and on the back of the detector and are labelled as F and B. The prototype was mounted to have the last layer (layer number 23) on top.

2.6 Beam Test Setup

Several beam tests were carried out during 2014. The detector was positioned horizontally towards the beam pipe. The top view of the typical beam test layout is shown in Figure 2.5 Besides the F and B scintillators, three scin-

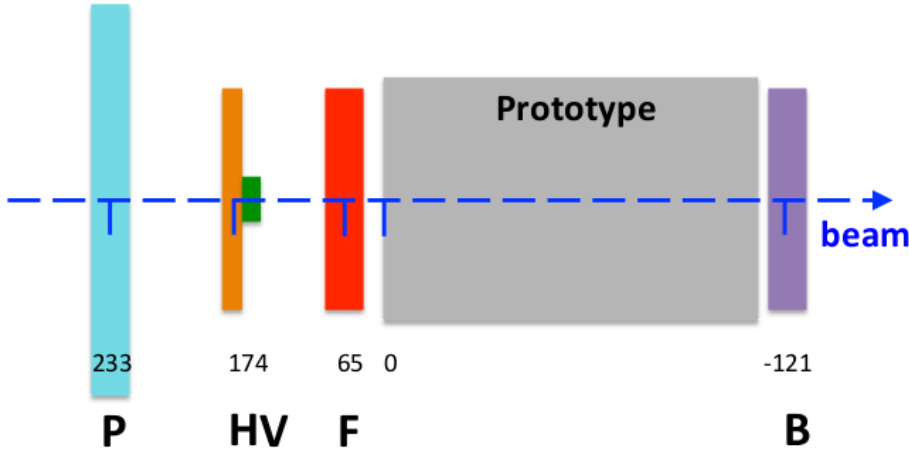


Figure. 2.5: The experimental layout during beam test, the numbers of position are shown in mm.

tillators P (Present), H (Horizontal), and V (Vertical) are also involved in the beam test. The size of the scintillators are:

- **(P)resent:** $110 \times 110 \times 10 \text{ mm}^3$
- **(H)orizontal:** $40 \times 10 \times 5 \text{ mm}^3$
- **(V)erticle:** $20 \times 10 \times 5 \text{ mm}^3$

The coincidence signals from these scintillators are used for selecting events where particles hit in the different positions of the detector during the beam tests. They can be found in Table 2.4.

Table 2.4: Trigger input bits and the corresponding coincidence combinations

Beam Test	Bit 5	Bit 4	Bit 3	Bit 2	Bit 1
DESY	Clock	HV	FP	BP	HP
SPS	Spill	HVF	FP	BF	HF

2.6.1 DESY beam test setup

The DESY (Deutsches Elektronen-Synchrotron) beam test was performed in February of 2014 at Hamburg, Germany. A pure electron beam that covers the energy range from 2 GeV to 5.4 GeV at the T22 beam line was obtained. Since the duration of the beam pulse is much shorter than the buffer filling time of the readout box, the data taking was driven by a pulse generator which indicates the start of a beam pulse.

2.6.2 CERN beam test setup

The SPS (Super Proton Synchrotron) beam test started in November of 2014. At SPS, a mixed beam was provided (electrons and pions) with energies from 30, 50, 100 and 244 GeV. The relative amount of electrons and pions was different at different energies. However, there was no external detector for particle identification at these energies since the Cherenkov system couldn't provide appropriate signals at high momentum at the SPS. To illustrate the beam composition, Figure 2.6 shows the distribution of the number of hits for a beam of 100 GeV. The peak close to zero hits is produced by particles that go through the detector without producing showers, producing a few hits per layer. The broad peak around 25000 hits is produced by electron showers, while the distribution between these extreme cases is produced by hadrons with partially developed showers. The estimate of pion contamination will be evaluated in Chapter 5.

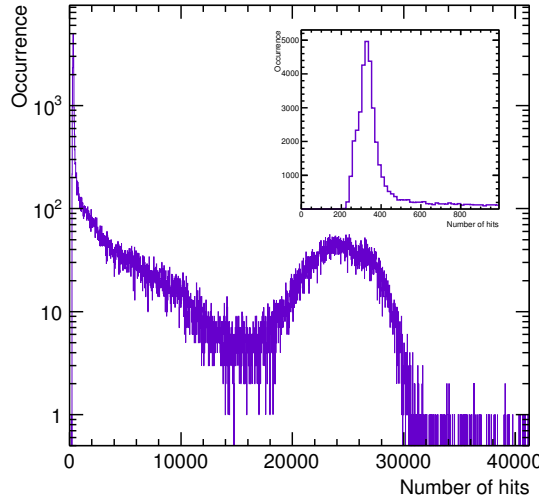


Figure. 2.6: Number of hit pixels of raw SPS data at 100 GV/c. The insert figure shows the region around the MIP peak.

2.7 Data Collection and Statistics

2.7.1 Beam test data statistics

The overview of data collected during the DESY and SPS beam tests can be found from Table 2.5

Table 2.5: The properties of the different data samples collected in test beams.

Time	Site	Particle type	p (GeV/c)	N_{events}
Feb 2014	DESY T22	e^+	2, 3, 4, 5.4	9.5×10^3
Nov 2014	CERN SPS H8	e^+, π^+	30, 50, 100	1.4×10^5
Nov 2014	CERN SPS H8	e^-, π^-	244	1.6×10^4

In this thesis, the electron data will be used in the following analysis topics:

- Shower center reconstruction.
- Pion contamination estimation.
- Calibration optimization based on the lateral density profile.

- Performance results of the prototype, e.g. linearity, energy resolution, position resolution.

2.7.2 Track statistics

Besides the cosmic muon tracks collected at Utrecht University, a large number of pions in the test beam data which do not produce showers in the detector can also be considered as tracks. This leaves us with two different track sources. the overview of the track data sets is shown in Table 2.6 and 2.7.

Table 2.6: Cosmic muons data sets used in the this thesis

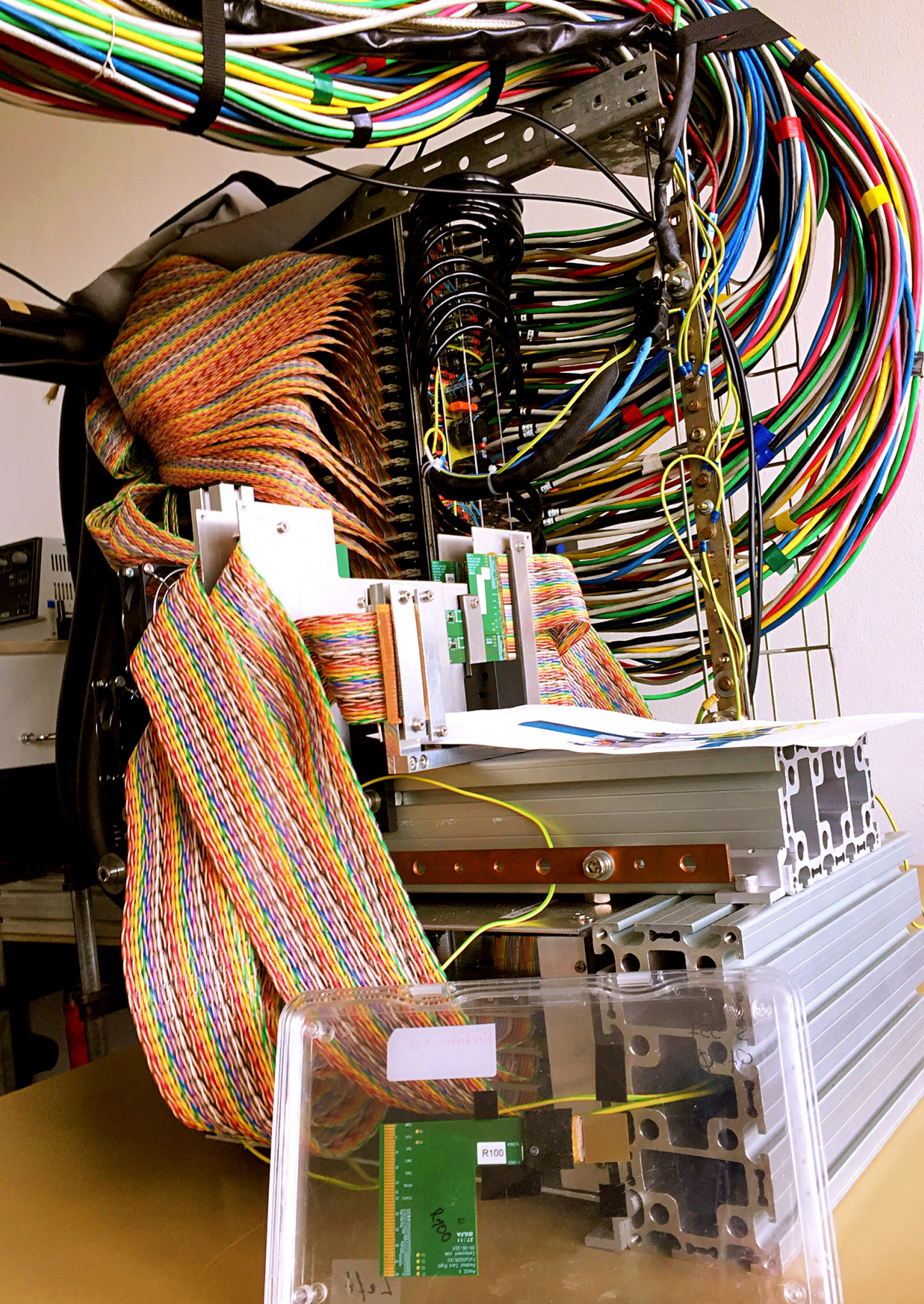
Run No.	Noise Level	Number of Tracks	Year
455-475	10^{-5}	9115	2014
967-975	10^{-5}	3293	2016

Table 2.7: Pion data sets used in this thesis

Momentum (GeV/c)	Particle Type	Number of Tracks	Year
30	π^+	1639	2014
50	π^+	2957	2014
100	π^+	7649	2014
244	π^-	5628	2014

The tracks will be used in the following analysis topics in this thesis:

- Track based sensor alignment.
- Efficiency of sensors in the prototype.
- Beam inclination angle correction for SPS data.



Chapter 3

Analysis Methodology

3.1 Introduction

The high-granularity calorimeter prototype has unique features, which have not been employed by any calorimeter so far. Some of these new features also require the development of new analysis algorithms. In this chapter, a series of approaches and methods that have been used and developed for event reconstruction, noise subtraction and position determination, which will be further used in the MIP and shower particle analysis, will be presented.

3.2 Coordinate System

Figure 3.1 shows the definition of the origin of coordinates and the quadrant number in the analysis. The coordinates of a pixel are calculated with its line (L) and column (C) numbers with the following expressions:

$$\begin{aligned} x_{ideal} &= [j \times (L + 0.5)] \times 0.03\text{mm} & j &= \begin{cases} 1, & Q = 0, 1 \\ -1, & Q = 2, 3 \end{cases} \\ y_{ideal} &= (-C + k - 0.5) \times 0.03\text{mm} & k &= \begin{cases} 0, & Q = 1, 2 \\ 640, & Q = 0, 3 \end{cases} \end{aligned} \quad (3.1)$$

The longitudinal sensor number is the serialized sensor number from layer 0 to layer 23. The simple conversion from layer number l and quadrant number Q to longitudinal sensor number n is:

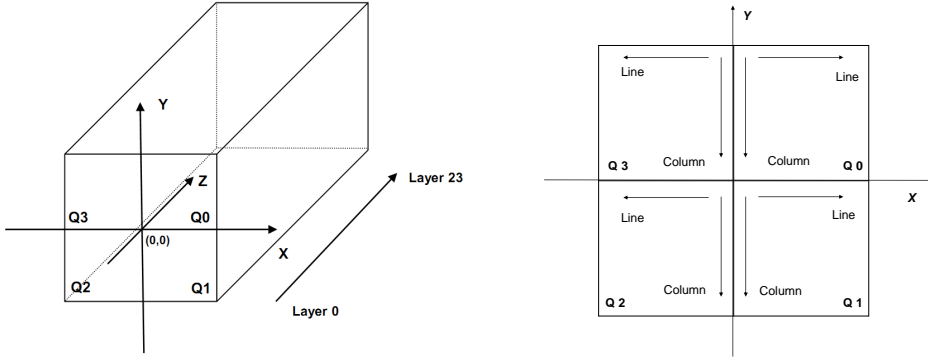


Figure. 3.1: The coordinate system and quadrant definition of the prototype. The quadrant number, original point and layer number are defined in the left plot and the lines and columns in a layer are defined in the right plot.

$$n = l \times 4 + Q \quad (3.2)$$

For the experimental data, the coordinates of a pixel are calculated from the ideal positions by using Equation 3.1. In order to obtain the accurate positions of the pixels, alignment procedure is necessary and will be discussed in Section 3.5 in this chapter, the different position terms in the alignment procedure are defined as:

Nominal position : the nominal position of a pixel is the expected position which is designed in the mechanic scheme of the original design.

Ideal position: the ideal position of a pixel is calculated by using Equation 3.1 without taking any misalignment from the assembly process, gap and overlap into account.

True position: the exact positions where the sensors are located. The true positions are known in the simulation, but unknown in the experimental data.

Aligned position: the aligned position of a pixel is calculated from the translation from the ideal pixel position by using the alignment parameters.

3.3 Pixel Mask and Noise Level

Some sensors, channels, and pixels are malfunctioning after manufacturing and assembly. The following cases need to be masked:

- Sensors and channels that were damaged during assembly.
- Channels that are unstable in some of the frames.
- Lines or columns that show a much higher hit probability in some of the frames.

Noise hits originate from pixels which are activated when there are no particles in the detector. There are two reasons that pixels may contribute to noise in the prototype, one is due to the internal thermal electron-hole pair generation in pixels, and the other one is malfunction of pixels, channels and sensors.

All in all, these masked areas, together with the noise pixels, amount to an insensitive fraction of $\approx 16.7\%$ of the total sensor area installed.

To adjust the numbers of noise pixels in every sensor, two steps of tuning and calculation were performed. First of all, the *physical noise threshold* can be configured via tuning the discriminator settings of the sensor, which are called V_{ref1} and V_{ref2} . The detection threshold can be increased effectively only up to a certain point, since the reduction in sensitivity leads to counting less of the charge as signal and thereby to a reduction of the number of hits representing the signal. In addition to this, the *internal noise threshold* P_i can be determined by integrating the noise probabilities of all good pixels in a sensor, in other words, any pixel with the noise probability above a certain cut value of the probability will be identified as a noise pixel and be masked in the further steps. The internal noise threshold is calculated from:

$$N_{\text{noise}} = \int_0^{P_i} N(P_n) \cdot P_n dP_n \quad (3.3)$$

where N_{noise} is the average number of firing noise pixels, P_n is the noise probability per pixel, and $N(P_n)$ is the number of noise pixels with noise probability P_n . The threshold value P_i of the noise probability is chosen such that the fraction of noise pixels $N_{\text{noise}}/N_{\text{total}}$, i.e. the so-called noise level, has the desired value.

It is difficult to perform the threshold tuning for every sensor in a single step, it requires several optimization steps on the V_{ref} value until the N_{noise} is

fixed to a reasonably low value. For all layers except layer 0, which is the first layer seen from the beam, the internal noise threshold was set to obtain a noise level of 10^{-5} . A similar tuning was used for layer 0 for most data sets, however, to increase the efficiency of identifying the incoming position of electrons during the SPS beam test, some of the data samples use a different threshold of layer 0. The noise rate after tuning for the different data samples for layer 0 that has been used in this thesis can be found in Table 3.1.

Table 3.1: Noise level for layer 0 of different data samples

Noise Level	N_{noise} (pixels/sensor)	Data set(GeV/c)
10^{-5}	≈ 4	2, 3, 4, 5.4
10^{-5}	≈ 4	244
10^{-4}	≈ 40	30, 50, 100
10^{-5}	≈ 4	Cosmic data

3.4 Track Reconstruction

According to the Bethe-Bloch formula describing the ionization energy loss of charged particles, the stopping power decreases with increasing particle momentum. There is a relatively broad interval of minimal energy loss beyond which it increases again. A minimum ionizing particle (or MIP) is a charged particle whose mean energy loss rate through matter is close to the minimum. In many cases, relativistic particles, for example muons, are minimum ionizing particles.

Due to the heavy mass and less bremsstrahlung, the muon has stronger power to penetrate through material, while depositing only a small amount of energy in every sampling layer. It leaves only a relatively small number of detectable hits in the prototype. Pions with high energy may not only produce tracks but also start to cascade in the prototype. However, due to the fact that the prototype is relatively thin in terms of nuclear interaction length, a large fraction of tracks can be detected by the detector for the pion beam. In Figure 3.2, a large number of entries with low number of hits can be seen – these should originate from tracks. The pedestal signals (red line) and the MIP (blue line) signals can be decomposed from template fit. A simple cut on the number of hits at 1000 can be used to separate tracks and showers.

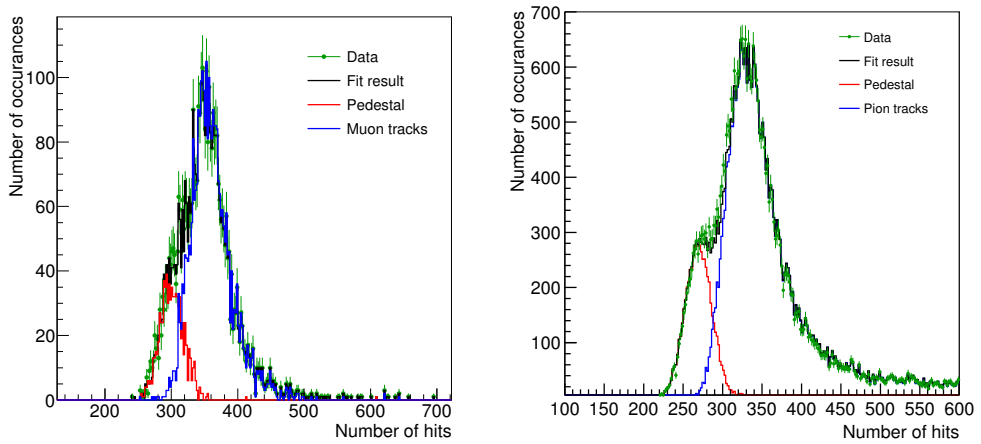


Figure. 3.2: Distribution of the number of hits for (part of the) cosmic muons (left) and pions (right), the region around the MIP peak is decomposed in noise and MIP signals. The noise (pedestal) and the MIP component are visible in both. Note, that a tail from showering particles extends beyond the range of the plot for the pions.

Since the number of noise hits in every frame is ≈ 270 ¹ for 30, 50, and 100 GeV SPS data and ≈ 300 for cosmic muon data and 244 GeV SPS data, this number is significantly larger than the signal hits (≈ 60) generated by the MIP particles, it is difficult to identify the hits from an individual track by applying a simple cut on the number of hits. Moreover, because of the instrumental effects of sensors (sensitivity, dead area) the number of signal hits in the detector may vary. A dedicated tracking algorithm with high reconstruction efficiency is therefore required to reconstruct tracks from raw data.

3.4.1 Tracking algorithm

From the events selected after setting a cut on the number of hits at 1000, we reconstruct tracks according to the following procedure:

1. Combine pairs of hits in different layers to tracklets.
2. Find the most dense region in track parameter space.
3. Use the tracklet with the maximum number of neighbors as the proto track.
4. In each layer, assign hits within $r = 1$ mm to the proto track.

¹The fake hit rate in the layer 0 is 10^{-4} , which is excluded from calculating the number of noise hits.

5. Accept only tracks with more than 24 hits in at least 12 different layers.
6. Find track parameters by χ^2 -minimization of the distance of hits from a straight line.

When performing analysis of a given layer, the track properties are calculated from all layers excluding the one in question.

Due to the multiple scattering in the cosmic data, the limitation of a straight line is obvious. It is necessary to set a certain search radius to preserve as many candidate hits as possible, although the probability of noise increases. Therefore, the search radius is set at 1 mm away from the fit line for both cosmic muons and pions. The details about the multiple scattering effect will be discussed in Chapter 4.

3.5 Alignment

3.5.1 Alignment based on residuals

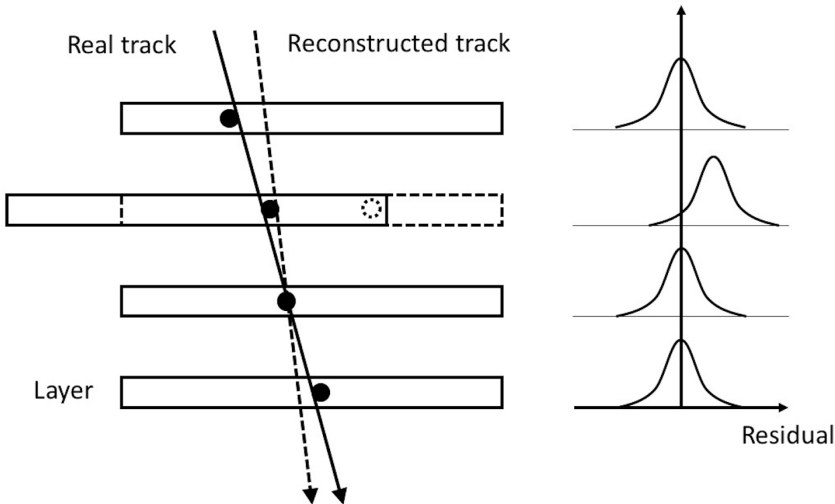


Figure. 3.3: working principle of track-based alignment

It is an important feature to measure the position information of incoming particles for a highly granular calorimeter. To reach the desired goal, the direct use of tracks traversing the detector during operation achieves the highest

precision of alignment. All track-based alignment methods are based on the minimization of the mean of the residual distributions. The residual for a given layer is hereby defined as the difference between the track fit position and its associated hit on a detector plane.

The reconstructed track is the estimate of the true particle trajectory going through the prototype and plays a crucial role in all track-based alignment approach. Over many tracks, the distribution of residuals on a detector module will be roughly uniform. The distribution of the residuals for a perfectly aligned module is then centred around zero with a Gaussian shape (Figure 3.3), however, if there is a misalignment, the mean of the residual distribution will be biased. The principle of alignment based on residuals can be seen in Figure 3.3.

3.5.2 Algorithm

The construction of the prototype allows positioning deviations of the sensors within the x - y -plane. The task of the alignment is to correct these. The possible errors can be described by a rotation angle θ about the z axis:

$$R_z = \begin{pmatrix} \cos\theta & -\sin\theta & 0 & 0 \\ \sin\theta & \cos\theta & 0 & 0 \\ 0 & 0 & 1 & 0 \\ 0 & 0 & 0 & 1 \end{pmatrix} \quad (3.4)$$

and a displacement of the sensor as a translation only in x and y directions,

$$T_{xy} = \begin{pmatrix} 1 & 0 & 0 & \Delta x \\ 0 & 1 & 0 & \Delta y \\ 0 & 0 & 1 & 0 \\ 0 & 0 & 0 & 1 \end{pmatrix} \quad (3.5)$$

The transformation between the ideal coordinates $\vec{C}(x, y, z, 1)$ and the aligned coordinates $\vec{C}^a(x^a, y^a, z, 1)$ can then be given by a combination of this rotation and the translation:

$$\vec{C}^a = T_{xy} R_z \vec{C} \quad (3.6)$$

We define $\vec{\alpha}$ as a collection of alignment parameters $(\Delta x, \Delta y, \theta)$, and the resulting χ^2 is given by:

$$\chi^2 = \frac{\sum_{i=1}^n (\vec{C}_i^a(\vec{\alpha}) - \vec{C}_i^{fit}(\vec{\alpha}))^2}{n\sigma^2} \quad (3.7)$$

Here n is the number of hits and σ is the standard deviation associated to the reconstructed tracks. When track-based alignment is performed on many tracks, the χ^2 becomes a function of the alignment parameters. The multi-dimensional χ^2 has a minimum for the combination of alignment parameters corresponding to the true detector geometry.

Because there is no global constraint of the absolute position of the layers, the simplest approach to remove the potential deformation is to fix some of the detector planes or some of the sensors. Therefore, we take sensor $(l, q) = (0, 0)$ (top right layer 0) as the origin: $(x, y, \phi) = (0, 0, 0)$ and fix the z -axis by setting $x, y = 0$ for sensor $(l, q) = (23, 0)$. This leaves us $(96 - 1) \times 3 - 2 = 283$ degrees of freedom for the alignment. These two sensors are fixed for the alignment verification of both simulated and experimental data which will be further discussed in Chapter 4.

3.6 Shower Position Determination

As fundamental elements of many experiments all over the world, electromagnetic calorimeters are designed to measure precisely the energy of the detected photons and electrons. In addition to the energy measurement, the position of impact of the particles, corresponding to the shower centre position, is usually required. The knowledge of the photon or electron energy and of the incident positions allows to experimentally reconstruct the origin of two photon events from decay of π^0 , η -mesons or of the di-electron from quarkonium via the two-particle invariant mass.

The shower position can be defined as the impact point where particles hit the detector. The detailed information available due to the high granularity of the MAPS sensors should, for a uniform sensitivity, make the determination of the shower centre straightforward. However, for experimental data, it is not always trivial to identify the shower position because of the information lost in dead channels, dead sensors and the non-uniform sensitivity of the layers. The most reliable way is to use only a few layers (e.g. 0,3,4) with fully working sensors to calculate the shower position since they do not suffer from the problems mentioned above. Based on this, a dedicated method to identify the shower centre was developed. In part of the following discussion we will only use x_c

as the reconstructed shower centre in x direction to show the performance of the method since the y_c coordinate can be deduced following the same method. The procedure can be described as follows:

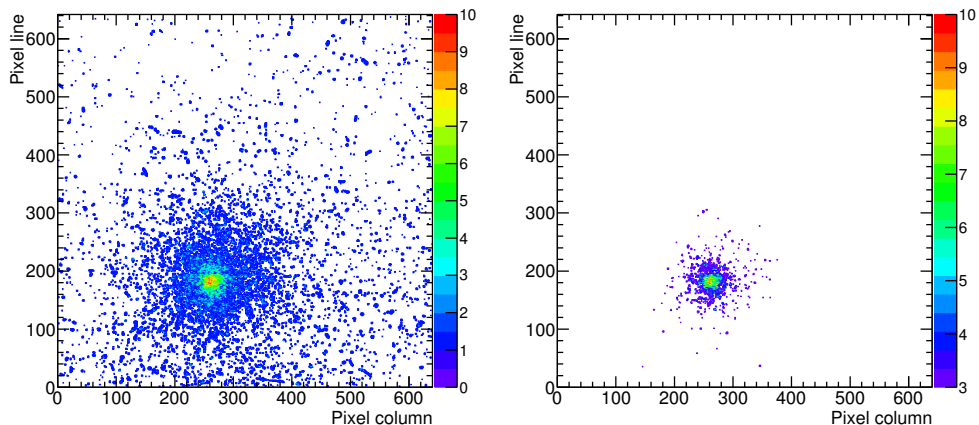


Figure. 3.4: The 2-D transverse hit profile for an electron shower event after identifying the rough shower centre (left) and the region of the profile where the pixel bin contents above $n = 3$ (right).

1. Obtain the 2-D transverse hit profile of all the layer with all the hits in the event.
2. According to the position of the bin with highest amplitude derived from all the layers from the first step, the rough shower position can be obtained, and the corresponding quadrant where the shower is located can be identified.
3. Since the number of working sensors in different quadrants are not identical, in order to reduce the bias may be introduced by the inhomogeneous of the 2-D transverse hit profile. All the hits from all the good layers of the same quadrant identified in the previous step are used to get the transverse hit profile of the quadrant as shown in Figure 3.4 left.
4. Select the region in the transverse hit profile with pixel bin content (amplitude of the sum pixels) above a certain value of n (see Figure 3.4 right), The amplitude in the pixel bins will be used as the weights for final shower centre determination.

5. The shower centre is calculated using the weights with a power t :

$$x_c = \frac{\sum_i w_i^t x_i}{\sum_i w_i^t} \quad (3.8)$$

Because the number of dead sensors and dead channels are different among the quadrants, it is important to use all the good layers in the different quadrants to avoid the bias that may potentially be introduced by the dead area.

The energy deposition is conventionally used as the weight for calculating shower centre. However, it is impossible to directly measure the energy deposition of the shower particles in the pixel, therefore, an alternative approach is to sum the fired pixels in all the working layers in this quadrant to get an equivalent amplitude as an approximation of energy deposition in the sum pixel.

As we know from Section 2.2.1, 90% of the energy of a shower is absorbed within $1 R_M$ range. In Figure 3.4 left, one can see that at distances larger than 5mm the average amplitude ratio is already down by a factor of 10, and decreasing further. This means that the tail part of the shower not only gives no help to determine the shower centre, but may also introduce a bias to the calculation if it is too far away from the centre. To get rid of the bias introduced by the tail, the analysis should be constrained to a region around the shower core which can be established via setting a cut on the amplitude of the sum pixels. In order to emphasize the inner part of the shower core, a power law weight which has been shown in Equation 3.8, was applied in the calculation. This way, the bias from the tail of the shower can be suppressed significantly.

3.7 Inclination Correction

According to the mechanical measurements of the beam test setup, the direction of the incoming particles was supposed to be parallel to the z axis. The beam test setup was measured and placed perpendicular to the beam line in preparation of the beam test. In addition to this, the beam direction of the test beam can also be measured off-line by projecting the reconstructed pion tracks after alignment. As can be seen in Figure 3.5, the projection of tracks show similar trends which indicate the non-perpendicular incidence of incoming particles. An inclination of the beam affects the measurement of the position dependent variables of showers, e.g shower profile and position resolution.

There are different sources that contribute to this effect. The discussion of these sources and the estimate values of the inclination angle that was used in the shower analysis will be shown in the Chapter 4.

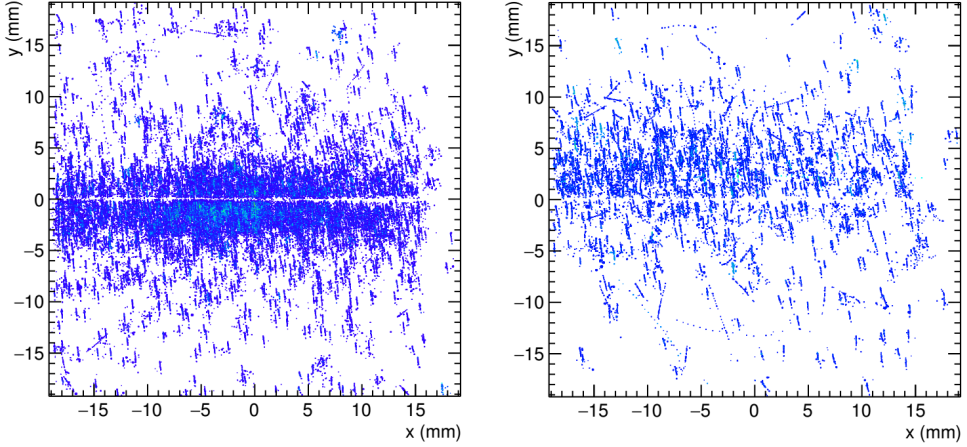


Figure. 3.5: Pion track projection on $x - y$ plane for 244 GeV (left) and 50 GeV (right) pions, the lines of projection indicate an inclination angle of the beam.

3.8 Sensor Calibration and Dead Zone Correction

The sensitivity of a sensor is not only controlled by its readout discriminator voltage (see Section 3.3), but also depends on the thickness of the epitaxial layer. Since there are three different thicknesses of epitaxial layers of sensors, and the threshold settings for all sensors are not identical, the sensitivities of sensors in the FoCal prototype vary and need to be calibrated.

The dead zones in the FoCal, which are mainly dead sensors, dead channels, and noise pixels, affect the measurements significantly, especially in the energy resolution and linearity measurements. The area without any output information together with the varying position of incidence of particles generates considerable fluctuation of the total number of hits in the detector.

One way to solve these questions is to use the hit density of the electrons to extrapolate the lost number of hits in the dead zones. The hit density in a given ring with radius r to the reconstructed shower centre in a sensor in the layer l and quadrant q before calibration can be defined as

$$\rho_{l,q}(r) = \frac{\Delta N_{\text{hit}}^{l,q}(r) - \Sigma p_i}{\Delta N_{\text{pixel}}^{l,q}(r) \cdot (30\mu\text{m})^2} \quad (3.9)$$

where $\Delta N_{\text{hit}}^{l,q}(r)$ is the number of hits in a ring for a given sensor, $\Delta N_{\text{pixel}}^{l,q}$

is the number of counted live pixels within this ring and Σp_i is the total noise contribution, which is obtained by summing the noise probability p_i over the live pixels. Because both the number of hits and the area used are from live areas, the dead areas and the areas where sensors overlap in the ring can be corrected by integrating the area of the ring.

The average response of a sensor before calibration can be obtained via integrating its hits density profile with the following equation:

$$M_{l,q}(R, \langle \rho_{l,q} \rangle) \equiv \int_0^R 2\pi r \langle \rho_{l,q}(r) \rangle dr \quad (3.10)$$

where the $\langle \rho_{l,q} \rangle$ is the mean hit density in this sensor obtained from Equation 3.9 and $\langle \rho_{l,q}(r) \rangle$ is the mean hit density in a given sensor at distance r to the shower axis.

The calibration factors of sensors can be derived from the relative differences average responses between 4 sensors in the same layer.

$$c_{l,q} \equiv \frac{M_l^{fit}}{M_{l,q}(R, \langle \rho_{l,q} \rangle)} = \frac{M_l^{fit}}{\int_0^R 2\pi r \langle \rho_{l,q}(r) \rangle dr}, \quad q = 0, 1, 2, 3, \quad (3.11)$$

Here M_l^{fit} is a coefficient which can be derived from the fit of the average longitudinal shower profile using Equation 2.4 between the different layers [34]. After calibration, the sensitivities of the sensors should be equalized.

The calibrated hit density for a given sensor (l, q) for each shower can be obtained:

$$\rho_{l,q}^c(r) = \frac{(\Delta N_{hit}^{l,q}(r) - \Sigma p_i) \cdot c_{l,q}}{\Delta N_{pixel}^{l,q}(r) \cdot (30\mu m)^2} \quad (3.12)$$

and the calibrated number of hits of the event for a given layer l is:

$$N_l^c(R) \equiv \int_0^R 2\pi r \rho_l^c(r) dr \quad (3.13)$$

The total number of hits after calibration in the radius $R = 20$ mm for a given event is:

$$N_R^c = \sum_{l=1}^{23} N_l^c \quad (3.14)$$

3.9 Parameters for MC Simulations

The development of individual showers cannot be described analytically, but has to be simulated with a Monte-Carlo approach. For electromagnetic processes, it can be described precisely with the electromagnetic interaction model integrated in Geant4 [27]. This is more complicated for hadronic interactions. In the development of a Geant4-based application, it is the user's responsibility to decide which physics processes are required, and then to include them in the "physics list" in Geant4. A description of Geant4 physics lists and their use can be found in [40]. The physics lists that are used here in the simulation for hadrons and electrons are `FTFP_BERT_HP` and `emStandard`, respectively.

3.9.1 Primary particles

Cosmic muon energy and spectrum

For the cosmic muon measurements the detector is located close to sea level, only below a relatively small amount of concrete from the laboratory building. The known cosmic angular distribution and energy loss at sea level can be approximately used in the analysis. The cosmic muon angular distribution is generated with the empirical equation [22]

$$I_\mu = (72 - 7.8 \cdot \sin^2 \theta) \cdot \cos^2 \theta \quad (3.15)$$

Here θ is the zenith angle.

The multiple scattering depends on the energy of muons, which is crucial for tracking the muons in the prototype and will also influence the precision of alignment. An approximate extrapolation formula [38] for the muon energy spectrum valid, when muon decay is negligible and the curvature of the Earth can be neglected, is

$$\frac{dN}{dE_\mu d\Omega} \approx \frac{0.14 E_\mu^{-2.7}}{\text{cm}^{-2} \cdot \text{sr} \cdot \text{GeV}} \quad (3.16)$$

Electrons

The energies of electron data sets used in simulation are the same energies as the experimental data. The incident position of electrons is from $-15 \text{ mm} < (x, y) < 15 \text{ mm}$. The finite momentum spread of the test beam is not simulated.

Pions

Pions are used for two purposes in the simulation. The first is to estimate the pion contamination in the full energy peak of electrons in test beam data. The other one is to study the general separation power between electrons and pions in the FoCal prototype. Pions with the same momentum as the experimental electron data were generated in the simulation. The incident position of pions are also from $-15 \text{ mm} < (x, y) < 15 \text{ mm}$ and perpendicular to the detector plane.

3.9.2 Shower position definition

In simulation analysis, shower position can be obtained from the primary particles in Geant4, that makes shower position definition much simpler and preciser than experimental data. A uniform distribution for the incident position of primary particles within $\pm 15 \text{ mm}$ in both x and y directions from the centre of the detector for the electrons and pions was used.

3.9.3 Charge sharing model

The charge deposited by incoming particles in the epitaxial layer of the sensor can diffuse into different directions and this may lead to the activation of several pixels at the same time. The charge collecting process in simulation has been modeled and simulated.

The charge diffusion model algorithm was developed and the powerful performance has been shown and discussed in [34], here we just simply describe the principle of the model.

This model can be further simplified such that only the isotropic charge diffusion is responsible for the distribution of the generated charge. The charge moving towards the substrate will be reflected by the potential barrier. The charges collected are the sum of the charges that reach the collection diode directly and after reflection. The charge collection probability is:

$$\rho(\vec{R}) = \frac{d\Omega}{4\pi} = \frac{1}{4\pi L} \frac{hr}{(h^2 + r^2)^{3/2}} dr d\phi \quad (3.17)$$

where

- r is the horizontal distance to the diffusion point.
- L is the thickness of the epitaxial layer.

- h is the depth where the charge is generated in the epitaxial layer.
- $d\Omega/4\pi = \sin\theta d\theta d\phi/4\pi$ describes isotropic diffusion of the charges.

The charge collection of a certain pixel can be obtained by integrating the distribution above over the pixel area for all charges.

In this thesis, a threshold of 470 eV is used for a sensor thickness of 20 μm [34]. The agreement of the shower response between experimental data and simulation indicate the modelling and parameters are good enough to describe sensor property.

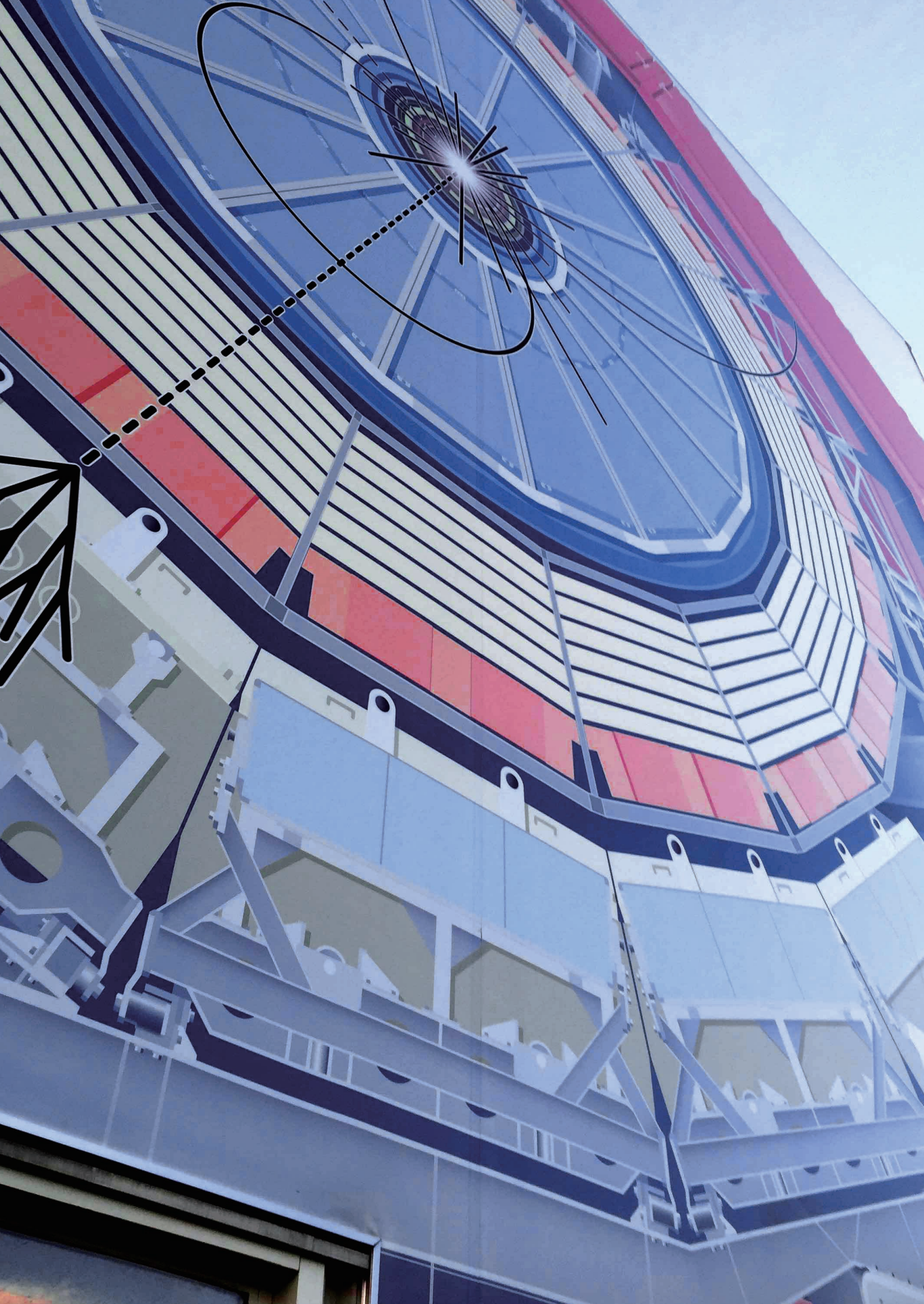
3.9.4 Noise

For MIP analysis (cosmic muon and pion tracks), there is neither charge sharing nor noise implemented in the simulation because the amount of hits generated by the MIP in the detector is relatively small.

A *Poisson* distribution was used in the simulation to describe the spectrum of noise. In the chapter 5, for the analysis of the electrons and pions which produce showers in the detector, the fake hit rate is tuned to 10^{-5} which equivalents to average 4 noise hits for every sensor. However, the dead sensors, channels and pixels which do not produce any signal in the data make the number of noise hits decrease as well. It results 3.55 noise hits per event on average. In the simulation, the mask procedure is not necessary. A number of noise hits is picked from a Poisson distribution with an average of 3.55 and is randomly distributed over the sensor surface. The resulting noise contribution to the final energy resolution is $6.3\%/E(\text{GeV})$ and will be used in the fitting of the energy resolution curve in Chapter 6.

3.9.5 Misaligned sensors in simulation

In order to make the simulation more realistic and allow the verification of the alignment procedure, a misalignment was implemented in the simulation. This was done by moving the sensors in both x and y direction in the geometry setting of Geant4. Also the gap and overlap region for every layer can be built into the simulation. The numerical values used are based on the estimates from experiment data. Although the sensors were moved, the true position of sensors can be recovered in the simulation. The numerical values of misalignment for every sensor can be found in the appendix.



Chapter 4

MIP Analysis

4.1 Introduction

High precision of the position measurement is a unique feature of the high granularity calorimeter. However, the misalignment of the sensors, which is introduced during the assembly may become a systematic bias for the position measurement of particles, and its effect needs to be corrected by an alignment procedure, which is a crucial intermediate step for reconstructing charged particle track and the precise location of the shower centre. The alignment algorithm is based on the tracks produced by MIPs (minimum ionizing particles) in the FoCal detector and has been developed and discussed in Chapter 3. In this chapter, the alignment results will be shown and discussed. The results show that the alignment precision, which will be discussed in both simulated and experimental data, can reach the μm level. In addition to the alignment, the sensor efficiency measured with MIPs will also be discussed in this chapter.

In this chapter, we will use “nominal position”, “ideal position”, “true position” and “aligned position” to describe the pixel or sensor positions in different situations. The definitions of different terms of positions have been defined in Section 3.2.

4.2 Alignment Verification in the Simulation

In order to not only verify the alignment algorithm, but also to have better understanding of the precision in the alignment, the alignment algorithm has been applied to a simulated muon data.

In contrast to the experimental data, the true position of the sensors is known in the simulation. In order to verify the alignment performance, the ideal

coordinate system which is the same as the experimental system was also implemented in the simulation (the definition of coordinate system can be found in Section 3.2.). The alignment in the simulation starts with the ideal coordinates of the hits, if the alignment works successfully, the difference between the true position and aligned position of the hits on the sensors should be approximately zero.

In the simulation, the ideal coordinates of the hits from the tracks on the sensors are the initial input to the alignment procedure, which is the same as the experimental situation. The comparison between aligned and the true coordinates of the hits after alignment shows the precision of alignment.

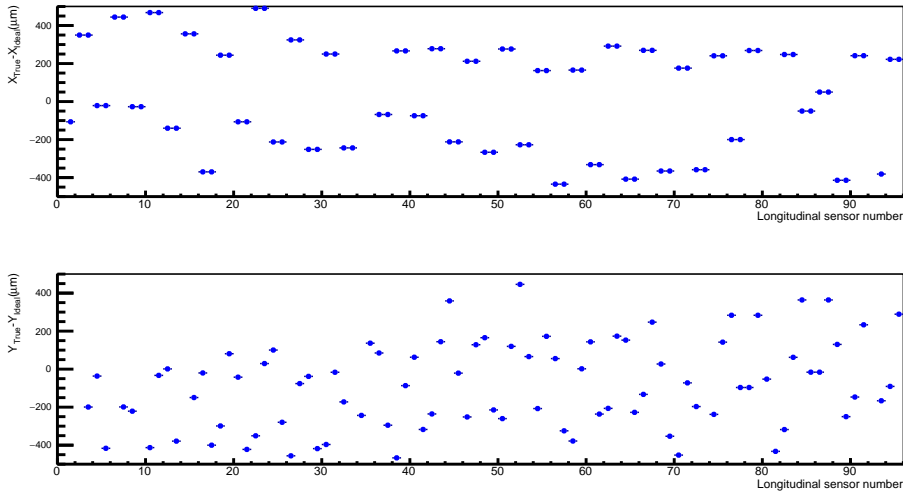


Figure. 4.1: Difference between the true position and ideal position in the x (upper panel) and y direction of all the sensors in the simulation.

The residuals between true and ideal positions as a function of longitudinal sensor number¹ are shown in Figure 4.1. We can see the regular pattern with two sensor grouped together only in the x direction. The reason is that every layer consists of two identical modules, each with two sensors. The two sensors glued together in a module only artificially misaligned along the x direction instead of the y direction compared with the ideal sensor position (because in the y direction, the default gap region has been implemented in the geometry of the simulation). The values in Figure 4.1 consist of two different sources of physical position shift in the misalignment. The first one is the shift between

¹The definition of longitudinal sensor number can be found in Section 3.2

nominal and ideal positions. The second one is the shifts we implement to simulate the misalignment during assembly. The total shift of the two sources mentioned above can be approximately up to hundreds of microns, and they should be corrected by the alignment.

4.2.1 Track selection

The algorithm of the tracker in the simulation is the same as in the experiment and has been introduced in Section 3.4.1. However, neither noise nor the charge sharing has been implemented for this study. The track selection criteria in the simulation are:

1. To reduce the influence from the multiple scattering of muons, only the tracks that have hits on both the first and the last layers are selected.
2. If there more than one cluster is found in a given layer, only the largest one is used in the alignment.
3. The centre of gravity of the cluster was used for alignment.
4. If there are more than two largest clusters with the same number of hits on a certain sensor, both of the clusters are discarded from that track.
5. There is no constraint on the size of the cluster.
6. There are no dead sensors in the simulation, all the sensors are included in the alignment procedure.

4.2.2 Residuals

In simulation, the residual is defined as the difference between the true position of the hit and the position of the fitted track in that layer. As can be seen in Figure 4.2, the residuals in x and y directions are shown in the left panel and the projection of the residual distribution should be a Gaussian, which is shown in the right panel. The width of the distribution gives the track resolution of the straight track model. Figure 4.3 shows that the mean values of the residual distribution of all sensors before alignment in the simulation. These values are consistent with the values of the misalignment in Figure 4.1 and they represent the shifts between true positions and ideal positions of the sensors. Figure 4.4 shows the mean residuals after alignment. They are close to 0 with deviations below $20\text{ }\mu\text{m}$ (below $5\text{ }\mu\text{m}$ for most sensors). This indicates that the residuals in x and y directions can be used to monitor the quality of the alignment with a precision of better than 5 micrometer for most sensors.

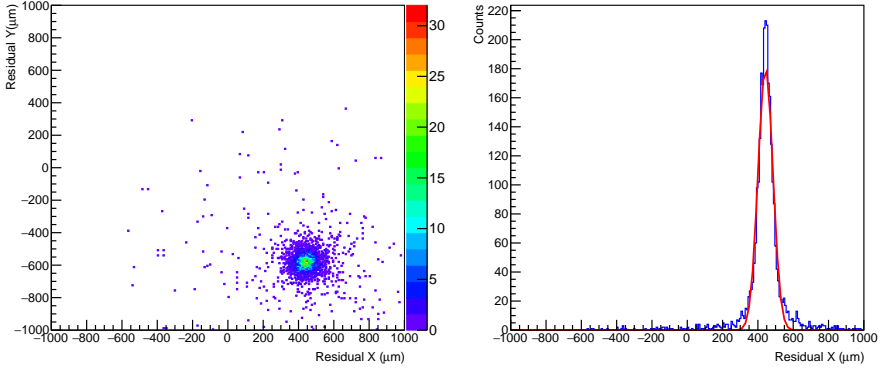


Figure. 4.2: Residuals distribution in x and y directions of sensor 46 in layer 1 (left) and the projection in x direction(right) in the simulation.

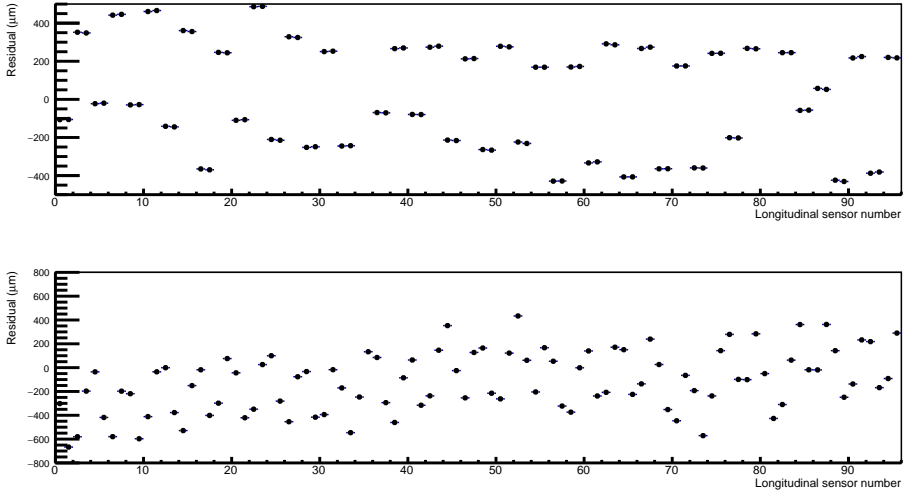


Figure. 4.3: Distribution of residuals between hit ideal position and the position of fitted track of simulated cosmic muon tracks as a function of sensor number before alignment in x (upper) and y (lower) directions.

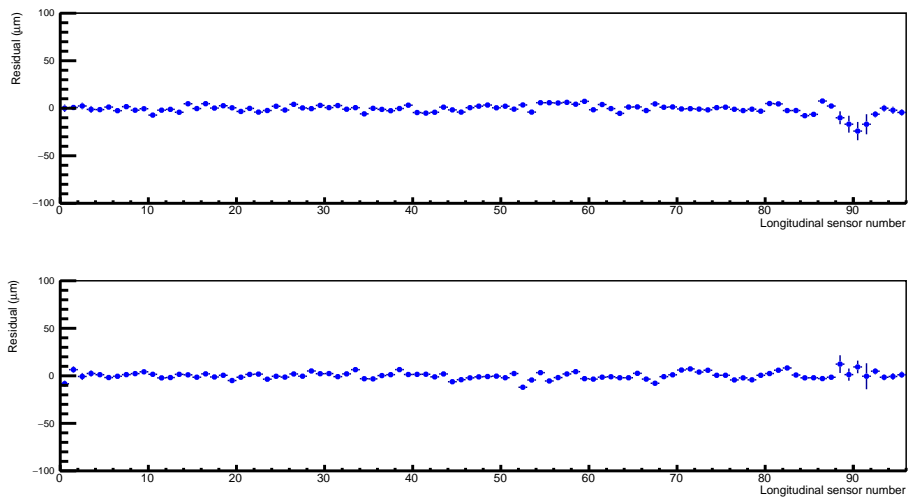


Figure. 4.4: Distribution of residuals between hit aligned position and the position of fitted track of simulated cosmic muon tracks as a function of sensor number after alignment in x (upper) and y (lower) directions.

4.2.3 Alignment accuracy

The distribution of the difference between true and aligned positions of the sensors shows the accuracy of the alignment. For most of sensors in Figure 4.5, the average residuals in both x and y directions are less than $10\ \mu\text{m}$.

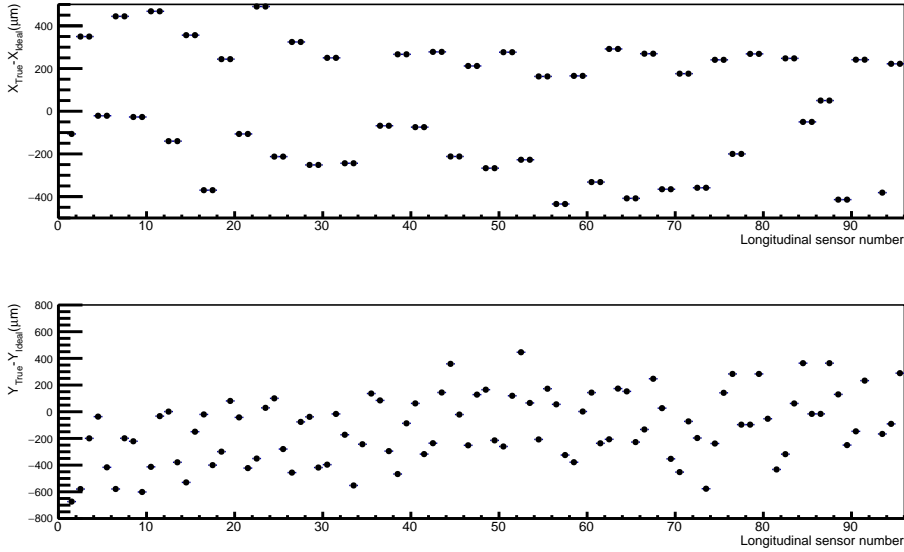


Figure. 4.5: Difference between the true position and aligned position for all the sensors in x (upper) and y (bottom) directions after fixing the two sensors in the first and last layer of the simulation. The fixed two sensors $((l, q) = (0, 0), (l, q) = (23, 0))$ are not shown in the plot.

4.3 Alignment Verification with Cosmic Muons

4.3.1 Track Selection

There are two independent cosmic muon data sets which are used for the alignment. The two samples can provide an independent cross check of each other. Table 2.6 and 2.7 shows the number of collected events in the two data sets. The cosmic muons of the two data sets were collected in different time periods. In Figure 4.6, one can see the correlation of residual values between these two data sets before alignment. The strong correlation indicates that the geometry is stable even though the detector has been transported several times during this period. It also tells us that the residuals before alignment are large compared to the intrinsic position resolution ($< 30 \mu\text{m}$) – they are of the order of tens to hundreds of microns.

The χ^2 minimization which determines the alignment parameters depends significantly on the quality of the tracks used in the alignment procedure, e.g. distribution of track angles and multiple scattering (multiple scattering effect will be further discussed in Section 4.6). Cosmic ray muons are useful as they

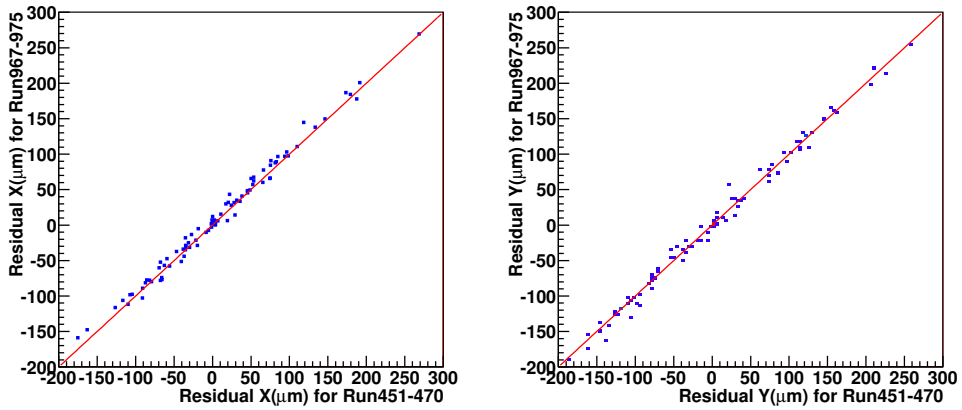


Figure. 4.6: Residuals before alignment for different cosmic data sets in x (left) and y (right) directions.

come from different angles. The large angle tracks from cosmic ray muons can cross different quadrants of the detector and thus provide information to align the sensors in these different quadrants with respect to each other. As a result, they provide precise alignment especially in the gap and overlap regions in every layer. There is also a disadvantage of cosmic muons, which is the multiple scattering. The average momentum of the cosmic muons is around $4 \text{ GeV}/c$ [38], and compared with the much larger momentum pion data the probability of producing large angle multiple scattering is also much higher. Low-momentum tracks suffer from multiple scattering and those tracks are of little use for alignment. More discussions about the influence of multiple scattering can be found in the efficiency analysis later in Section 4.7. Considering the multiple scattering and some other effects, for tracks from the cosmic muon data the criteria 5 and 6 given in Section 4.2.1 were modified as follows

5. If the number of hits of the largest cluster on a certain sensor is larger than 10, the cluster is discarded from that track.
6. Sensors with large dead areas are excluded from the alignment (longitudinal sensor number: 11, 45, 53, 72, 76, 84, 85, 86, 87).

4.3.2 Sensor geometry

An intuitive verification of the alignment can be done from qualitative features of the geometry of the prototype. e.g. the physical overlap region along the x direction and the gap along the y direction in every layer, which should be reconstructed after the alignment, should be easily visible.

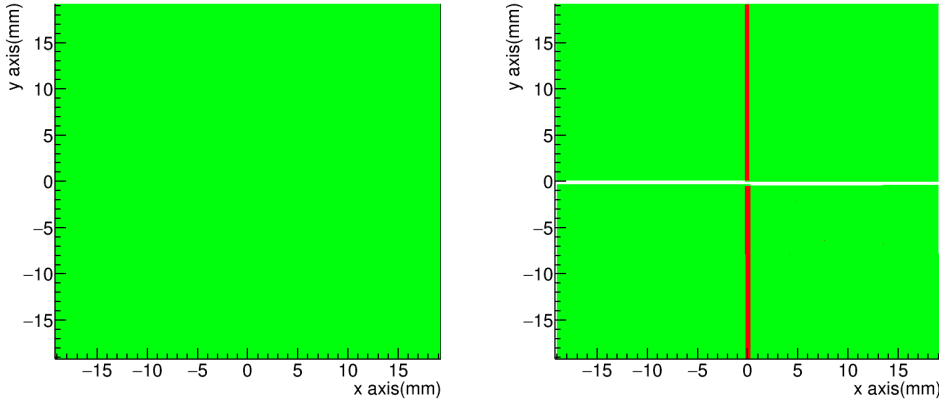


Figure. 4.7: Geometry of layer 0 before (left) and after (right) alignment. The green region indicates the sensor. The red region is where the sensors are overlapped and the white region is the location of the gap between sensors.

Figure 4.7 shows the geometry of all the sensors before and after alignment. The left panel shows the “ideal” (see Section 3.2) layout of the layer, which was homogeneous before alignment. After alignment, the right panel, the sensors in this layer have been moved to a realistic position. The red overlap region is clearly visible in the figure, as is the gap between two sensors that are mounted on a single PCB (white area). The layer is physically constructed with two pairs of modules (left and right parts), the overlap region, which is the red area along the y direction is related to the relatively opposite movement directions of the modules.

4.3.3 Alignment parameters

Three degrees of freedom are involved in the alignment procedure. They are the rotation angle around the z axis, and movements along x and y axes. The rotation angle of all sensors as determined by the alignment procedure is shown in Figure 4.8 on the right. It shows that the rotation angles of all sensors are

between -0.01 and 0.01 radian, which are small enough to neglect. The sensors assembled in the same module show a similar rotation angle as expected.

The alignment parameters in the x and y directions as determined by the alignment procedure in Section 3.5.2 are shown in Figure 4.8 in the left and middle panel. The alignment parameters are given with respect to the ideal position of each sensor. The results clearly show the overlap between sensors in the x direction of about $500\text{ }\mu\text{m}$ and the gap in the y direction, which is of similar size, but visible as approximately equal and opposite offsets for (Q0, Q1) and (Q2, Q3).

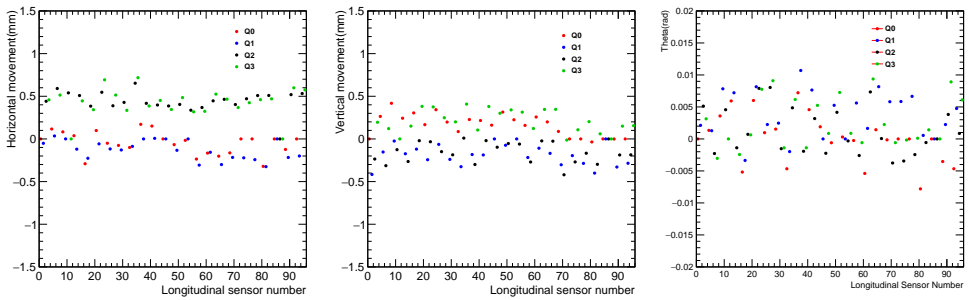


Figure. 4.8: Alignment parameters in x (left panel), y (middle panel) and rotation angle (right panel) for all the sensors in the prototype from cosmic data.

4.3.4 Residuals

Another important check of the alignment quality is to look at the residuals similar to what was done in section 4.2.3 for the simulation. In the track model described in Section 3.4, the tracks after selection can be fitted with a straight line. The residual is defined as the difference between the measured cluster centre position and the expected position from the fitted track on each layer. This observable can show a bias if the detector is not well aligned. If the alignment has been correctly performed, the residuals distribution should be a Gaussian like distribution which is centred on zero.

Figure 4.9 shows the residual distributions of all track hits for the four sensors in layer 8 before and after alignment. The distribution before alignment (red histogram) show shifts due to the misalignment of the sensors. These apparent shifts of the distributions are corrected by the alignment procedure (blue

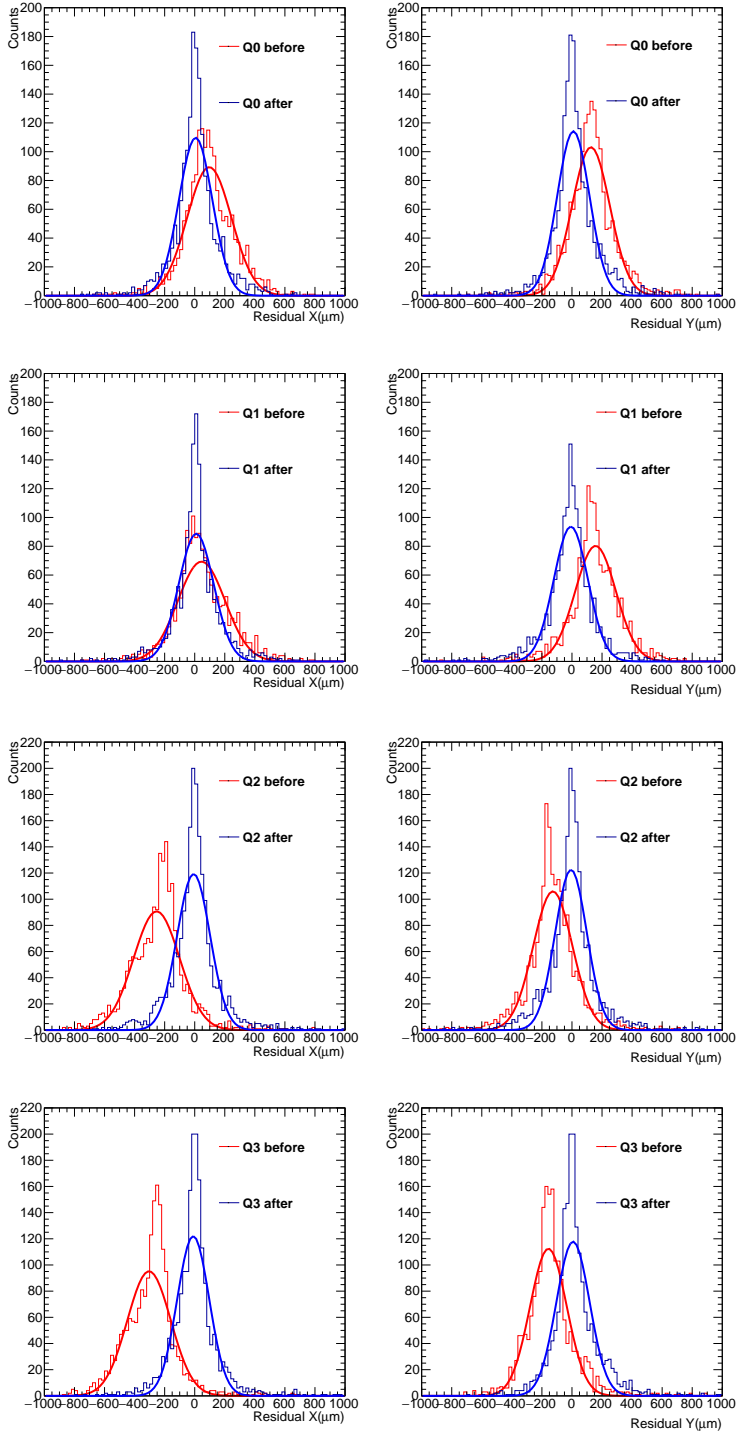


Figure. 4.9: Residual distributions for the sensors on layer 8 in x (left column) and y (right column) directions for the cosmic muon data. Histograms are shown “before” (red) and “after” (blue) alignment.

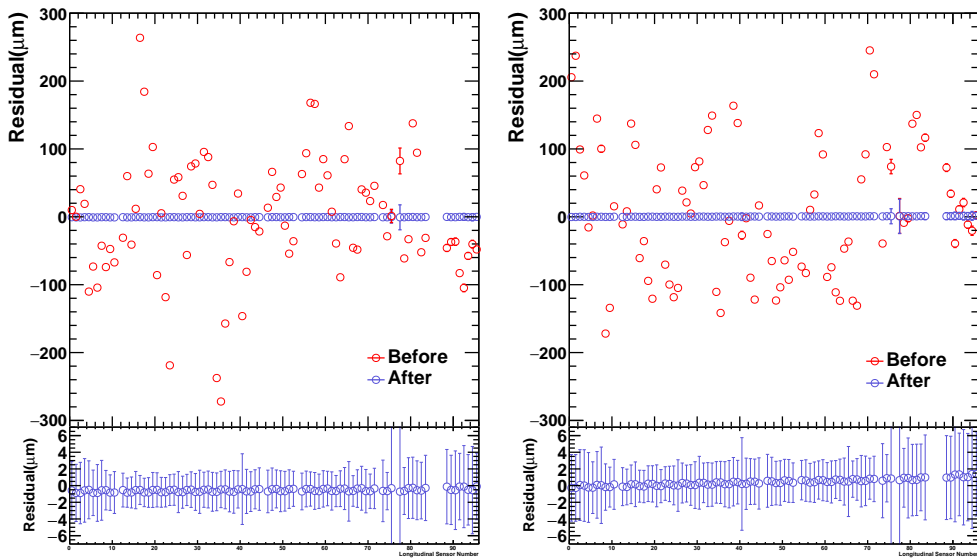


Figure. 4.10: Residual before (red symbols) and after (blue symbols, enlarged in the lower panels) alignment with cosmic muons data. Plots are shown in x (left) and y (right) directions.

histogram), as is visible from the distributions after alignment. The mean residuals of cosmic muons from Run 451–470 before and after alignment for all the sensors are shown in Figure 4.10. The mean values in the plot scatter in a broad range before alignment, which can be up to hundreds of microns, while after alignment, the spread is reduced to less than 5 microns, which demonstrates that the alignment procedure was successful.

The width σ of the Gaussian fits to the residual distributions in each sensor is shown in Figure 4.11. For most sensors, the residual distributions become narrower after alignment. This is obvious in the inner layers in longitudinal direction of the detector. However, in the first and last a few of layers, the width of the distribution is in general larger than in the central part and a decrease is not so apparent, which is related to the multiple scattering.

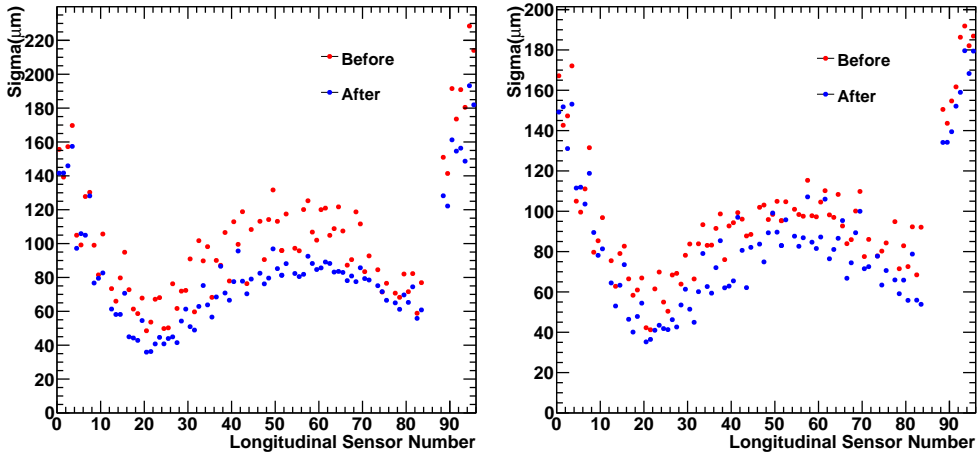


Figure. 4.11: Sigma of residual distributions of all sensors before (red symbols) and after (blue symbols) alignment with cosmic muon data in x (left) and y (right) directions.

4.4 Alignment Verification with Pions

As an independent check of the alignment procedure, pion tracks from the beam test are used for the validation of the alignment quality. The main features of the data sample are given in Table 2.6. The direction of the pion tracks is parallel to the z axis of the detector. The impact of multiple scattering is less than for the cosmic muon data because of the high energy of the pions.

The validation starts from checking the residual between the fitted track position and the hit positions after applying the alignment parameters obtained from the cosmic muon alignment. Pion tracks of 100 GeV are selected for the independent check of the alignment performance because the beam profile in this test beam experiment had the most uniform distribution over the acceptance of the detector. The mean and width of the residual distributions for each sensor are shown in Figure 4.12 and Figure 4.13

As can be seen in Figure 4.12, the mean values of the residual distributions of the pion tracks are less than $10 \mu\text{m}$ for most of the sensors in the detector in both x and y direction. Some of the sensors show a large error bar related to a small number of tracks/hits being available, which is caused by the bad channels in the sensor.

Figure 4.13 shows the width of the residual distributions of pion data before and after applying the alignment constants derived from muons in x and y directions. We can see from the plot that:

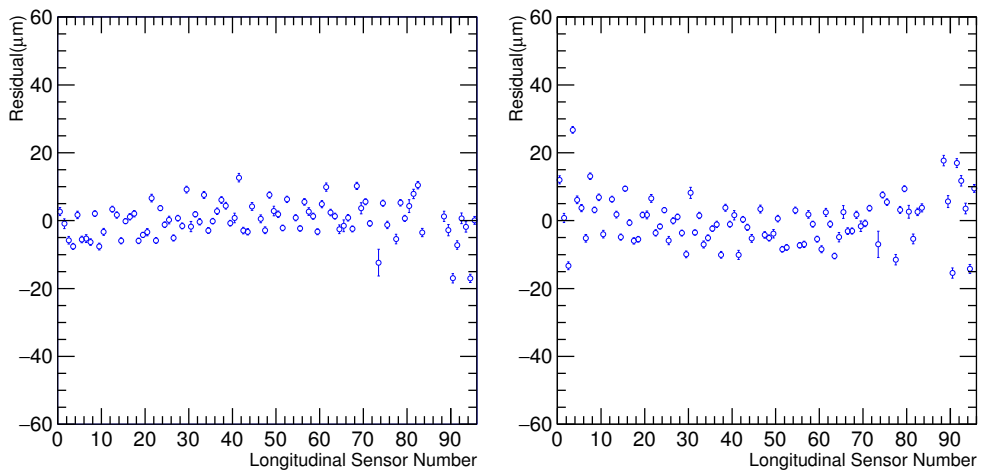


Figure. 4.12: Residual of 100 GeV pion tracks by applying the alignment parameters extracted from cosmic muon data in x (left) and y (right) directions.

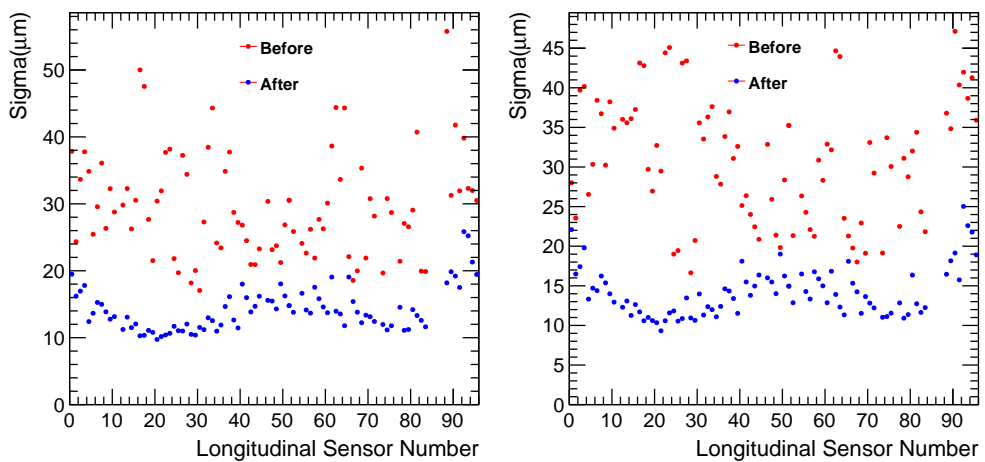


Figure. 4.13: Sigma of residual distribution of all sensors before and after alignment with 100 GeV pion data in x (left) and y (right) directions.

1. The widths are in general smaller than for cosmic muons which were shown in Figure 4.11, either before or after the alignment. This is due to the fact that the energies of pions in the SPS data are much higher than those of cosmic muons, which means the trajectories of pions can be better fitted by the track model. The residual between the fit point and observed cluster of pions is smaller than cosmic muons.
2. The widths decrease significantly for most of the sensors after the alignment, which is what we expected and also a proof that the alignment works.
3. There is a qualitatively similar w-shaped modulation of the widths as seen in muon data. The explanation is that multiple scattering could lead to curving tracks, when we apply the straight line fit to these tracks, there must be two points of intersection. This leads to the characteristic 'w' modulation of the widths of the residual distribution as a function of layer number. When the energy of the track increases, the curvature is reduced, which makes the "w" shape flatter.
4. The strong increase of the width for the first and last layers that has been shown in the muon data is not visible in the pion data, which is also due to the less multiple scattering for the pion data.

4.5 Inclination of the Beam

The distributions of the difference in x and y position of the pion tracks in the first and last layers are shown in Figure 4.14. One can clearly see that the displacement in the y direction is around 1 mm, which proves that the inclination angle between the beam and detector is significant and needs to be corrected in the analysis.

The correction of inclination angle was performed by a shift of the coordinates of every pixel. The values of the shift depend on the layer number (l) and can be calculated by the following expression:

$$x_l^{incline} = x_l^{align} - 0.15(\text{mm}) \times \frac{z_l}{z_0} \quad (4.1)$$

$$y_l^{incline} = y_l^{align} + 1.07(\text{mm}) \times \frac{z_l}{z_0} \quad (4.2)$$

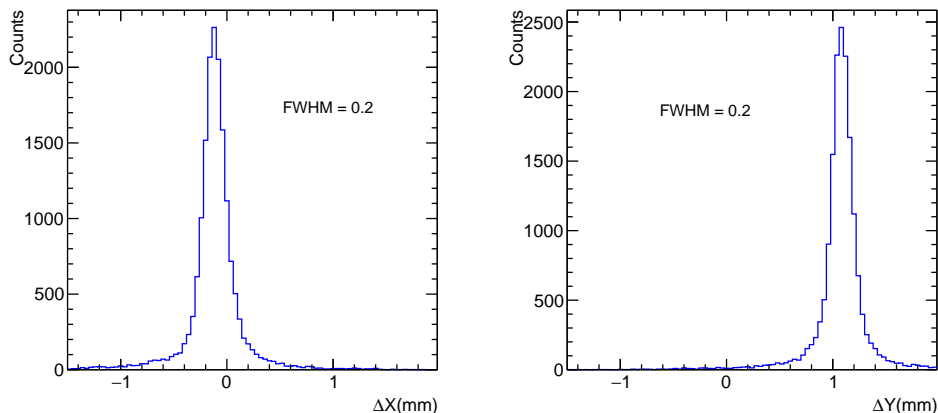


Figure. 4.14: Distribution of the estimated displacement between entry and exit points of 100 GeV pion tracks in x (left) direction and y direction (right).

4.6 Multiple Scattering

In multiple scattering, most processes are soft, small angle scatterings. Occasionally harder scatterings to larger angles may happen. Such cases of hard scattering will be effectively ignored by our tracking algorithm, which assumes a straight line trajectory.

The width θ of the angular distribution of a particle beam after a certain thickness of material depends on the particle momentum as $\theta \propto 1/p$ [38]. The higher the momentum of the particles, the narrower is the angular distribution from scattering. The average momentum of cosmic muons is around 4 GeV/ c [38], which means that some of them are lower energy muons that probably make large angle multiple scattering after passing through the tungsten absorber in the FoCal detector, especially in the 20mm thickness of tungsten block between 21st and 22nd layers.

Figure 4.15 shows the width of the distance distribution between the straight line fit point and the closest cluster produced by the muon track in all the layers in the simulation. For the purpose of comparing the simulation to the data, we use 2 GeV muons and 50 GeV pions in this analysis. The layer numbers are converted to depth in units of radiation length. Here we have to note that there is no noise added in the simulation, so all the clusters in the detector are produced by the the incoming particle or its secondary particles. The left panel of Figure

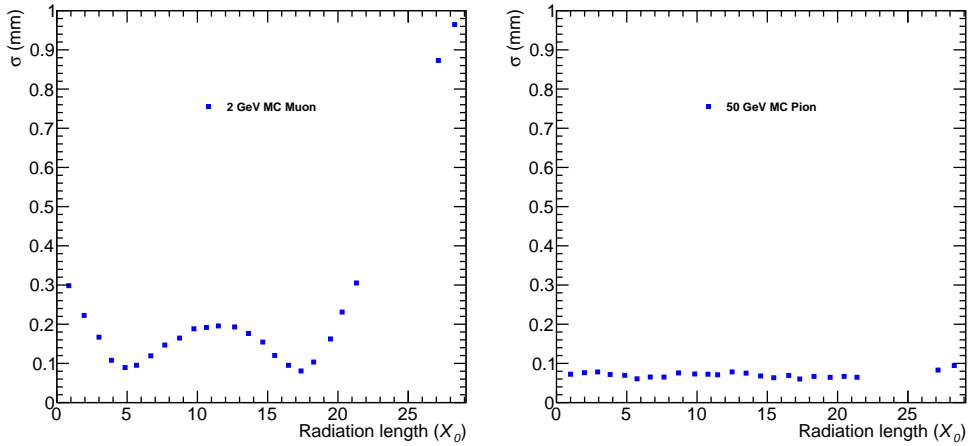


Figure. 4.15: Width (σ) of the distribution for the distance between the closest cluster in every layer to the position of the fitted track in the same layer as a function of the longitudinal depth for the 2 GeV muons (left) and 50 GeV pions (right) in the simulation.

4.15 shows the mean residual for 2 GeV muons. The values of the widths of the distributions are significantly larger than for the right panel, which shows results for 50 GeV pions. This is due to the curvature of the trajectory introduced by multiple scattering of the low energy muons. For 2 GeV muons, the widths of the distribution in the last few layers are large. In the data analysis, the search radius of 1 mm is used to associate hits with tracks. This will lead to a loss of the hits when defining a track, which will be a crucial effect for the sensor efficiency measurement discussed in later Section 6.2. This effect is not present in the pion data since they have less scattering.

Figure 4.16 shows similar distributions as Figure 4.15 but for the experimental cosmic muon data and 50 GeV pion data. We observe a similar effect in the experimental cosmic muon data as demonstrated in the panel of Figure 4.16, due to the track curvature induced by multiple scattering. A clear difference is seen between the cosmic muon data and the results for 50 GeV pion tracks. It is expected that the large residuals due to the effect of multiple scattering in the cosmic muon data lead to a loss of efficiency. This is further discussed in Section 6.2. The precise efficiency of the sensors in the detector can only be determined using pion tracks.

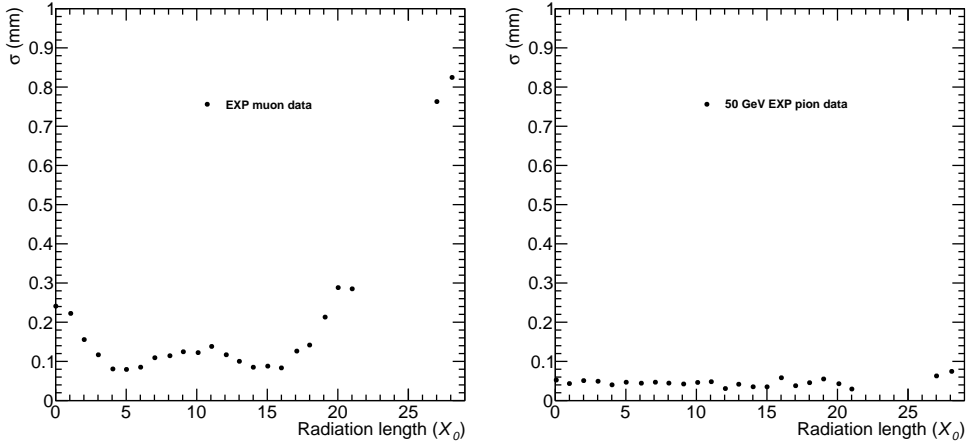


Figure. 4.16: Width (σ) of the distribution of the residuals between the closest cluster in every layer to the position of the fitted track in the same layer as a function of the longitudinal position in units of radiation length for the experimental cosmic muon data (left) and 50 GeV experimental pion data (right).

4.7 Sensor Efficiency Measurements

The energy of the pions at SPS is close to the minimum ionizing range. These pions are expected to travel through the detector on straight trajectories. These pion tracks will be used in the following to measure the efficiency of the sensors.

The sensor efficiency is defined as

$$\epsilon_l^q = \frac{N_{assoc}}{N_{total}} \quad (4.3)$$

where N_{assoc} is the number of tracks associated with a hit on the sensor and N_{total} is the total number of tracks passing through the sensor.

4.7.1 Effect of non-active areas

The gap between the sensors is an insensitive area along the x direction on every layer of the prototype. Pion tracks that go through the gap area of the layer will result in an efficiency drop. It is necessary to remove these tracks.

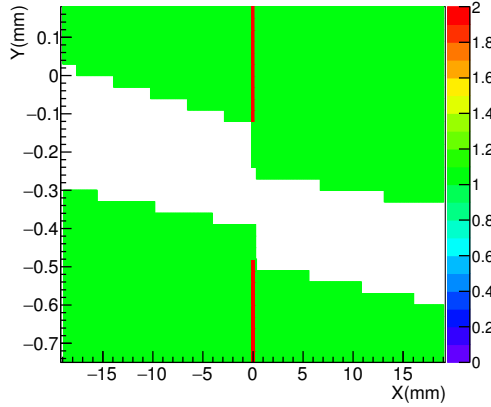


Figure. 4.17: Distribution of active pixels as a function of x and y in layer 0. The distribution is zoomed-in in the y direction.

Figure 4.17 shows a zoomed view of the gap of Figure 4.7 right. The blank area in the central part of the pixel pattern is the gap, and the red area parallel to the y axis is the overlap area. The width of the gap in the y direction is approximately $350\ \mu\text{m}$.

Since the track can be fitted by a straight line, the position of fit points on every layer can be obtained. The track will be removed from the calculation of the efficiency of the sensor if the fit point falls into the gap region.

Apart from the gap, some other types of dead areas exist in some of the sensors. This relates to either some of the channels or the whole area of the sensor. These areas are never active due to the manufacturing problems. The track fit position that is located in this region is also excluded from the calculation of the efficiency.

Some pixels show excessive noise which cannot be suppressed by higher discriminator thresholds. Those hot pixels were disabled via a software mask applied to the raw data. The position of these pixels is treated as the dead area and same criteria as mentioned above are applied.

4.7.2 Secondary particles

Some secondary particles may produce non-uniform and irregular trajectories that could be misjudged by the tracker. Although the tracks of these

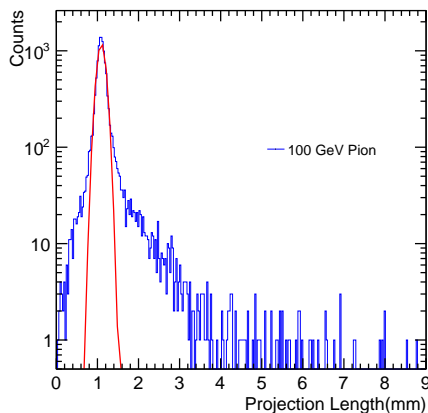


Figure. 4.18: Length projection distribution of 100 GeV pion tracks.

particles could be straight lines as well, they are not the ones produced by the primary pions. Once the secondary particle is generated in the detector, the trajectory of it can be regarded as track by the tracker, these secondary tracks have to be removed.

The distribution of the projection onto the $x - y$ plane of the track length is shown in Figure 4.18. The length is calculated as square root of quadratic sum of residuals in x and y directions from Figure 4.14. A Gaussian fit has been performed to these distributions and mean values of approximately 1.0 mm are extracted, which are related to the inclination of the beam. In addition to the Gaussian peak the distributions have a tail to large values, which is most likely induced by secondary particles. These are eliminated by setting a cut on the projection length. The cut value is chosen to be ≈ 0.32 mm to the 3σ .



Chapter 5

Shower Analysis

5.1 Introduction

One of the main purposes of FoCal is to study the shower properties in unprecedented detail, not only in the longitudinal, but also in the transverse direction. In general, the prototype is designed to precisely measure electromagnetic showers, while the situation for hadronic showers is more complicated and the behaviour is not well understood so far. The behaviour of electrons/photons or hadrons and also the discrimination between them in an electromagnetic calorimeter are interesting questions in calorimetry studies.

In this chapter, several important intermediate analysis steps related to showers produced from different particles (electrons, pions) will be discussed. Only after this can we turn to the final beam test performance results.

5.2 Shower Position Reconstruction

Various formulas have been proposed and compared to determine the shower centre position [23–26,28]. All of them were based on the energy deposition of electrons (or photons) in laterally segmented calorimeters. The centre of gravity method in Equation 5.1 is one of the most common formula to reconstruct the shower centre in a conventional sampling calorimeter.

$$x_c = \frac{\sum_i \omega_i x_i}{\sum_i \omega_i} \quad (5.1)$$

Here the sum runs over the number of blocks in the shower cluster and ω_i is a weight factor depending of the energy. Because the FoCal prototype is a

fully digital calorimeter, and only digital signals can be obtained by the pixel response (0 or 1), our analysis has to be slightly different. The small pixel size should make the shower centre estimate much more precise. The precision of the shower position reconstruction based on centre of gravity method with linear weight and only using selected layers of the detector has been discussed in [34].

In comparison to the simplest linear weighting case, a new weight method with a power weight applied to the amplitude defined as the sum of the hits in a pixel region has been introduced in Section 3.6. This power weight in Equation 3.8 can enhance the significance of the core region of the shower. By cutting on the amplitude for all properly working sensors, the bias from the wide tail of the electromagnetic shower can be suppressed. In this method the weight ω_i is given by

$$\omega_i = \max \{0, A_i - W_0\} \quad (5.2)$$

Here A_i is the amplitude of sum of pixel region i obtained by superimposing all working layers, W_0 is a dimensionless parameter providing a threshold for the amplitude. Consequently, only the pixel regions having an amplitude higher than W_0 are taken into account for calculating the shower centre position. Indeed, high W_0 favours the shower core region but decreases the number of pixel regions used in the calculation, while small W_0 has the drawback that one may bias the centre calculation due to the large number of low amplitude pixel regions. It exists therefore an optimal value for both W_0 and the power t for Equation 3.6, and this will be discussed in the next section.

5.2.1 Parameter optimization

There are two parameters that need to be determined. W_0 allows to set a threshold to calculate the amplitude in the pixel region, while t modifies the weight of the amplitude. The optimization will be performed in the simulation. Based on Equation 5.2, higher W_0 can refine the calculated region but reduces the reconstruction efficiency, especially when the energy of electrons decreases (see Figure 5.1). We hereafter define the *position resolution* as the sigma of the distribution of the residual between the position of the cluster on layer 0 and the calculated shower centre in the x direction. Of course, this can be done in an analogous way for the y direction. The reconstruction efficiency is related to the energy of the particles. For higher W_0 value, the efficiency of reconstructing the position of the shower decreases dramatically. This decrease happens for

lower threshold value, when the electron energy is decreasing. It is desirable to maintain the reconstruction efficiency at a relatively high level ($> 95\%$).

In Figure 5.2, the position resolution decreases first to the optimal value of W_0 and increases again for still larger values for some of the data sets (244, 100, 50 GeV). However, for 30 GeV, the efficiency decreases significantly after $W_0 = 6$, which is a compromise value for 30 GeV electrons. For the low energy data (e.g. 5 GeV), the low number of hits restricts the range of selecting the W_0 value. This case is not shown in this plot.

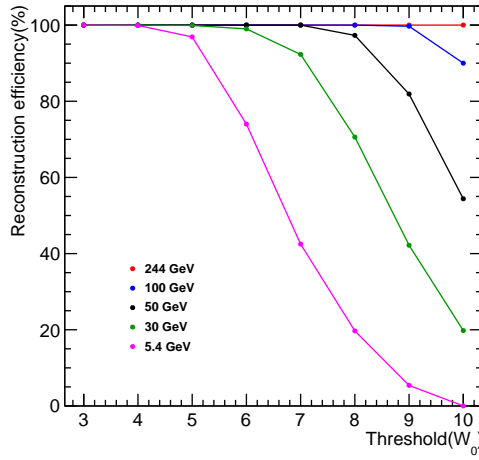


Figure. 5.1: Shower centre reconstruction efficiency as a function of threshold parameter W_0 in the simulation.

The other parameter t , which is the power index to enhance the shower core region of a given shower, can also be optimized through checking the position resolution for different values of t . Figure 5.3 shows the position resolution at different power index t for different energies at fixed $W_0 = 3$. For SPS energies, the trend of the curve shows a moderate decrease for small values followed by a much stronger increase for large values. The higher the energy, the smaller the value of t necessary to obtain the best position resolution. One can note that the differences of the position resolution for different t is relatively small for not too large values of t ($< 5 \mu\text{m}$ for SPS data sets), but larger t values can consume much more computing time for calculating the shower centre. Therefore, we select $t = 2$ for calculating the shower centre.

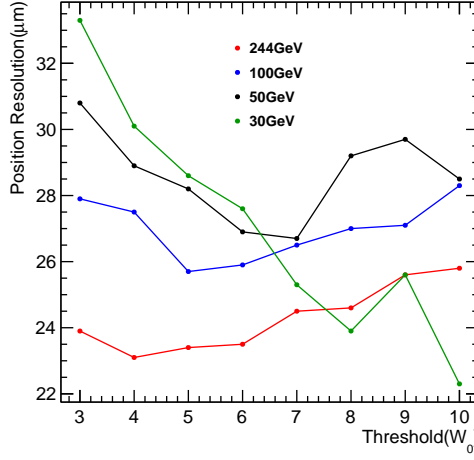


Figure. 5.2: Position resolution as a function of threshold parameter W_0 ($t = 2$) in the simulation.

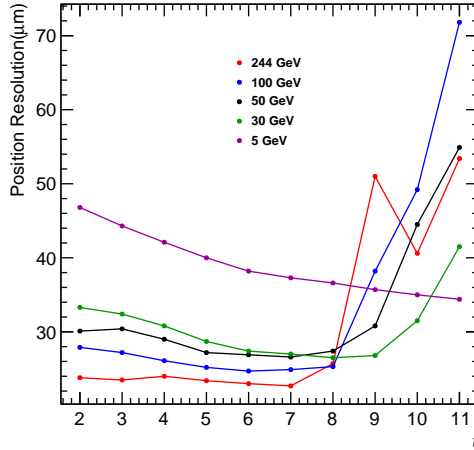


Figure. 5.3: Position resolution as a function of t ($W_0 = 3$) for electrons of different energies in the simulation.

By tuning these two parameters in the simulation, we can obtain the appropriate values for estimating the shower centre in the experimental data and they are summarised in Table 5.1.

Table 5.1: Selected parameters form simulation for shower centre determination.

Energy(GeV)	W_0	t
244	4	2
100	6	2
50	7	2
30	5	2
5.4	3	2

5.2.2 Reconstruction quality

In the previous section, the method of reconstructing the shower centre has been established, in order to check the reconstructed shower centre quality, a verification procedure based on the simulated electrons is performed.

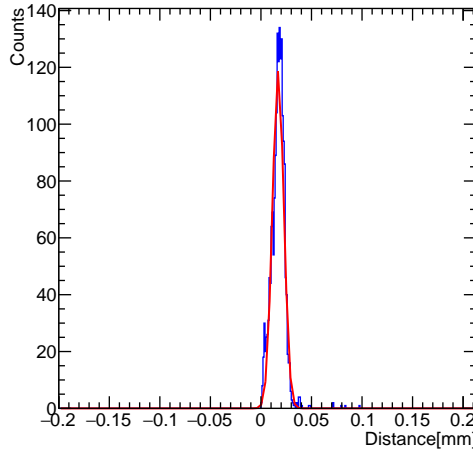


Figure. 5.4: Simulated distance distribution between primary particle and cluster found in layer 0 in for 5 GeV electrons.

The precise positions of incident electrons are known in the simulation, which corresponds to the original position where the primary particles are generated. The precision of the estimate of the particle position from layer 0 can be seen from the distance of the cluster position in layer 0 relative to the true particle position as defined in the simulation. As can be found in Figure 5.4, the width of the distribution is $\sigma = 5.6 \mu\text{m}$ as obtained from Gaussian fit. The mean of the distribution is approximately $16 \mu\text{m}$, which is in line with the $15 \mu\text{m}$ for the coordinates of a pixel according to Equation 3.1. Here we can draw the conclusion that the cluster position is precise enough to be the estimate of primary position.

To verify the method, $W_0 = 3$ and $t = 2$ has been chosen as the parameters for calculating the shower centre. The region of the incident position of electrons covered is $|x| \leq 15 \text{ mm}$ and $|y| \leq 15 \text{ mm}$. The number of electrons for different energies used to verify the quality of the shower centre calculation is summarised in Table 5.2. In order to be close to the realistic situation of the experimental setup, the dead sensors and channels are excluded from the calculation.

Table 5.2: The statistics of different energies to verify the quality of shower centre reconstruction in the simulation.

Energy(GeV)	particle	events
244	e^-	3000
100	e^-	2000
50	e^-	2000
30	e^-	2000
5.4	e^-	2000

Figure 5.5 shows the performance of the shower centre reconstruction for 5.4 GeV and 100 GeV electron data. The strong correlation between the primary incident positions and reconstructed shower centre in the upper panel shows a good agreement. Apparent the bias in the shower position reconstruction seen in previous analysis for coarse granularity is essentially absent for our high-granularity detector. The bottom panel in Figure 5.5 shows the residual between the calculated shower centre and the primary incident position extracted from the primary particles in the simulation. The width of the projection along the y axis gives the precision of the reconstructed shower centre in the simulation. We obtain for 5.4 GeV $\sigma = 120 \mu\text{m}$ and for 100 GeV $\sigma = 42 \mu\text{m}$.

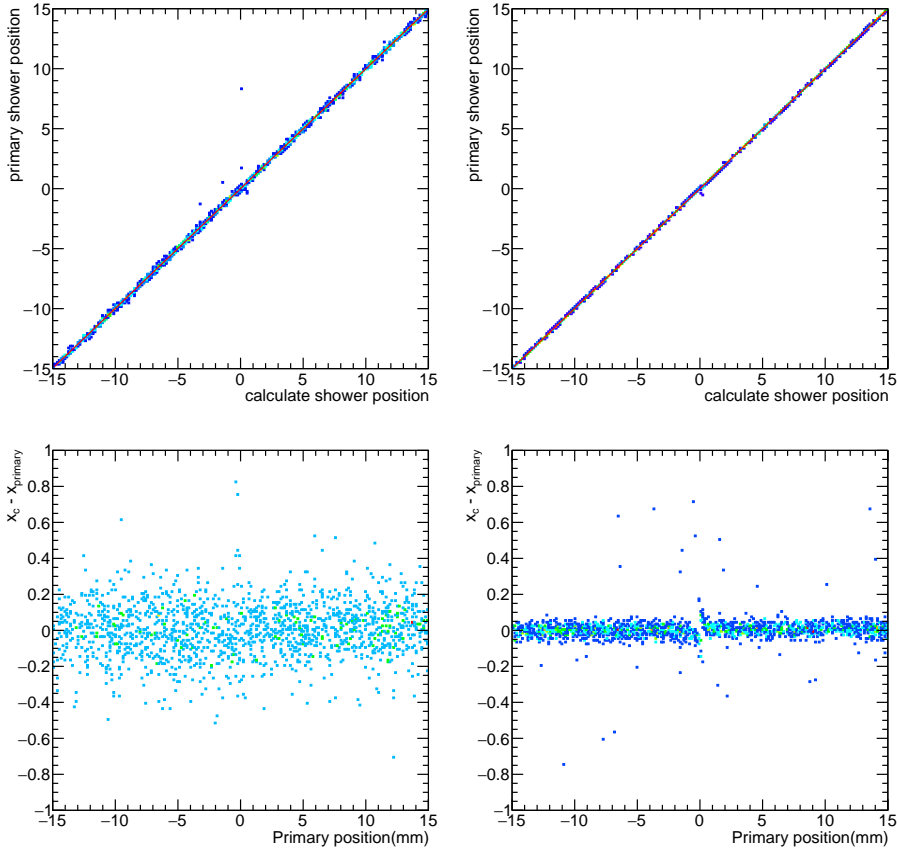


Figure. 5.5: Shower position reconstruction quality for 5.4 GeV (upper left) and 100 GeV (upper right) simulated electrons. Residual between primary shower centre and reconstructed shower centre for 5.4 GeV (bottom left) and 100 GeV (bottom right). Note: the gap and overlap regions are also taken into account.

5.3 e/π Separation

The electromagnetic shower induced by electrons or photons behaves considerably differently from the principle of showers induced by hadrons. e.g. pions or protons. We can conduct the particle identification studies based on the various information provided by high granularity calorimeter. For a typical electromagnetic calorimeter with tens of radiation length, a large fraction of hadrons will generally deposit much less energy than electrons/photons, and

in a realistic measurement situation this already helps to suppress the contamination from hadrons for a photon measurement. Further discrimination can be obtained from the shape of the shower. The longitudinal and lateral development of electromagnetic showers and hadronic showers should allow such a separation. High Z materials are considered to be good options for absorbers in a calorimeter since there is large difference between λ_I (nuclear interaction length) for hadronic process and the radiation length for electromagnetic process. In this section, the contamination by pions in the mixed beam of SPS beam test will be estimated, and after this, several different methods which can potentially provide separation power on electrons and pions are also discussed.

5.3.1 Pion contamination in test beam

The beam particles at DESY are pure electrons, while the SPS test beam contains a mixture of pion and electrons. Although the lateral size of the FoCal prototype is $3.84 \text{ cm} \times 3.84 \text{ cm}$, which is not wide enough for most hadron showers to be fully contained, still there is a small fraction of hadrons interacting in one of the early layers and depositing a large fraction of their energy in the detector. These hadrons may contaminate the full energy peak of electrons. In this section, the contamination of hadronic showers in the electron peak are estimated.

The template of the number of hits distributions for pions and electrons are individually obtained from a simulation in Geant4. Charge diffusion also has been implemented in the simulation. The contamination was estimated by a MC template fit, which allows to estimate the fractional contamination by pions. The fit results are shown in Figure 5.6.

The estimates of pion contamination in the SPS test beam can be found in Tab. 5.3. The contamination of the electron peak by pions in the SPS data sets are less than 1%, which can be neglected in the analysis.

Table 5.3: Pion contamination estimation of SPS test beam data.

energy(GeV)	fit range	hits cut	pion left	contamination(%)
30	150-70000	5800	24	0.2
50	300-70000	9500	39	0.3
100	1200-70000	18000	216	1.0
244	900-70000	40000	55	0.9

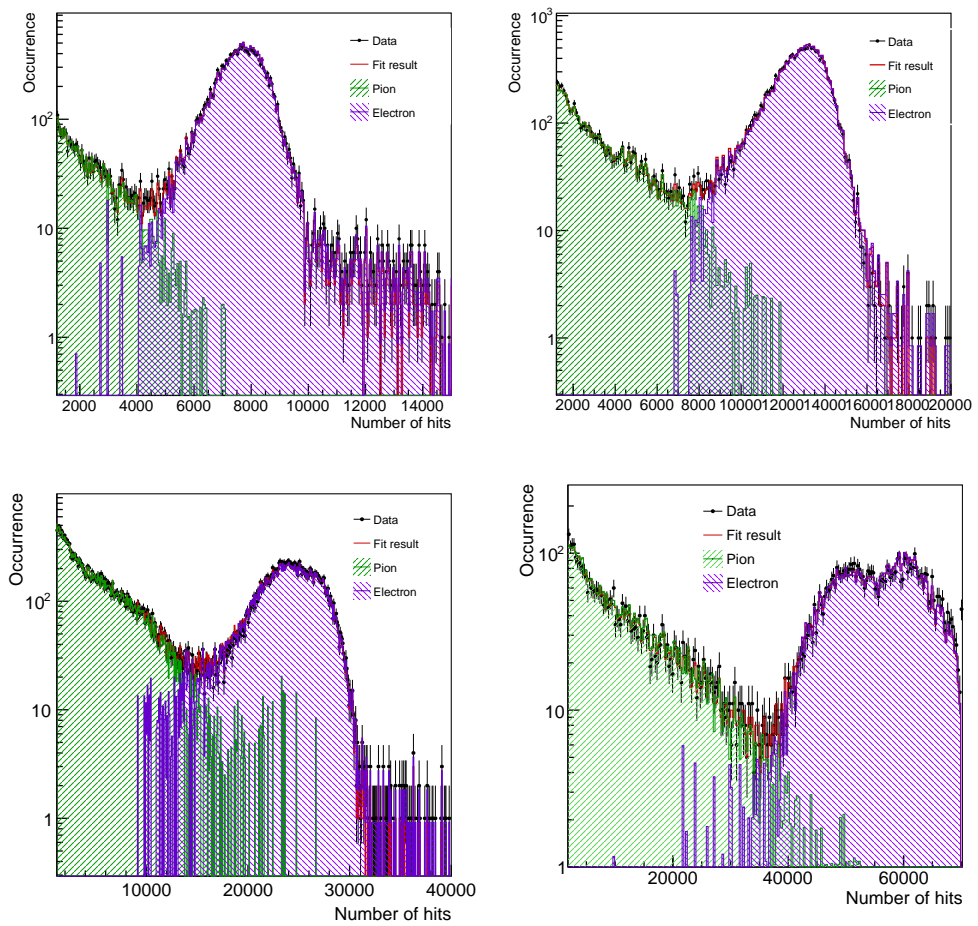


Figure. 5.6: Estimation of pion contamination by decomposing the spectrum of 30 GeV (upper left), 50 GeV (upper right), 100 GeV (bottom left) and 244 GeV (bottom right) of raw data.

Although the pion contamination in test beam data can be negligible, it is still interesting to conduct studies on electron hadron (e/h) separation capability in the high granularity calorimeter. The unprecedented detail of the shower development may provide a potentially unique e/h separating power. In the next section, we will discuss several methods to separate electrons and pions based on the longitudinal and transverse distribution of showers in the FoCal prototype.

In the following sections, the simulated and experimental data will be used for the separation analysis and discussion. The particle type is known in the simulation. However in the experimental data, to separate the electrons and pions, we simply use the cut on the number of hits, which has been listed in Table 5.3. To treat the simulation in the same way, this cut is also implemented in the simulation.

5.3.2 Longitudinal parameters

The average probability of a photon to generate electron and positron pairs when passing through material of $1 X_0$ thickness is around 55%, which means 90% of electrons will start to produce shower particles within $4 X_0$. Because of the nature of the strong interaction, hadronic showers are much more complicated than electromagnetic ones. On average, the probability that a hadron traverses a distance z in a heavy material without causing a nuclear interaction equals [30]:

$$P = \exp(-z/\lambda_{int}) \quad (5.3)$$

The total interaction length of the FoCal prototype is approximately $1 \lambda_{int}$. With a large ratio of $X_0/\lambda_{int} \approx 28$, the probability of charged pions to produce a shower in the detector within $4 X_0$ is 0.6 %.

The fine granularity of the prototype enables one to identify the point at which the incident particle makes its primary interaction. The significant difference of interaction length and radiation length makes the shower starting point different between electrons and pions, which may be useful as the longitudinal information to identify the different types of particles.

The precise shower centre reconstruction for electrons has been proved in section 5.2. To identify the interaction layer of a shower based on the shower centre reconstruction, a dedicated criterion is established as follows:

- For every event, first obtain the shower centre which has been described in Section 3.6.

- Calculate the number of hits N_r^l within $r = 1$ mm relative to the shower centre for all the layers.
- If there are at least 3 layers or 2 consecutive layers with N_r^l more than 30 hits between the layers $[l, l + 4]$, while N_r^l is less than 30 hits before layer l , then layer l is identified as the interaction layer of the shower.

We use the N_r^l with the search radius $r = 1$ mm around the reconstructed shower centre instead of all the number of hits in the layer. There are several reasons for this. Firstly, the malfunction sensors, channels or pixels induce large uncertainties of the number of hits in the layer, while using small search radius reduces these uncertainties. Secondly, the average number of noise hits N_r^l in the search radius is approximately 0.03, while the average number of hits is several order of magnitudes higher than the noise rate, which leads to a better signal to noise ratio.

In principle, the shower centre reconstruction method works better for electrons than hadrons, and the efficiency of shower centre reconstruction can be better than 95 % for electrons. Therefore the interaction layer of electrons are easier identified than hadrons. The interaction point distribution as a function of number of hits for simulated data and experimental data are shown in Figure 5.7. The calculation of the number of hits after calibration can be found in Section 3.8. The electrons in both experimental and simulated data show values which concentrate in narrow regions for both of the parameters. Electron showers have an early start at the beginning of the detector and they always deposit essentially all of their energy leading to a strong constraint on the number of hits. The latter fact can be observed clearly in the simulation, it should be noted, however, that in this analysis a cut has been imposed on the raw number of hits to minimize any contamination from pions in the experimental sample. For SPS test beam energies, the interaction layer is rarely the 5th or a later layer for most of the electron events.

The energy deposition of hadronic showers varies event by event and some of them have inhomogeneous shower transverse development in the detector. The interaction layer as a function of the number of hits of pions for simulation and experimental data are given in Figure 5.8 and 5.9. The interaction layers of the events for which the centre cannot be well defined by the algorithm or the interaction layer cannot be identified within the first 20 layers are treated as interacting beyond the detector and they are filled in the 25th bin of the histograms. Because of the high efficiency of identifying the interaction layers of electrons, these hadron events do not influence the separation between electrons and pions. In fact, the observation that no interaction layer can be found assures us that these cannot be electron events. As shown in these plots, the earlier the

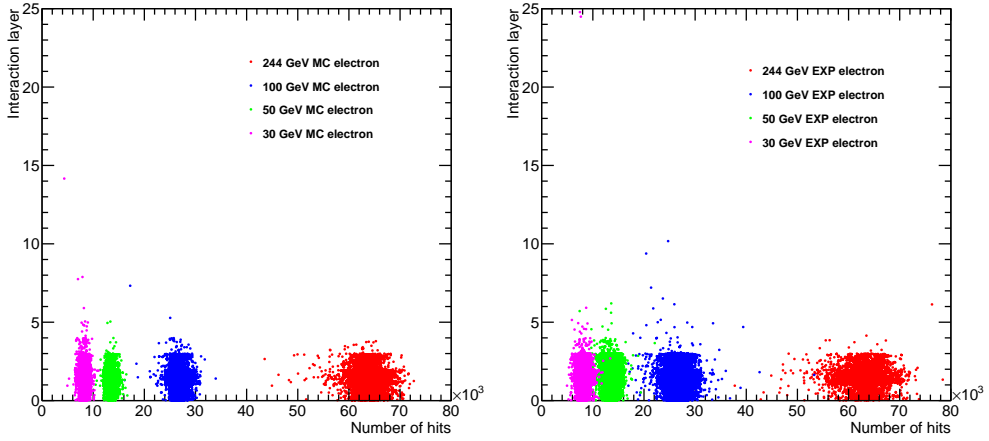


Figure 5.7: Interaction layer as a function of the number of hits of SPS energies for electrons from simulation (left) and experimental (right) data.

hadrons start to produce a shower, the more hits they generate in the detector. Hadrons very rarely deposit all of their energy, so particles of known energy (as in a test beam) can be easily distinguished from electrons just by their number of hits. This leads to a strong suppression of hadrons at a fixed energy. However, hadrons of high energy have a significant probability to generate the same number of hits as a lower energy electron. E.g. a shower from a 100 GeV pion may produce as many hits as a 30 GeV electron. However only a small fraction of the pions start to shower in the first 4 layers, which may provide separation power to electrons for a wide range of energies.

5.3.3 Transverse parameters

Hadron showers likely also have a different lateral development as compared to electron showers. This might also be useful for discrimination. It could be particularly useful, because some of the pions may start to produce a shower in the early layers. These cases are difficult to be separated by only using the starting layer. The lateral hit density profile (“lateral profile” in the later discussion), which contains the information of the shower development in the transverse direction, may provide useful information for separation, because the mechanism of hadronic showers is fundamentally different from electromagnetic showers. The difference of development in transverse direction can

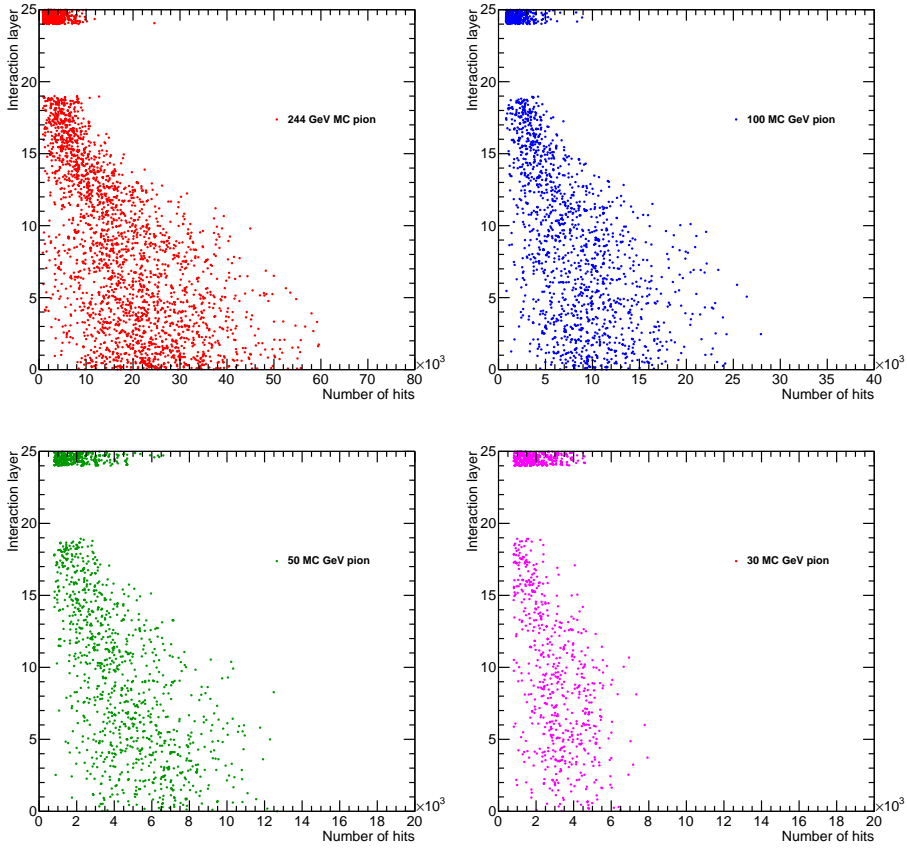


Figure. 5.8: Interaction layer as a function of the number of hits of SPS energies for simulated pions.

be reflected by the slope of the lateral hit density profile close to the shower core region. Since the shape of the lateral profile extracted from different depths of the detector varies. In order to reduce the fluctuations of the lateral hit density profile event-by-event, the detector is divided into four parts, every of them contains 6 consecutive layers, which are called a “segment” and marked with numbers from 0 to 3.

To fit the inner part of the lateral hit density profile (ρ_i) for a given segment i ($i = 0, 1, 2, 3$), we use the equation:

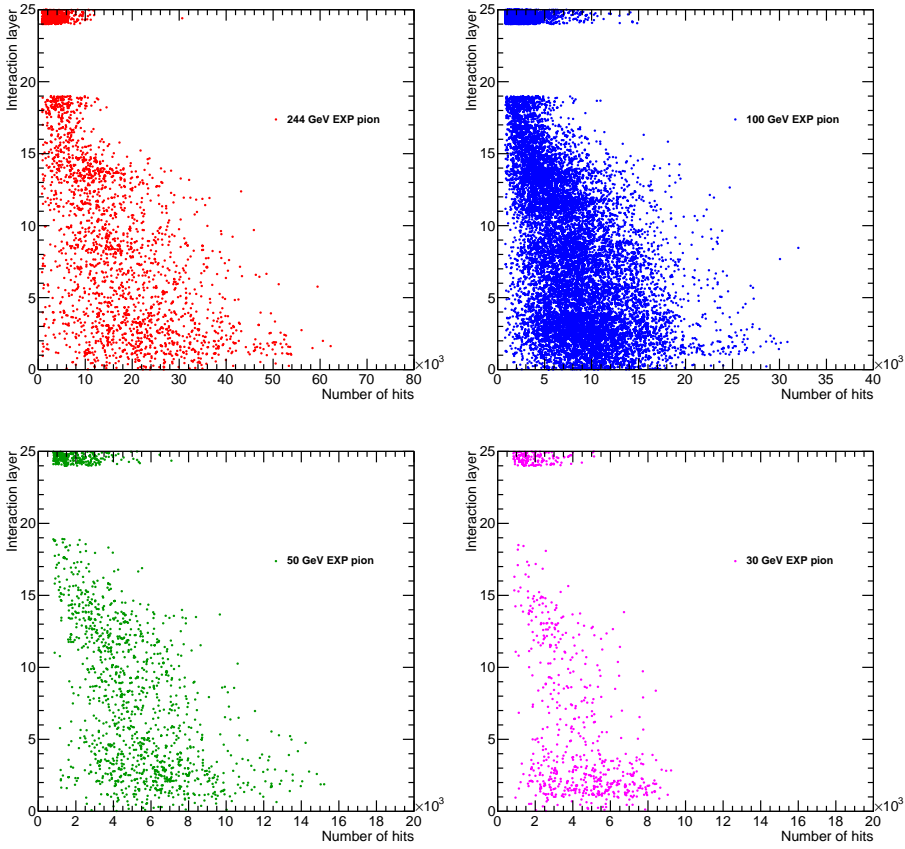


Figure. 5.9: Interaction layer as a function of the number of hits of SPS energies for experimental pions.

$$\log_{10} \rho_i(r) \cdot (\text{mm}^2) = a \times r + b \quad (5.4)$$

Here parameter a represents the slope of the inner part and b is related to the amplitude of the hit density at the shower centre. The steeper the lateral profile, the smaller is the value of a . Because the steepest part of the lateral profile is close to the shower core, the fitting range of the lateral profile of all the following analysis will be fixed from 0 to 5 mm from the shower centre¹.

¹A cylinder of $r = 5\text{mm}$ around the shower centre contains $\approx 75\%$ of all the hits [34].

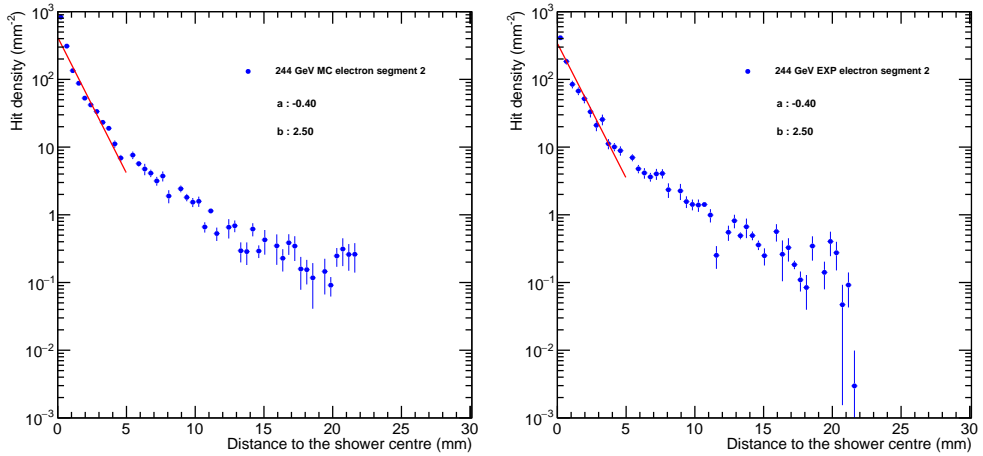


Figure. 5.10: Examples of lateral profile of segment 2 fit for 244 GeV single simulated (left) and experimental (right) electron event using Equation 5.4.

Figure 5.10 shows some typical examples of the fit for electrons by using Equation 5.4 in simulated and experimental data. The shapes of the electrons in these data sets show stable fit results and relatively small fluctuations. Similar fits using pion data are shown in Figure 5.11². There are 3 typical cases in this figure. The pions which show similar behaviour to electrons are shown in the upper panel. The middle panels show a flatter transverse shower development and the bottom panel indicates that the shower can also start at a very later layer, leading to a barely developed distribution. These possible variation in the distribution for pions will lead to a broader distributions of the a and b values.

The a and b parameters as a function of the number of hits extracted from fit of the lateral profiles of the different segments for different particles are shown in Figure 5.12 to 5.15. Since for some showers the distributions cannot be well fitted by Equation 5.4, the parameter a or b for these cases are fixed to a value of 9 in the histogram. The events with the number of hits below 1000 after calibration are treated as tracks and are excluded from fit. As can be seen in these plots, for electron data:

1. The distributions of parameter a for segment 1 and 2 (layer 6-11, 12-17) are narrower than for the other segments. This is due to the relative small

²Similar figures for the segment 3 are not shown here, but can be found in appendix

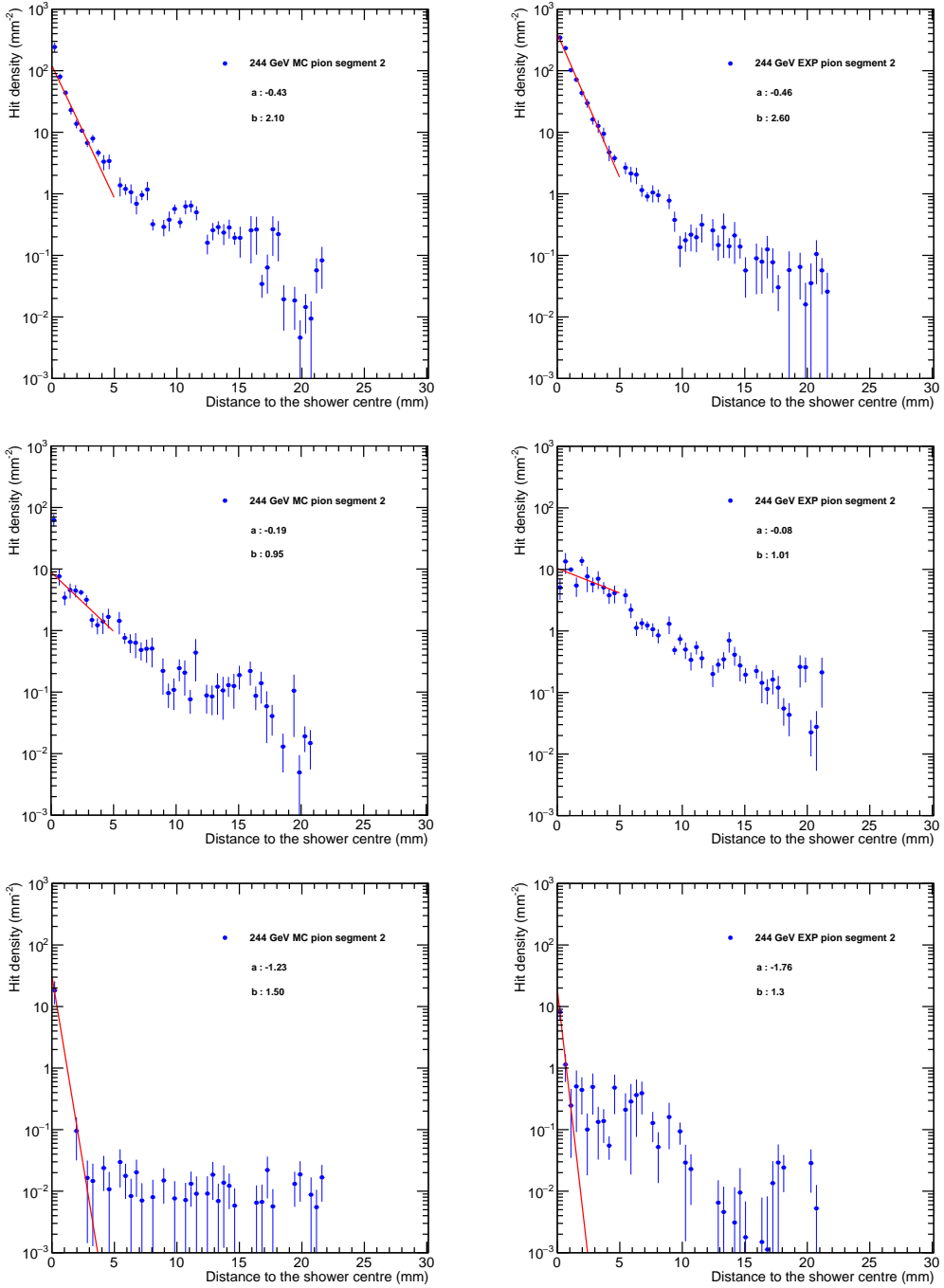


Figure. 5.11: Examples of lateral profile fit for 244 GeV single simulated (left) and experimental (right) pion event using Equation 5.4. Three different typical situations are shown in upper, middle and bottom panels.

number of hits in the beginning and end layers of the detector, which increase the fluctuation of the fit results.

2. Related to the smaller fluctuations, the mean values of a distributions for segment 1 and 2 show a consistent width for different energies than other segments. For the third segment, the distributions also begin to suffer from the lower number of hits for low energy, so the distributions tend to be broader at low energy for this segment.
3. Because the b parameter represents the amplitude of the hit density in the shower core region, the distributions demonstrate an energy dependence for all the segments. Again this is most easily seen for segments 1 and 2.
4. The electrons from experimental data show distributions for both a and b parameters for the first 3 segments. The statistical uncertainties in the experimental data are larger than in the simulation.
5. In general, the agreement between the simulation and the experimental data is reasonably good, with increasing discrepancies for the last segment.

For the pions one observes the following behaviour:

1. The distributions of parameter a are wider than those of electrons for all the segments.
2. For the b parameters, the pions show larger fluctuations than electrons in segment 1 and 2, which is because the shower may start in a different segment of the detector. This will lead to the broader distribution of the b value.
3. The unsuccessful fitting results in the data are to a large extent due to an inefficient shower centre reconstruction, especially for the events, which generate low number of hits in the detector.
4. The agreement between simulation and experimental data is in general not as good for pions as it is for electrons.

5.3.4 Determination of separation parameters

We have discussed the parameter values extracted from the shower shape in the previous section, the parameters which will be used in the separation will be determined in this section.

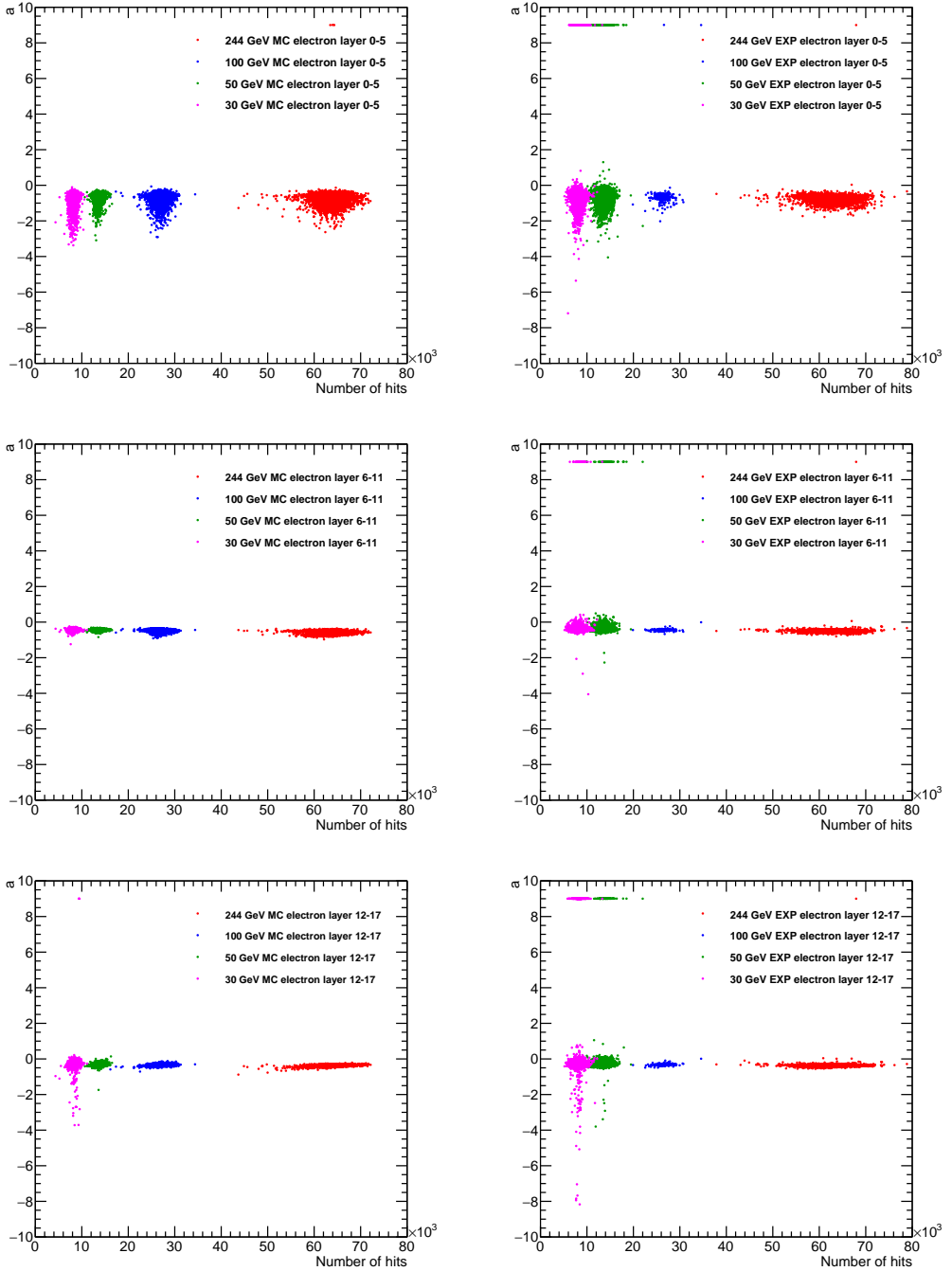


Figure. 5.12: Distribution of parameter a as a function of the number of hits of simulated (left column) and experimental (right column) electrons for the different segments in the detector. Different colours represent different energies.

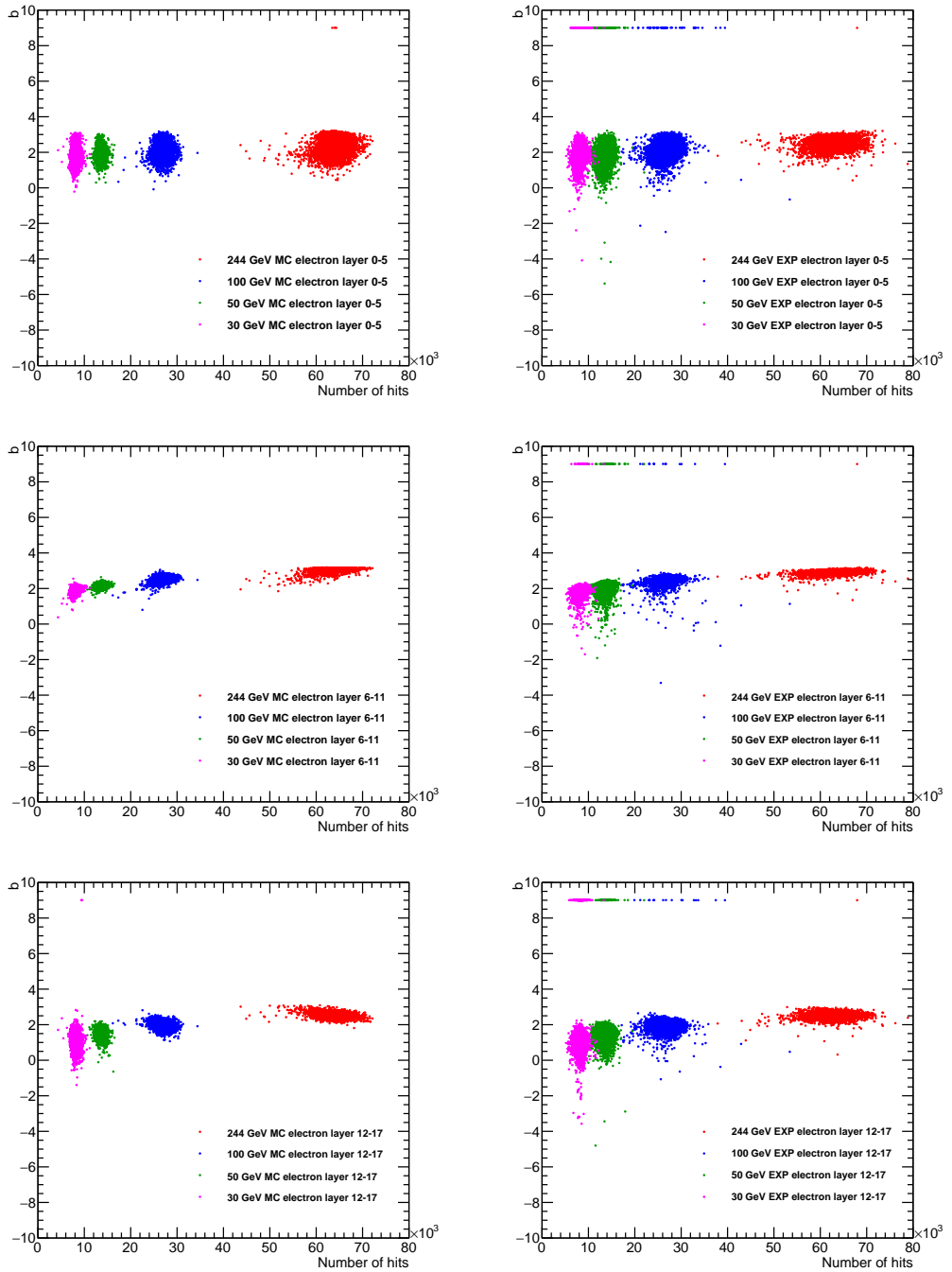


Figure. 5.13: Distribution of parameter b as a function of the number of hits of simulated (left column) and experimental (right column) electrons for the different segments in the detector. Different colours represent different energies.

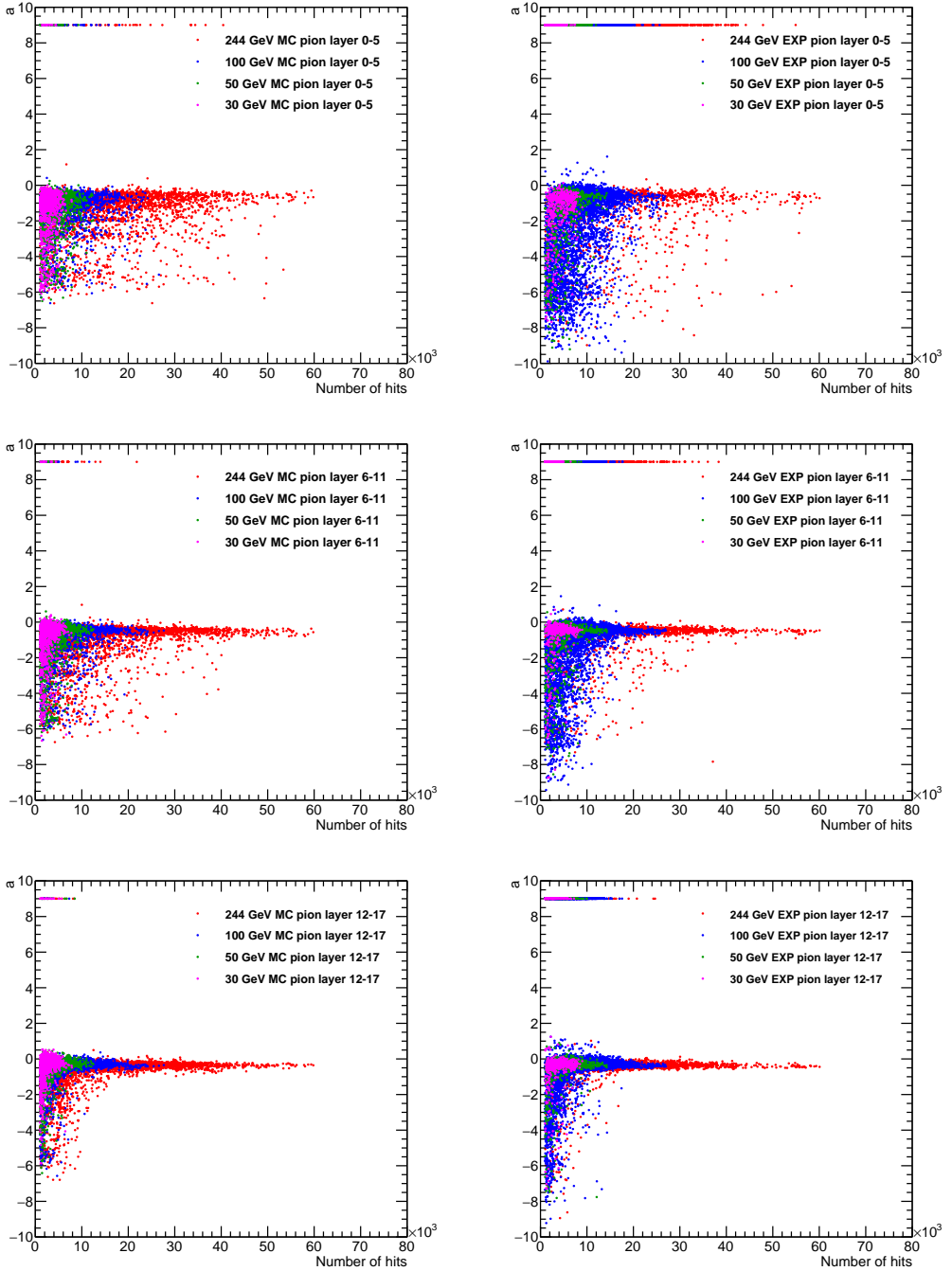


Figure. 5.14: Distribution of parameter a as a function of the number of hits of simulated (left column) and experimental (right column) pions for the different segments in the detector. Different colours represent different energies.

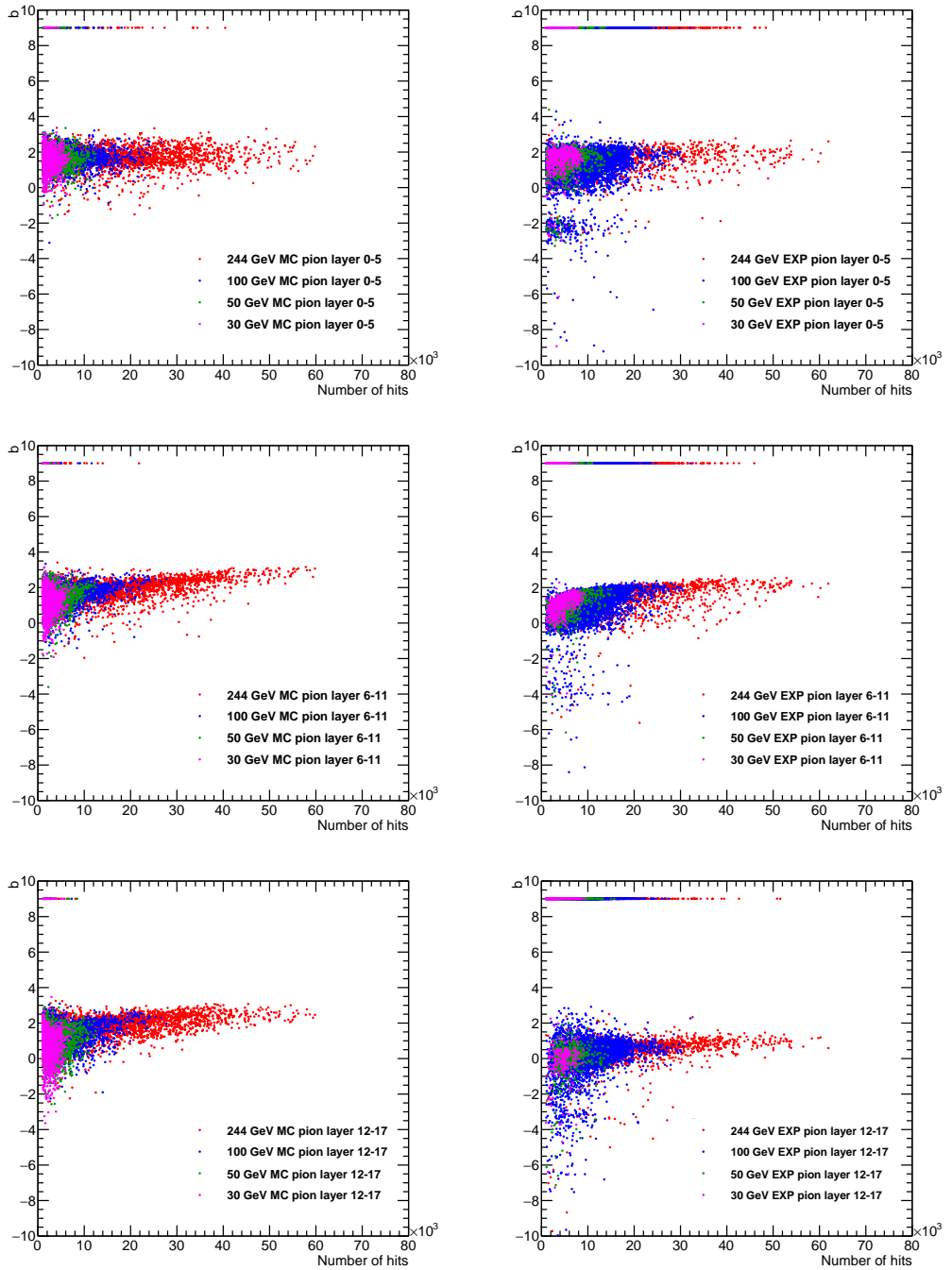


Figure. 5.15: Distribution of parameter b as a function of the number of hits of simulated (left column) and experimental (right column) pions for the different segments in the detector. Different colours represent different energies.

The shower interaction layer, which is energy independent, is able to provide discrimination power for the different particles. In addition to the interaction layers, we can also use the lateral parameter cut to enhance the discrimination power.

To clarify the way the separation due to the interaction layer works, Figure 5.16 shows the distribution of the interaction layer for pions of two energies (50 and 244 GeV). In both cases, only showers that generate a number of hits similar to that for electrons of 30 GeV have been chosen, which selects only a small fraction of all pion events. The left panel shows results of the simulation and the right panels those for experimental data. The simulation agrees reasonably well with the data.

While electrons would essentially all have an interaction in one of the first four layers, it can be seen that pions have a significant probability to have the shower start in a later layer. The late interaction probability is significant, but not very large for the 50 GeV electrons – apparently for those electrons to deposit 60% of their energy in the detector, requires them to look relatively similar to electromagnetic showers. For 244 GeV, most of the pions have a late shower start, which relates to the fact that they deposit only a small fraction of their energy.

The a parameter for the electrons in the segment 1 and 2 show less energy dependence and also a narrow distribution for different energies in both simulated and experiment data in Figure 5.12. We will therefore look in more detail at the results from these two segments. In order to determine the cut values for different energies, the one-dimensional distributions of a are fitted by Gaussians. The mean and sigma values of the fit are plotted in Figure 5.17 for both data and simulation. In addition a linear fit is plotted. There is a slight discrepancy between the experiment and the simulation for segment 1, while the agreement is perfect for segment 2. We will therefore base our discrimination on the fits in segment 2.

The types of particles in the simulated data are known. We will use the lateral profile determined in the segment 2 of simulated data for the discrimination, which will be discussed in the later section. We define an interval $[a_-, a_+]$ to select electromagnetic showers, where:

$$\begin{aligned} a_{\pm} &\equiv \bar{a} \pm 2\sigma_a \\ &= p_0 + p_1 N_{\text{hits}} \pm [p_2 + p_3 \cdot \exp(p_4 \cdot N_{\text{hits}})] . \end{aligned} \quad (5.5)$$

These parametrisation are fitted to the upper and lower 2σ bounds shown in Figure 5.17 as dashed line and provide an energy-dependent set of selection

criteria. The fit values are summarised in Table 5.4.

Table 5.4: Fit results of prediction values for cut on a from simulated data.

parameter	value
p_0	-0.3 ± 0.098
p_1	$(-8 \pm 2) \times 10^{-7}$
p_2	0.075 ± 0.004
p_3	0.28 ± 0.05
p_4	$(-1.4 \pm 0.2) \times 10^{-4}$

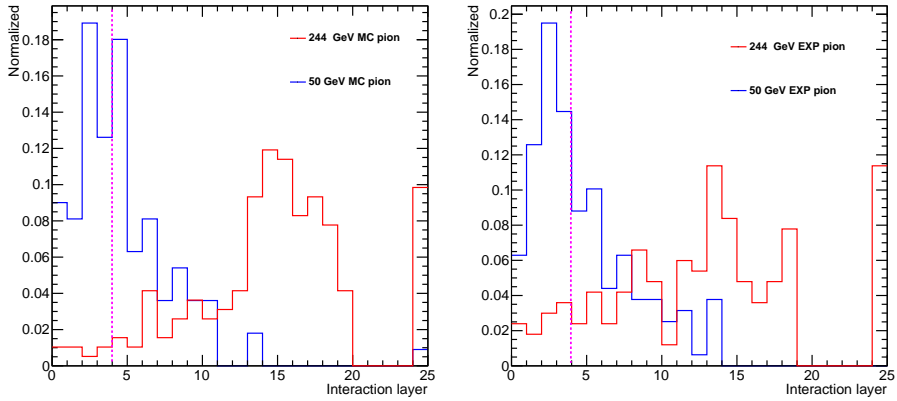


Figure. 5.16: Interaction layer distributions for 50 GeV (blue) and 244 GeV (red) pions with the number of hits similar to 30 GeV electrons. The magenta dashed line indicates the cut on the interaction layer for discriminating electrons and pions.

5.3.5 Separation power verification

We have established cuts on the longitudinal and the transverse distribution of the number of hits to discriminate electromagnetic and hadronic showers by studying particles of specific energies. These cuts can be applied both independently and combined. The performance will be judged below in a more realistic simulation using a continuous distribution of particle energies, as will be the case in future measurements. For these simulations, the particle spectra

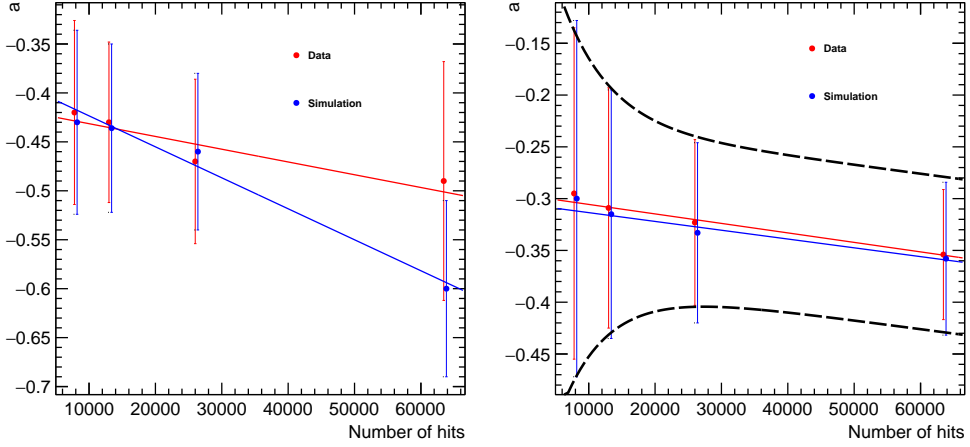


Figure. 5.17: Parameters a extracted from lateral profile fit of segment 1 (layer 6-11) and 2 (layer 12-17) for simulation and experimental data, the error bar is the 2σ of the distribution by applying the Gaussian fit. The data points are shifted between simulation and experimental data for visibility.

should be close to those in expected in Pb-Pb collisions at the LHC. The momentum spectrum of charged pions as measured by ALICE at $\sqrt{s} = 2.76$ TeV can be fitted with a modified exponential function:

$$\frac{d^2N}{dydp_T} = c \times (e^{(a \times p_T - |b| \times p_T^2)})^d \quad (5.6)$$

Table 5.5: Parameters of the fit of the charged pion spectrum.

a	b	c	d
-0.767	0.010	439.6	-5.908

Table 5.5 shows the parameters used for fitting the charged pion spectrum.

In these simulations a detector similar to our prototype is at 7 m away from the interaction point. We use a fixed rapidity of $y = 1.5$ and study the charged pion yield as a function of p_T . 100000 charged positive pions events were generated uniformly according to a probability distribution following Equation 5.6 for identification purpose. We discard the events with incident positions close to the edge of the detector, i.e. we require a particle incident position

selection of $|x| \leq 1.5$ cm, $|y| \leq 1.5$ cm. 55873 charged positive pions events were left. The separation power results will be discussed in Section 6.5.

5.4 Calibration Optimization

5.4.1 Motivation of optimization

The detailed calibration procedure has been discussed in the thesis of Chunhui Zhang [34]. However, there are still several open issues remaining to discuss, some of which may leave room for further optimization, and they can be listed as follows:

- The shower centre selection for SPS data sets is $|x_c| \leq 1.0$ cm, $|y_c| \leq 1.0$ cm.
- Quadrant 1 was not included in the final result (e.g. linearity and energy resolution).
- There are situations where extrapolation into the dead areas does not work properly.
- There is an obvious discrepancy between the experimental data and the simulation (e.g. energy resolution).

The sensitivity calibration within a layer has been introduced in Section 3.8. The calibration factors are obtained by equalizing the hit density profile of the 4 quadrants within the layer. For well equalized sensors the average response $M_{l,q}(R, \langle \rho_{l,q} \rangle)$ of electromagnetic showers on a certain sensor should be independent of the shower centre location. In this context we characterize the location of the shower via a variable $p_{l,q}$, which is the fraction of working pixels belonging to a certain sensor located in layer l and quadrant q of all pixels in a circular area around the shower centre.

$$p_{l,q} = \frac{N_{l,q}^{working}}{N_{all}^r} \quad (5.7)$$

where $N_{l,q}^{working}$ is the number of working pixels on layer l and quadrant q , while N_{all}^r is the total number of pixels, both calculated in the radius $r = 10$ mm around the centre of an individual shower. There are two reasons for setting a fixed radius r . The first is that the size of a sensor is 1.92×1.92 cm², the selected shower circular part of a shower can be contained in one sensor. The other reason is that the R_M ($R_M = 11$ mm) contains 90% shower hits and the

resolution and response of electromagnetic showers are hardly affected down to half R_M [34].

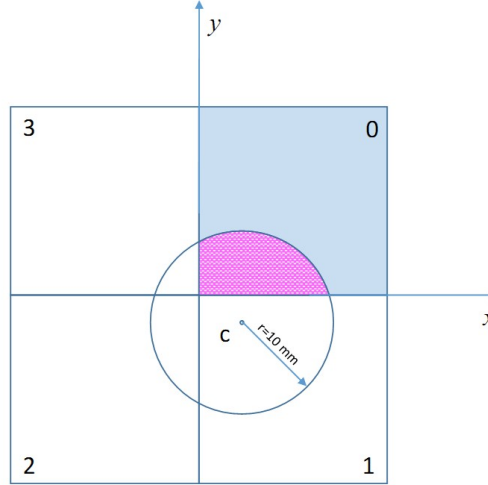


Figure. 5.18: Schematic of calculating percentile of a shower in a individual quadrant 0. The red area is the effective area that can be used for calculating the hits density profile.

Figure 5.18 shows the schematic diagram of the method to calculate the value of $p_{l,q}$ for a given quadrant 0. In this case only the information in quadrant 0 for a given shower can be used to obtain the hit density profile, which means that showers located in different positions may contribute different sampling uncertainties. The higher the value of $p_{l,q}$, the closer the shower is to the centre of the quadrant, while lower value means that shower is close to the edge. In other words, different parts of the hit information can be used for the calibration of the sensors within the same layer.

An assumption in the calibration procedure is that the electromagnetic shower is uniformly developing in the transverse direction – it shows a rotation symmetry around the shower centre. Independent of the fraction of effective area (value of $p_{l,q}$) used in the hits density profile, the hits density is supposed to be stabilized. Figure 5.19 shows the average layer response as a function of $p_{l,q}$ for two individual layers before and after additional optimization, however, the average layer response is not independent of $p_{l,q}$. There are discrepancies up to

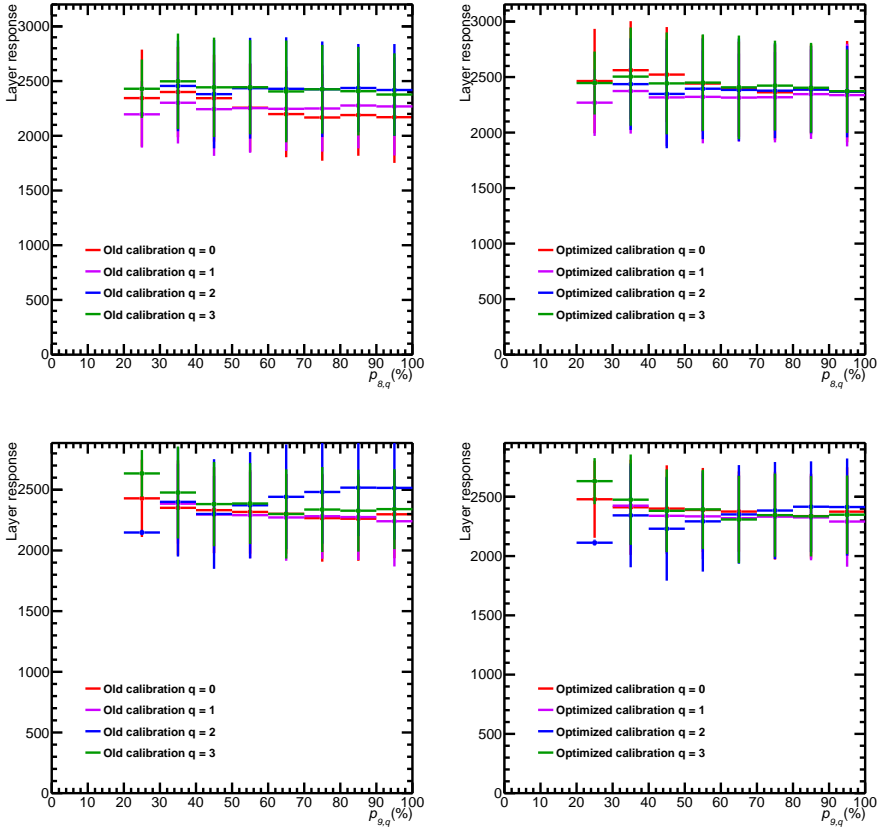


Figure. 5.19: Layer response as a function of varying values of $p_{l,q}$ of old calibration (left) and optimized calibration (right) for layer 8 (upper row) and layer 9 (bottom row).

10%. This effect shows that using only a small part of a shower used to calculate the hit density profile can introduce a bias on the average response of that layer, which will lead to a bias of energy response and deteriorate the energy resolution and linearity. Those events which are located close to the centre of the quadrant give more consistent response, which reflects the actual sensitivity of the sensor.

5.4.2 Optimization procedure

The equalization of the sensors in a layer relies on the cumulative hit density profile of the corresponding sensors. To get the best estimation of the layer

response and also obtain the most precise calibration factors, it is necessary to do an event selection according to the relative position of the shower on the sensor, as characterized by $p_{l,q}$. Figure 5.20 indicates the statistics of the different values of $p_{l,q}$ for the 4 quadrants for an energy of 100 GeV. One can see that most of the electrons for 100 GeV data are only partially ($p_{l,q} = 50\%$) contained in the quadrant. In addition, there are events with considerably lower $p_{l,q}$ values, which account for 30%. These need to be excluded from the calibration, and it leaves us with the events located in the centre ($p_{l,q} > 80\%$) to be used in the optimization of the calibration.

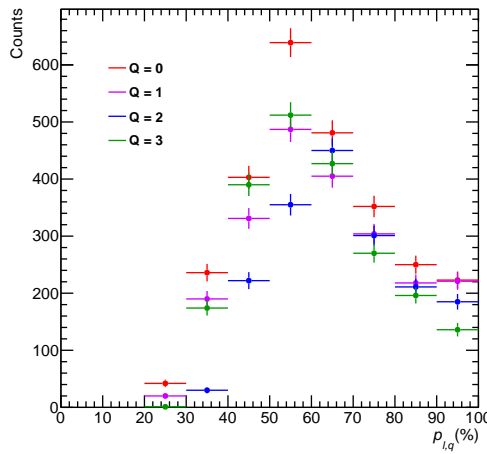


Figure. 5.20: Statistics of 100 GeV SPS data in different quadrants for different values of $p_{l,q}$.

The comparison of the calibration constants before and after optimization is shown in Figure 5.21. The significant differences at early and late layers of the detector are due to the relatively low response and a consequently larger role of the noise in the calibration, which leads to a large uncertainty on the calibration constants. This does not generate significant uncertainties on the final response, because the number of hits in these layers contribute less than 0.5% of the total number of hits for 100 GeV.

5.4.3 Calibration quality

The calibration procedure and quality based on the hit density profile has been discussed in [34], which will be called “old calibration” in the following discussion.

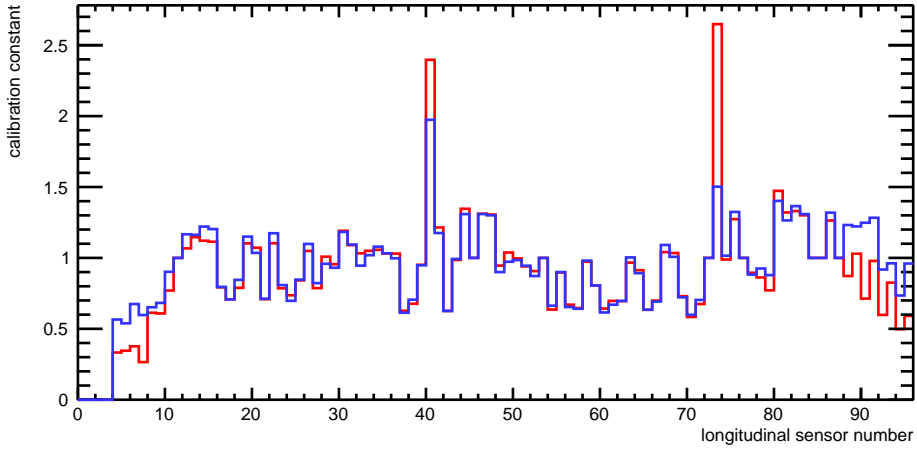


Figure 5.21: Calibration constant comparison before (blue) and after (red) optimization.

The layer response for a given event after calibration has been defined in Equation 3.13. If the calibration is successfully performed, the relative variation of the layer response for different shower positions within a layer should be small. Figure 5.19 shows the layer response of different quadrants as a function of the value of $p_{l,q}$ in layer 8 and 9 which are the layers with all functioning sensors and also close to the shower maximum. Actually, the calibration constants can only translate the response but without changing the trend of the data. The optimized calibration reduces the deviation of the response in quadrants for the majority of the data ($p_{l,q} > 50\%$). There are differences for the region of low values of $p_{l,q}$, which cannot be fully corrected by this procedure.

The detector performance results with the optimized calibration will be shown in Chapter 6.



Chapter 6

Results and Discussion

6.1 Introduction

The methods and procedures of the test beam data and the cosmic data have been introduced and discussed in the previous chapters. In this chapter, the results of analyses based on these data will be shown. The results will focus on the performance of the prototype in either energy measurements or position determination. In addition, the electron hadron separation power by using such a high granularity calorimeter will also be discussed in this chapter.

6.2 Measured Sensor Efficiency

The procedures to obtain the sensor efficiency has been discussed in Section 4.7. Due to the multiple scattering effect which has been introduced in Section 4.6, the low energy muons will make the efficiency decrease. Therefore, the SPS pion data at 100 GeV and 244 GeV will be used in the sensor efficiency measurements.

Figure 6.1 shows the efficiency measured with 100 GeV and 244 GeV pion tracks, using the method described in the Section 4.7. It can be seen from figure that the efficiencies of most of the sensors are above 96% for both of the energies. The 3 different types of sensors show different detection efficiencies, in particular the sensors with a $14\text{ }\mu\text{m}$ $10\text{ }\Omega\cdot\text{cm}$ epitaxial layer show significantly lower efficiency than the other two types of sensors. In addition, there are some sensors with $15\text{ }\mu\text{m}$ $400\Omega\cdot\text{cm}$ or $20\text{ }\mu\text{m}$ $400\Omega\cdot\text{cm}$ epitaxial layers, which also show a low efficiency. This is due to inappropriate threshold settings of the discriminators.

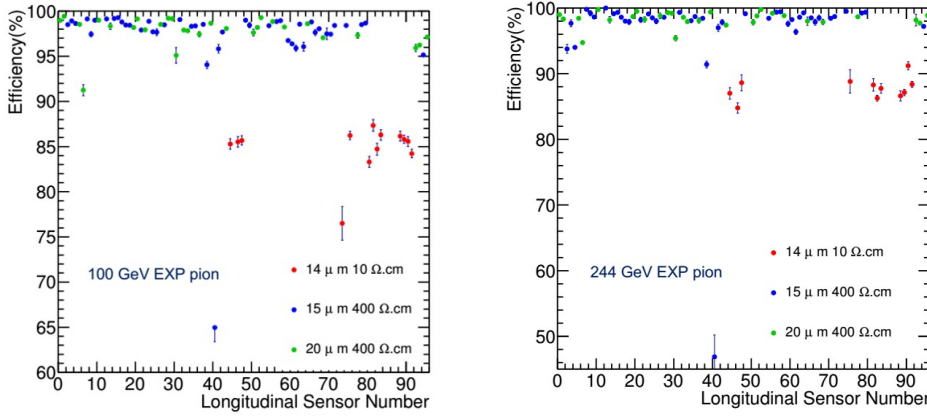


Figure. 6.1: Detection efficiency of all sensors for pions of 100 GeV/c (left) and 244 GeV/c (right).

6.3 Detector Response

Detector response is defined as the number of hits generated by the energy deposited by a particle and can be expressed by the Equation 3.14.

In the prototype, the hits in dead pixels, channels and sensors can not be recovered directly, but can be extrapolated by making use of the radial symmetry of the shower profile and calculating the integral of the lateral hit density profile layer by layer. For layers that are completely dead, the average of the layers before and after it is used. The layer 0 has been excluded from calculating the response since there is no tungsten absorber in front of it.

Figure 6.2 gives the detector response after the optimized calibration procedure for electrons that has been introduced in Section 5.4 with different energies. The measured distributions were fit with a Gaussian fit (black line). The mean of the fit $\langle N_R^c \rangle$ will be used to calculate the linearity, and the energy resolution is obtained from the sigma of the fit.

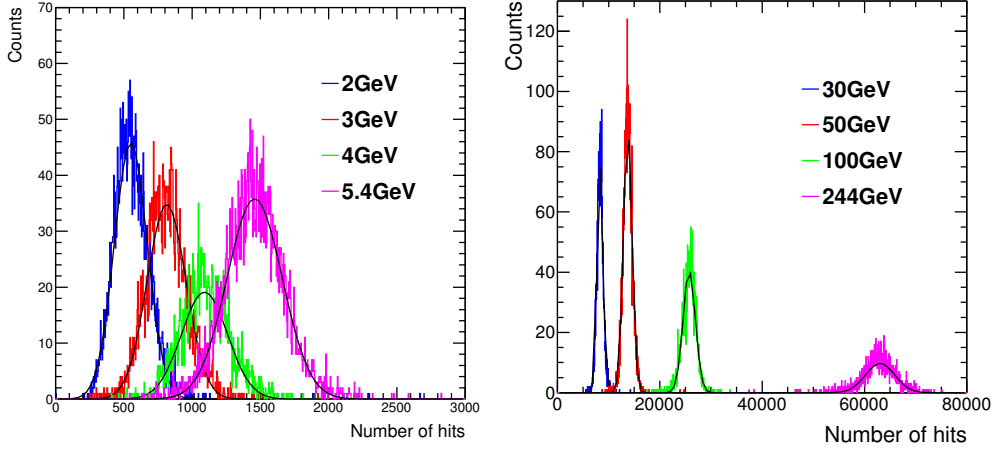


Figure. 6.2: Detector response after calibration for DESY (left) and SPS (right) electron beam data sets

6.4 Linearity and Energy Resolution

Table 6.1: Parameters for the fit by using equation $\langle N_R^c \rangle = k \cdot E$.

Scenario	k (GeV^{-1})
Data	266.9 ± 0.01
MC (real detector)	262.6 ± 0.2
MC (ideal detector)	258.2 ± 0.01

Table 6.2: Parameters for the fit by using equation $\langle N_R^c \rangle = \alpha \cdot E^\beta$.

Scenario	α (GeV^{-1})	β
Data	292.2 ± 0.6	0.980 ± 0.0004
MC (real detector)	277.0 ± 0.8	0.988 ± 0.0006
MC (ideal detector)	278.7 ± 0.7	0.986 ± 0.0005

Figure 6.3 shows the mean energy response of the prototype after the calibration optimization described in Section 5.4. The figure also compared to

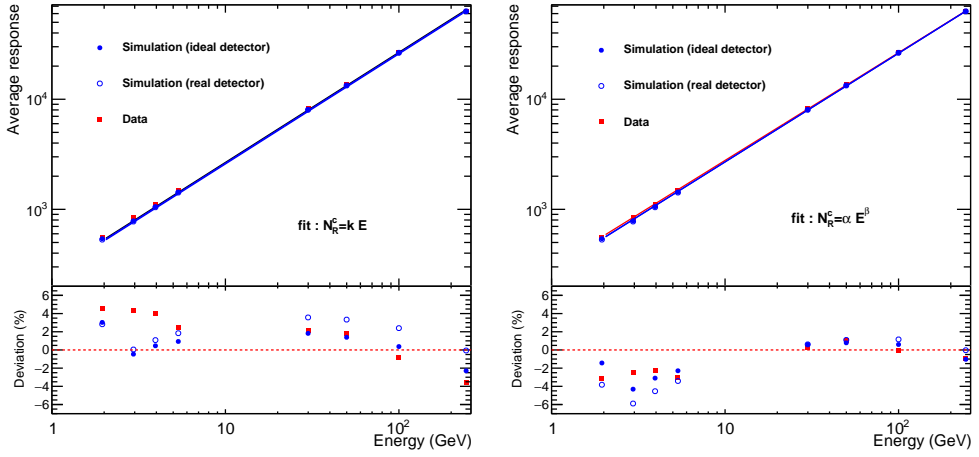


Figure. 6.3: Mean response as a function of momentum. Shown are test beam data and results of MC simulation for two different assumptions on the detector properties (see text). The data are fitted with linear function (left) and non-linear function (right). At the bottom, the ratio of the mean values to the fit function (see text) is shown.

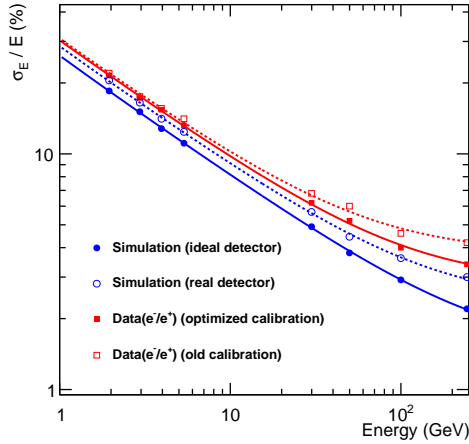


Figure. 6.4: Energy resolution as a function of momentum. Included are test beam data for the two sets of calibration factors and MC simulations, again for the two different scenarios. The lines show fits with Equation 6.1.

simulation results with an ideal detector as well as the “real detector” where the malfunctioning sensors, channels and pixels are considered. The left panel shows a fit of a linear function $\langle N_R^c \rangle = k \cdot E$. To compare with the linear function, the fit result of a power law function $\langle N_R^c \rangle = \alpha \cdot E^\beta$ is shown in the right panel. Different fit scenarios are shown for comparison, and the lower part of that panels show the ratio of the mean values to the corresponding function fit. The fit parameters can be found in Table 6.1 and 6.2. For the linear function fit, both experimental data and simulation show deviations from the linear function of the order of a few percent. The data shows an increasing deviation to smaller than linear response to higher energies. This may be a hint that small effect of saturation appear and should be corrected for. The agreement between experiment and simulation is reasonably good, but also not perfect. This may in part be due to the fact that the sensitivity differences have still not been fully corrected in the experimental data, but are not present in simulation. Also, the relatively simple implementation of charge diffusion may influence the linearity. The comparison with the non-linear fit function in the right panel of Figure 6.3, shows a very good description of the behaviour for the SPS energies. For the DESY energies the fit function is consistently slightly too high. One should note that the DESY measurements were done with slightly different settings of the detector, and the discrepancy here might point to an uncertainty in the relative calibration of the two different measurement campaigns.

The energy resolution of the prototype is shown in Figure 6.4, also compared to simulation results with an ideal detector as well as the “real detector” where the malfunctioning sensors, channels and pixels are taken into account.

The energy dependence of the energy resolution can be characterized as

$$\frac{\sigma}{E} = A \oplus \frac{B}{\sqrt{E/\text{GeV}}} \oplus \frac{C}{E/\text{GeV}} \quad (6.1)$$

where the three terms are the “constant” term, “stochastic” term, and “noise term”, respectively. The fit parameters from “old” calibration which has been discussed in [34], and the parameters obtained after calibration optimization described in Section 5.4.3 are shown in Table 6.3.

Table 6.3: Parameters for energy resolution fit by using Equation 6.1.

Calibration	A(%)	B(%)	C(%)
old	3.78 ± 1.60	30.02 ± 3.98	6.3
optimized	2.95 ± 1.65	28.47 ± 3.83	6.3

The values of the energy resolution for experimental and simulated data for different energies with the optimised calibration, are listed in Table 6.4.

Table 6.4: Energy resolution of experimental data, simulated “ideal detector”, and “real detector” at all energies.

Momentum (GeV/c)	Data		MC (real detector)		MC (ideal detector)	
	Sigma/Mean	$\sigma_E/E(\%)$	Sigma/Mean	$\sigma_E/E(\%)$	Sigma/Mean	$\sigma_E/E(\%)$
2	120/558	21.5	112/542	20.7	100/540	18.5
3	145/835	17.3	133/788	16.9	118/796	14.8
4	171/1110	15.4	152/1060	14.3	135/1072	12.6
5.4	196/1476	13.3	177/1445	12.2	157/1452	10.8
30	508/8207	6.2	458/8143	5.62	400/8142	4.9
50	712/13890	5.4	619/13540	4.57	513/13520	3.8
100	1100/26400	4.0	990/26840	3.68	782/26730	2.9
244	2155/62727	3.4	1897/63804	2.97	1406/63459	2.2

The parameters obtained from the optimized calibration are similar to the ones from the old calibration, but the resolution is slightly improved for all energies, which makes both the stochastic and the constant term go down. The discrepancies between the “real detector” simulation and experimental data are not fully understood, but the following factors could play a role:

- The sensitivities of the sensors are not perfectly equalised.
- The energy spread of beam particles is not implemented in the simulation.

6.5 e/π Separation

In this section we will discuss results on electron/pion separation based on the simulations that were introduced in Section 5.3.4. The energy spectrum of charged pions are followed with Equation 5.6. 100000 charged pion events were generated in the simulation. The positions of primary pions are uniformly distributed over the detector. After rejecting the events with incident position at $|x_c| > 1.5$ cm, $|y_c| > 1.5$ cm, 55873 pion events are left for the separation.

Figure 6.5 shows the distributions of observed energy for pions before and after applying different separation cuts. These cut values have been determined in Section 5.3.4. For the “observed energy” the number of hits is converted into

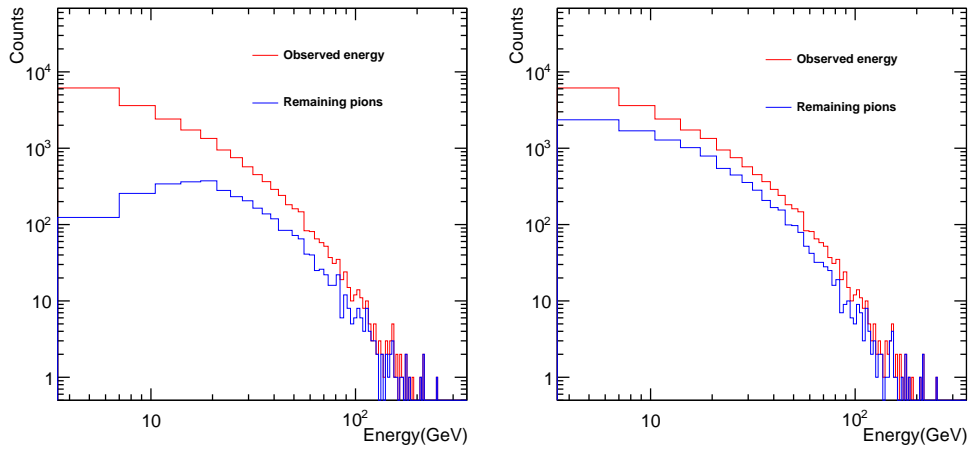


Figure. 6.5: e/π separation power by applying individual cut on the simulated data. The distribution of observed energy of pions without cuts is shown as the red line, and pions after final rejection are shown as the blue line. Left: cut on interaction layer. Right: cut on the lateral profile fit parameter α .

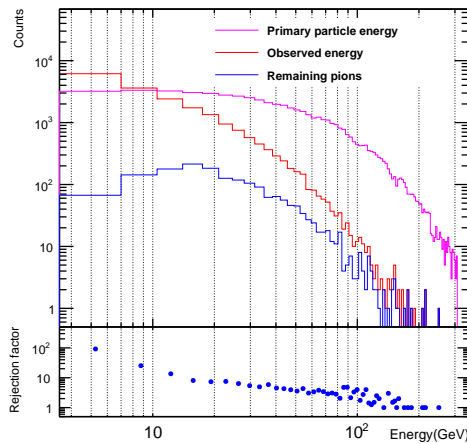


Figure. 6.6: e/π separation power. Primary pions are shown with the magenta line, red line represents the observed pion energy, and pions after final rejection are shown by the blue line. The ratio in the lower panel shows the pion rejection factor as a function of observed energy (see text).

an equivalent energy – here the conversion factor $1/k$ (see Section 6.4) from the linear fit to the electron response is used. The noise has been subtracted. In the left panel, only the interaction layer cut is used. The pion rejection in the low observed energy region (e.g. $E_{pion}^{obs} \leq 20$ GeV) is by a factor of 4 or more, since most of the pions produce either tracks or showers which start interacting at later layers of the detector. When the energy increases, the relative separation power decreases significantly, which is the consequence of the fact that pions start to shower in the early layers and deposit larger fraction of their energy. The separation power of using only the cut on the lateral exponential slope a is shown in the right panel of Figure 6.5, this cut also provides a significant separation power in a wide energy range. For lower energy (e.g. $E_{pion}^{obs} \leq 20$ GeV), this method is not as effective as the separation power with interaction layer cut. However, for higher energy, the separation power is similar for these two cuts. Because the properties exploited by these two cut parameters are different, the final separation power can be obtained by using the combination of them.

Figure 6.6 shows the separation power of using a simultaneous cut on both parameters. For comparison, the magenta histogram shows also the distribution of generated energies according to Equation 5.6. The red histogram is the the distribution of the observed energy in the detector without any additional cut. The clear difference between these two histogram is due to the on average small value of deposited energy and its large event-to-event fluctuations of hadronic showers. The blue histogram shows the remaining pions after applying the cuts. The pion rejection factor, i.e. the ratio of the distribution of observed energy before the cuts to the one after the cuts, is shown in the lower panel of Figure 6.6. A rejection by more than a factor of 8 is seen for energies below 20 GeV. At higher energy ($E_{pion}^{obs} \geq 20$ GeV), the pions start to produce shower in the early layers and more hits in the detector. The rejection factor decreases since the fraction of “electron-like” showers starts to increase. For the high energy pions, the pion rejection factor is still above 2.5 up to $E_{pion}^{obs} = 100$ GeV.

As can be seen from Figure 6.5 and 6.6, the discrimination using the shower start point is more efficient than the one using the lateral slope, but the combination of the two leads to significant further improvement. E.g. at an observed energy of ≈ 20 GeV, the number of observed pions without cuts is ≈ 1350 . The starting point cut reduces this to ≈ 350 , while the lateral slope cut by itself leads to ≈ 800 pions. The combination of the two achieves a reduction to ≈ 200 .

6.6 Shower Position Resolution

The position resolution of the shower reconstruction is studied by comparing the shower position x_c using the method described in Section 3.6 to the position x_0 of the cluster in the layer 0.

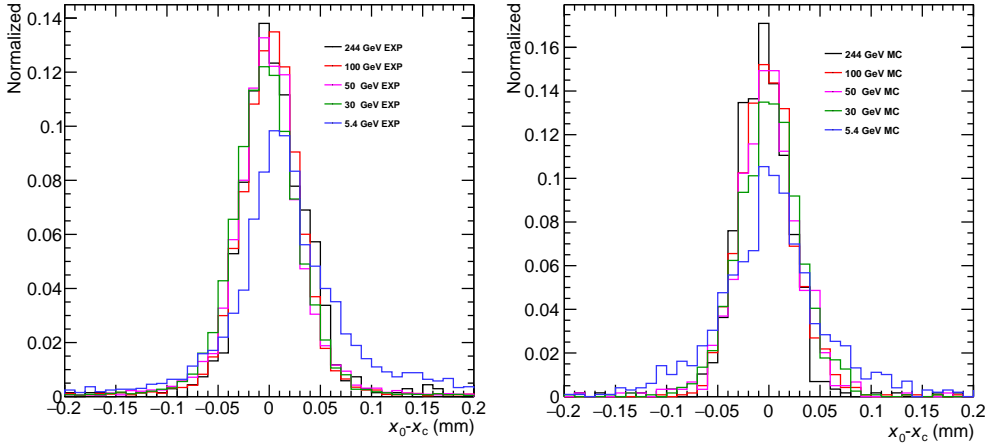


Figure. 6.7: Distributions of the cluster position x_0 with respect to the the shower position x_c in layer 0 for experimental (left) and simulated data (right).

The distribution of $x_0 - x_c$ for both experimental data and simulation are shown in Figure 6.7 for several beam energies, ranging from 5.4 GeV to 244 GeV. The distributions are approximately Gaussian and centred around zero for most beam energies. A deviation is visible for the 5.4 GeV data from DESY beam test data. The centre of the distribution slightly shifts to the right (0.01 mm), which is possibly due to the small inclination of the beam towards to the detector in the DESY experiments. This effect is not present in the simulation as the trajectories of the incident electrons are parallel to the z axis.

The position resolution is defined by the σ of the Gaussian fit of the $x_0 - x_c$ distribution¹ in Figure 6.7.

The obtained position resolution is represented in Figure 6.8 in the right panel as a function of beam energy E . The energy dependence can be described by

¹Here the focus is put only on the x coordinate since the y coordinate behaves similarly.

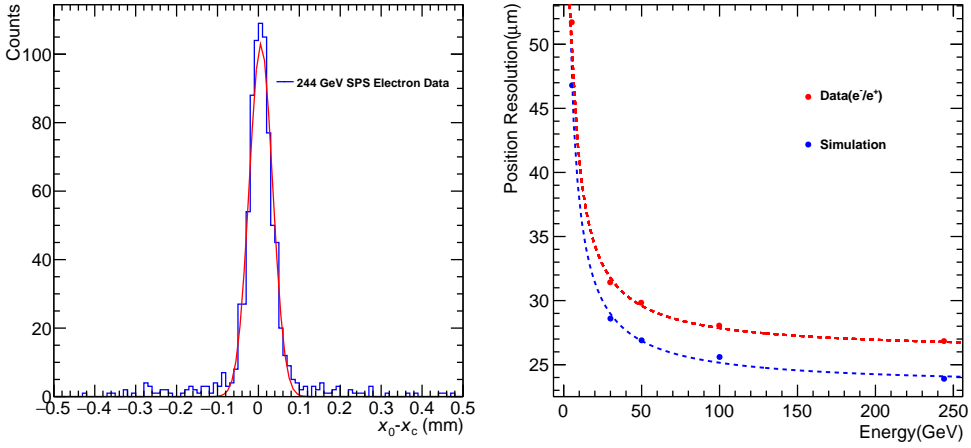


Figure. 6.8: Left: Distribution of $(x_0 - x_c)$ for 244 GeV electron data together with a Gaussian fit. Right: Resolution σ as a function of E for experimental and simulated data.

$$\sigma_x = f \oplus \frac{g}{\sqrt{E/\text{GeV}}} \quad (6.2)$$

Table 6.5: Parameter value of position resolution fitting

Data source	g (μm)	f (μm)
experimental	103.76 ± 1.16	25.80 ± 0.25
simulation	94.11 ± 1.05	23.33 ± 0.22

The parameters f and g obtained from a fit to the observed position resolutions are shown in Table 6.5. The position resolution of the FoCal prototype is extremely good. It is below 100 μm in a wide range of energies. For high energies (e.g. above 30 GeV), the position resolution is better than 30 μm . The position resolution in the simulation is slightly better than the experimental results since the limited precision of the alignment in the experimental data slightly degrades the resolution.



Chapter 7

Quarkonia Measurements with FoCal

7.1 Introduction

The physics motivation for the study of quarkonia has been introduced in Chapter 1. The FoCal, as a high granularity forward calorimeter system, can in principle also perform measurements of quarkonia in high energy collisions. The evaluation of the detector performance for quarkonia will be performed in simulation. By studying the simulation data, we will answer the following questions:

1. Can FoCal measure quarkonia in the dielectron channel?
2. Which quarkonia states can be observed and precisely measured?
3. What is the expect significance of the individually observed quarkonia states?
4. Can we make improvements of the detector to obtain better performance?

Similar studies have been conducted for the muon arm of ALICE [42,43], as well as for the heavy-ion programs of other experiments at LHC. As a comparison and extension, FoCal has the potential ability to measure the quarkonia in the di-electron decay channel. Since the aim of the simulations is to give a realistic estimate of the feasibility of these measurements and to indicate the possible direction for improvements, the quarkonia signals shall be embedded into realistic heavy-ion collision events (Pb-Pb) to validate the significance.

7.2 Simulation Situation

7.2.1 Detector construction

The current detector implementation of FoCal used in the simulation has already been introduced in Section 1.6. Here some more details of the detector design relevant for the photon/electron reconstruction are discussed.

The FoCal detector consists of two types of layer. The low-granularity layers (or “coarse layers”) have a cell size of approximately 1 cm^2 . These coarse layers are combined into segments for readout. The high-granularity layers (or “fine layers”) have a cell size of approximately 1 mm^2 and can be read out separately. The setup can be found in Figure 7.1. The area that FoCal covers is $1.6 \times 1.6 \text{ m}^2$. The thickness of the tungsten absorber is chosen to be approximately one radiation length (3.5 mm). The FoCal implemented in the simulations has an approximately circular hole of 8 cm radius around the beam pipe, and covers a radial distance up to $r = 0.8 \text{ m}$. The detector (first layer) is placed 7 m away from the interaction point.

The restriction of position resolution of the low-granularity layers makes it hard to recognize two clusters which are close to each other. This disadvantage can be solved by using the high-granularity layers. On the other hand, the low granularity layers have a better energy resolution as they are less sensitive to shower fluctuations due to their pixel size, which allows accurate energy measurement.

7.2.2 Clustering and shower reconstruction

In order to deal with the high occupancy in AA system. A dedicate method [5] of finding the clusters in the detector was developed. The same algorithm is also used for the low granularity layers. The algorithm parameters may be tuned for optimum performance depending on the granularity and occupancy.

The algorithm of finding cluster can be described as follows:

- Search for seeds which above the threshold (SeedThreshold) based on an energy-sorted list of digits from the segment.
- Digits within cluster radius (MaxRing $\approx 1.2 \text{ cm}$) of a higher energy seed are included in cluster.
- The seeds are not allowed to be less than MaxRing.

After the clusters have been found on each of the segments, it is necessary to determine which clusters on each segment belong to the same shower, and

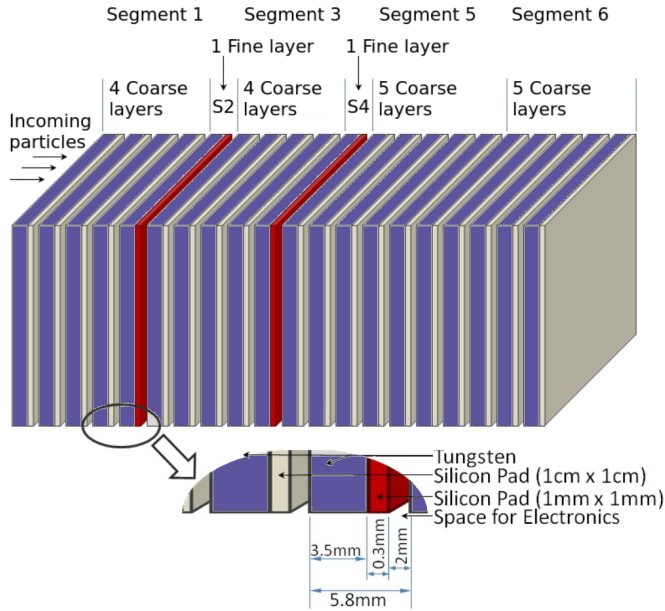


Figure. 7.1: The FoCal setup that was used in the simulation, which is another view of the same detector layout mentioned in Section 1.6.

to combine those clusters to determine the total energy of the shower and its position. An iterative algorithm [5] is used to combine information from different segments. This algorithm first loops over LGL and then HGL segments separately and finally combines LGL and HGL to find the final clusters. If more than one cluster is found on a HGL segment within a single cluster on a LGL segment, the LGL segment cluster is split into the corresponding number of HGL clusters, with energy partitioned according to the relative energies of the clusters found on the HGL segment. The total shower energy is obtained as the sum of all longitudinal segments of the matched clusters. The final shower position is calculated as the average of the two HGL segment positions.

7.3 Expected Quarkonia Yield

In the following, we will first estimate the expected production rates and the annual quarkonia production yields for FoCal. The properties of the quarkonium states investigated here are listed in Table 7.1.

Table 7.1: Mass, width and branching ratio of the di-electron channel of quarkonia states

system	mass(GeV/ c^2)	width(keV/ c^2)	Br(e^+e^-)(%)
$J/\psi(c\bar{c})$	3.096	93.4	5.94
Υ	9.460	54.02	2.38
Υ'	10.02	31.98	1.91

7.3.1 Quarkonia production

There are two necessary steps to form quarkonia, one is the production of a heavy quark pair in a hard collision and the other is the formation of quarkonia from two heavy quarks. Due to the high mass of the heavy quarks ($m_{charm} = 1.3 \text{ GeV}/c^2$, $m_{bottom} = 4.7 \text{ GeV}/c^2$), the production of heavy quarks can only take place during the early stage/initial hard scattering of the collision. The total charm production cross section is predicted to be 6.3 mb and the bottom production cross section is 0.19 mb.

The next step is the formation of quarkonia from the quark-anti-quark pair. There are several models describe the formation process, namely the Color Evaporation Model (CEM) [44], Heavy Quark Effective Model [45], Color Octet Model (COM) [46] and the Color Singlet Model (CSM) [47].

The cross section at forward rapidity has been measured by using the muon arm of the ALICE experiment in proton-proton collisions with a centre-of-mass energy of $\sqrt{s} = 7 \text{ TeV}$ and $\sqrt{s} = 8 \text{ TeV}$ [48, 49]. Here the cross section measured at these energy can be used to estimate the yield in 5.5 TeV Pb-Pb collisions. The resulting total cross section and the cross section in different p_T intervals are listed in Table 7.2 and 7.3. These numbers will be used in the analysis in the following sections.

Table 7.2: Cross section for quarkonia measured by the muon arm of ALICE. The branching ratio has been taken into account.

system	energy(\sqrt{s})	$J/\psi(\mu\text{b})$	$\Upsilon(\mu\text{b})$
p-p	7 TeV	4.37	0.0361

Table 7.3: Cross section of quarkonia states in different p_T intervals. The branching ratio has been taken into account.

p_T (GeV/c)	J/ψ (μb)	Υ (μb)
[0; 2]	2.071	0.0029
[2; 4]	1.683	0.0063
[4; 6]	0.511	0.0043
[6; 8]	0.0689	0.0023
[8; 10]	0.0199	0.0011
[10; 12]	0.007	—
[12; 14]	0.0029	—

7.3.2 Branching ratio

Since quarkonia that decay in the dielectron channel can be measured by FoCal, the branching ratios in dielectron channel of quarkonia states are shown in Table 7.1. Table 7.2 lists the cross section times the branching fraction for the di-electron channel.

7.3.3 Glauber model scaling

Quarkonia production in lead-lead collisions can be calculated as a superposition of nucleon-nucleon collisions. There is a widely used approach to calculate the number of elementary collisions, the Glauber model. For our calculation a rough estimate is sufficient. We will use the number of collisions in minimum-bias Pb-Pb reactions approximately to be $N_{coll} \approx 400$.

7.3.4 Quarkonia yields

Based on the calculations mentioned above, the final yields of quarkonia can be obtained from the following equation

$$Y_{q\bar{q}} = \frac{\sigma_{q\bar{q}pp}}{\sigma_{inelastic}} \times N_{coll} \times Br_{e^+e^-}. \quad (7.1)$$

Here, $\sigma_{q\bar{q}pp}$ is the production cross section of quarkonia in proton-proton collision system in Table 7.3. $\sigma_{inelastic} = 55.6$ mb is the total inelastic cross section to calculate the production yield per inelastic event. N_{coll} is the approximate

scaling number obtained from Glauber model. The resulting quarkonium yield in different p_T intervals for minimum bias 5.5 TeV Pb-Pb collisions is shown in Table 7.4.

Table 7.4: Expected yield J/ψ and Υ events in different p_T range .

p_T (GeV/c)	Yield (per event)	
	J/ψ	Υ
[0; 2]	2.68×10^{-2}	3.76×10^{-5}
[2; 4]	2.18×10^{-2}	8.16×10^{-5}
[4; 6]	6.62×10^{-3}	5.57×10^{-5}
[6; 8]	8.92×10^{-4}	2.98×10^{-5}
[8; 10]	2.59×10^{-4}	1.42×10^{-5}
[10; 12]	9.35×10^{-5}	—
[12; 14]	3.59×10^{-5}	—

7.4 Background Estimate

To estimate the final significance of the quarkonium signal, it is necessary to generate a realistic background and to combine it with signals. In this thesis, HIJING is used as the model to simulate the lead-lead background spectrum. In order to identify the realistic quarkonia mass interval, a quarkonia event was embedded in a lead-lead collision event. The clusters which are within 0.5 mm of the extrapolate clusters positions from quarkonia signal event were treated as the candidate quarkonia clusters. The reconstructed invariant mass spectrum of quarkonia states are show in Figure 7.2.

Since the quarkonia yield is small for every central lead-lead event (see Table 7.4), the background which is introduced by the clusters from quarkonium events in every collision event is negligible. The background can be estimated by using the Hijing invariant mass spectrum measured by FoCal in the simulation simply without embedding quarkonia signal. The background is calculated as integral over a fixed mass interval without embedding quarkonia event corresponding to $\pm 2\sigma$ of a Gaussian fit to the reconstructed mass distribution of the quarkonium states in Figure 7.2. The fit range can be found in Table 7.5. The number of background candidates in different p_T intervals are shown in Table 7.6.

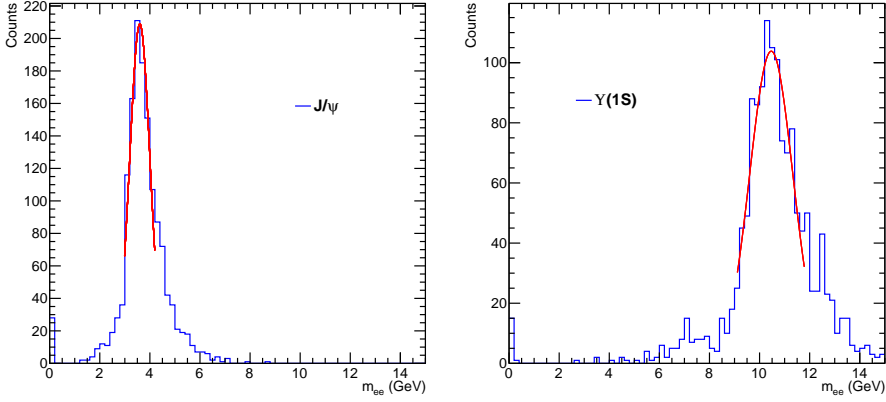


Figure. 7.2: Invariant mass of reconstructed J/ψ and Υ events embedded in the HIJING Pb-Pb events. The fit ranges are used as mass window for background estimation.

Table 7.5: Mass resolution and the Gaussian fit range of the invariant mass spectrum for J/ψ and $\Upsilon(1S)$ in the simulation.

quarkonia	FWHM (GeV/ c^2)	$\Delta E/E$ (%)	m_{low}	m_{up}
J/ψ	1.0	32.2	2.61	4.89
Υ	1.6	15.2	8	12.64

Table 7.6: Number of background candidates in different p_T intervals from HIJING model.

p_T (GeV/ c)	Background (per event)	
	J/ψ	Υ
[0; 2]	8.820×10^4	11.80
[2; 4]	5.348×10^4	17.61
[4; 6]	6.608×10^3	10.17
[6; 8]	3.630×10^2	3.77
[8; 10]	27.056	1.80
[10; 12]	8.988	0.50
[12; 14]	0.6	—

7.5 Quarkonia Performance

For this estimate, we use the expected interaction rate of 50 kHz for Pb-Pb events, which is expected to be available in run 3 of the LHC. The total Pb-Pb collision events that was used in the quarkonia estimation at run 3 is 2×10^{10} .

Now that all the physics variables to estimate the quarkonia measurements with FoCal have been described, the aim of this section is to give a realistic answer to the question whether the quarkonia can be measured by standalone FoCal through the di-electron channel. The performance of the measurements can be characterised by three quantities, namely the amount of expected signal, the signal to background ratio (S/B), and the significance (SIG). The amount of expected signal can be easily calculated by multiply the interaction rate and the yield per event, while the rest two quantities are defined as

$$S/B = \frac{\Sigma N_{sig}}{\Sigma N_{bkg}} \quad (7.2)$$

$$SIG = \frac{\Sigma N_{sig}}{\sqrt{\Sigma N_{sig} + \Sigma N_{bkg}}} \quad (7.3)$$

The significance depends on the total amount of interaction events and the signal events, while the signal to background ratio is independent of the statistics. Compared with the statistics of background in different p_T intervals, the signal can be straightforwardly treated as negligible in most of the cases.

Table 7.7: Signal to background ratio and significance of J/ψ and Υ for different p_T intervals.

p_T (GeV/c)	J/ψ		Υ	
	S/B	SIG	S/B	SIG
[0; 2]	3.03×10^{-7}	12.76	4.26×10^{-10}	1.54
[2; 4]	4.07×10^{-7}	13.33	1.53×10^{-9}	2.75
[4; 6]	1.00×10^{-6}	11.52	8.43×10^{-9}	2.47
[6; 8]	2.46×10^{-6}	6.62	8.20×10^{-9}	2.17
[8; 10]	9.57×10^{-6}	7.04	3.91×10^{-8}	1.50
[10; 12]	1.04×10^{-5}	4.41	—	—
[12; 14]	5.98×10^{-5}	6.55	—	—

The obtained results for the signal to background ratio and the signal significance for J/ψ by standalone FoCal can be found in Table 7.7. For the J/ψ measurement, the significance in individual p_T bins is not sufficient due to the following reasons

- The relatively low yield of quarkonia in the forward region, which significantly reduces the signal to background ratio.
- The background dominated by photons from the π^0 decay plays a role in the background spectrum.
- The mass resolution is low which increases the amount of background under the peak and this leads to the bad signal to background ratio.

The reasons mentioned above lead to difficulties to perform the measurements with standalone FoCal detector. Improvements are necessary to increase the signal to background ratio and significance. The dominant background introduced by photons from π^0 decay can be improved by tagging the particles, e.g. a charged particle detector. The mass resolution can be improved by taking into account the curvature in the magnetic field, although it may be a small effect.



Chapter 8

Conclusion and Outlook

8.1 Conclusion and discussion

It is well known that the parton distributions are crucial for understanding the particle production in heavy-ion collisions. The increase of the density of partons (especially for gluons) at high Q^2 and small Bjorken- x should lead to non-linear effects and this in turn would lead to gluon saturation. Several phenomena have been predicted and studied in recent years, but the understanding is still limited. Direct photon production is considered to be a clean probe for gluon saturation, and the increase of the energy at LHC also makes very small values of x accessible. However, the dominant background of neutral pions, which decay to two photons, poses a challenge for the identification of direct photons. The proposed forward calorimeter (FoCal), which is a high granularity calorimeter, is intended to measure direct photons in the forward region in the ALICE experiment at CERN. It enables to probe the gluon density at very small x . The robust separation power between direct and decay photons of FoCal requires high granularity since the opening angle between the two decay photons from neutral pions are small for forward emission.

The possibility of quarkonium measurements with the FoCal detector was studied in the simulation. The low yield of quarkonium production in the forward region and also the background introduced by photons from π^0 decay, which lead to a low signal to background ratio, will likely not allow us to perform such measurements. The simulation result and also some possible ways to improve the quarkonium measurements result were summarised in Section 7.5.

In order to perform the studies are motivated by FoCal by using the state-of-the-art technologies, a prototype with 96 MAPS CMOS sensors (pitch size $30 \times 30 \mu\text{m}^2$) and tungsten absorber has been build. It allows to reconstruct

particles in full digital mode. The detector has achieved a very small Molière radius (11 mm). 3 types of sensor with different thickness of epitaxial layers were installed in the detector. The prototype consists of 24 layers, and the total depth for electromagnetic showers is $28 X_0$. Each layer contains 4 MIMOSA sensors. The active area is $4 \times 4 \text{ cm}^2$, which is wide enough to contain an electromagnetic shower and to study the lateral shower development.

The prototype has been successfully tested with both cosmic muons and particle beams. The MIP tracking algorithm based on the straight line model was developed and tested. Several important analyses have been done based on the reconstructed tracks.

- Alignment is necessary since the position uncertainties after detector assembly can be up to hundreds of microns. In total 283 degrees of freedom were determined in the alignment procedure. By iterating the minimizing procedures of alignment, the residuals between the track fitting position and the observed hit position can be reduced to less than $5 \mu\text{m}$.
- Efficiencies of the sensors in the detector were measured with both pion and muon tracks. The results are shown in Figure 6.1. The high energy pion tracks give relatively consistent efficiencies for the sensors with the same kind of epitaxial layer.

Data from beam tests at DESY (using electrons) and CERN (electrons and pions) were also analysed for showering particles.

- A unique method for reconstructing the shower centre was developed and studied. This method is different from the conventional way with energy deposition in the transverse segments, it uses the digital information from all the layers together with power law weight to enhance the significance of the shower core region. By optimizing the parameters in Equation 5.2, the position resolution of the shower position can be better than $30 \mu\text{m}$ for high energy electrons (see Figure 6.7).
- The pion contamination in the test beam data has been estimated, which can be neglected in the analysis. For the general purpose, the differences of behaviour between electrons and pions were compared by using both longitudinal and transverse information of the shower in the simulation. The interaction point of shower can be identified with the method demonstrated in Section 5.3. The estimation of separation power is obtained based on setting combination cuts on both the longitudinal and transverse parameters extracted from showers for different energies in Figure 6.6. A very significant additional suppression of pions can be achieved.

- The event selection criteria for the calibration were optimized. After applying the new calibration factors we obtained in Figure 5.21, the energy resolution was improved for all energies.

8.2 Outlook

Prototype

The malfunctioning sensors, channels and pixels account for almost 30% of the total number of pixels in the detector, which makes the data cleaning, processing, and analysing relatively difficult. The systematic uncertainties of extrapolating the data in the dead region are significant and hard to estimate due to event by event fluctuations of the electromagnetic showers. There are other instrumental effects, e.g. gap and overlap regions, which influence the number of visible hits in the analysis. This may further reduce the effective usable region of the detector. For example, in the efficiency calculation, the gap and overlap regions have to be excluded. For the shower centre reconstruction, the precision of the shower centre determination in these regions decreases since part of the data is lost or doubled, which may bias the results. All these effects could be improved with a new prototype.

Simulation

Although the muons are not the most important particles for a calorimeter, it still plays a role for evaluating and testing the calorimeter in many intermediate aspects, e.g. alignment, calibration, and investigating the characteristics of the sensor. Therefore, an accurate cosmic ray generator is necessary in the simulation.

The physics lists for hadronic models in Geant4 are still under development, which could be the reason that discrepancies still exist between the simulation and experimental data. The physics list for electromagnetic processes is considered to be well described in Geant4. However, several differences in the shower shape analysis, especially in the longitudinal shower profile have been found. A physics list with FTFP_BERT_EMY option, which is proposed by the CALICE collaboration, shows good agreement for the shower maximum region of electrons in the digital hadronic calorimeter. The simulation based on the new physics list is worth to compare with the emStandard physics list in the future.

Experiments

There is still room to tune the sensitivities of some of the sensors in the prototype. After recovering some of the layers (e.g. layer 21), the threshold of these sensors also need to be optimized. Some of the sensors are located in the critical layers of shower development but have an unsatisfying tuning of the threshold. For example, the sensor located at $(l,q)=(10,0)$ contributes a large bias to the energy resolution. It may be worth to tune its threshold to improve the sensitivity.

The efficiencies for different energies in Figure 6.1 indicate that the type of sensor may play a role in the efficiency of sensors. The sensitivities are different for other thickness of epitaxial layer sensors, which makes the tuning of the sensor complicated and unstable.

The hadronic shower development in the highly granular electromagnetic calorimeter is interesting since it can be used for the Particle Flow Algorithm (PFA) for full imaging the particles in future calorimeter technologies. To develop realistic *Particle Flow Algorithms* (PFA), the interactions of hadrons and the detector response must be modelled and well understood in Monte Carlo simulations, and these should be compared with the experimental data.

The electron hadron separation has been studied. Although we compared the separation power from simulation to experimental data, due to the deficiency of the particle identification detector during SPS beam test, the verification of the method is limited.

All these problems can probably be solved by performing further test beams or building a new high granularity calorimeter prototype.

References

- [1] C. Rubbia, in Proceeding of the XXVI International Conference on High Energy Physics No. **272**, Vol. I, p. 321.
- [2] H. Satz, Nucl. Phys. A **544** (1992) 371c.
- [3] J.D. Bjorken, Phys. Rev. D **27** (1983) 140.
- [4] T.D. Lee, Nucl. Phys. A, **538** (1992) 3c.
- [5] The ALICE FoCal Collaboration, *Letter of Intent, A Forward Calorimeter (FoCal) for the ALICE experiment*.
- [6] V. N. Gribov and L.N. Lipatov, Sov. J. Nucl. Phys. **15** (1972) 438.
- [7] T. Peitzmann, *Measurement of forward direct photon production in pA at the LHC with ALICE A probe for nuclear PDFs and saturation*, Proceeding of Science. **PoS** (DIS2016) 273.
- [8] A.D. Frawley, *Cold Nuclear Matter Effects and Heavy Quark Production in PHENIX*, Proceedings for talk at Hard Probes 2012. arXiv:1209.1159
- [9] P. Hansson, *The parton model*, KTH, November 18. 2004.
- [10] G. A Rinella, *The ALPIDE pixel sensor chip for the upgrade of the ALICE Inner Tracking System*, Nucl. Inst. and Meth. **845** (2017) 583.
- [11] L. McLerran and R. Venugopalan, Phys. Rev. D. **49** (1994) 2233.
- [12] L. McLerran and R. Venugopalan, Phys. Rev. D. **49** (1994) 3352.
- [13] L. McLerran and R. Venugopalan, Phys. Rev. D. **50** (1994) 2225.
- [14] T. Peitzmann, *Prototype studies for a forward EM calorimeter in ALICE*, Proceedings of CHEF 2013 - Calorimetry for the High Energy Frontier, arXiv:1308.2585v1

- [15] The ALICE Collaboration, *Technical Design Report of the Zero Degree Calorimeters (ZDC)*, (1999).
- [16] ALICE Collaboration, *Technical Design Report on Forward Detectors: FMD, T0 and V0*, (2004).
- [17] ALICE Collaboration, *Technical Design Report of the Inner Tracking System (ITS)*, (1999).
- [18] ALICE Collaboration, *Technical Design Report of the Time Projection Chamber (TPC)*, (2000).
- [19] A. Brogna *et al.*, *Manual PHASE1*, IPHC Strasbourg.
- [20] C.W. Fabjan *et al.*, *Calorimetry for Particle Physics* Rev. Mod. Phys. **75** (2003) 1243
- [21] C.W. Fabjan., *Techniques and Concepts of High Energy Physics III*, (1985) 281.
- [22] P.N. Dinh *et al.*, *Measurement of the Zenith Angle Distribution of the Cosmic Muon Flux in Hanoi*, Nucl. Phys. B. **661** (2003) 3.
- [23] G.A. Akopjanov *et al.*, *Determination of photon coordinates in a hodoscope cherenkov spectrometer*, Nucl. Inst. and Meth. **140** (1977) 441.
- [24] V.A. Davydov *et al.*, Nucl. Inst. and Meth. **145** (1977) 267.
- [25] L. Bugge, Nucl. *On the determination of shower central positions from lateral samplings*, Inst. and Meth. **242** (1986) 228.
- [26] J.J. Gomez, *Study of an algorithm for electron-hadron separation in modular homogeneous calorimeters*, Nucl. Inst. and Meth. **262** (1987) 284.
- [27] P.J. Blenkers, *The Development of a GEANT Based Monte Carlo Simulation Framework for the R&D Process of the FoCal Calorimeter*, Master thesis Utrecht University (2012).
- [28] T.C. Awes *et al.*, Nucl. Inst. and Meth. **311** (1992) 130.
- [29] Y.S. Tsai, Rev. Mod. Phys. **46** (1974) 815. Prentice-Hall, Inc., Englewood Cliffs, NJ, 1952.
- [30] R. Wigmans, *Calorimetry - Energy Measurement in Particle Physics*, Oxford Science Publications, (2000).
- [31] E. Longo and I. Sestili, Nucl. Inst. Meth. **128** (1975) 283.

- [32] D. Fehlker, *et al.*, *Electronics for a Highly Segmented Electromagnetic Calorimeter Prototype*, 2013 JINST 8 P03015.
- [33] M.Reicher, *Digital Calorimetry using Pixel Sensors*, PhD thesis Utrecht University (2016).
https://www.nikhef.nl/pub/services/biblio/theses_pdf/thesis_M_Reicher.pdf
- [34] C.Zhang, *Measurements with a High Granularity Digital Electromagnetic Calorimeter*, PhD thesis Utrecht University (2017).
https://www.nikhef.nl/pub/services/biblio/theses_pdf/thesis_C_Zhang.pdf
- [35] A. Himmi, A. Brogna, *et al.*, *PHASE-I User Manual*, Institut de Recherches Subatomiques IN2P3-CNRS / ULP Strasbourg, France.
- [36] P.F. Dauncey, *Performance of CMOS Sensors for a Digital Electromagnetic Calorimeter*, **PoS (ICHEP 2010) 502**.
- [37] A.P. de Haas, G. Nooren, T. Peitzmann, M. Reicher, E. Rocco, D. Rohrich, K. Ullaland, A. van den Brink, M. van Leeuwen, H. Wang, S. Yang, C. Zhang, *The FoCal prototype - an extremely fine-grained electromagnetic calorimeter using CMOS pixel sensors*, accepted for publication in JINST.
- [38] K.A.Olive *et al.*, *Particle Physics booklet*, 2014.
<http://pdg.lbl.gov/>.
- [39] Application Software Group, *Geant Detector Description and Simulation Tool*, CERN, Geneva (1993).
- [40] Geant4 Collaboration, *Geant4 User's Guide for Application Developers* Published 14 December, 2007.
- [41] L. Maczewski *et al.*, Nucl. Inst. Meth. **A610** (2009) 640.
- [42] G.Martinez, *Physics of Muon Spectrometer of the ALICE Experiment*, J. Phys. Conf. Ser. **50** (2006) 361.
- [43] G.Martinez, *ALICE Potential for Open Heavy Flavour Physics*, J. Phys. G: Nucl. Part. Phys., Proceedings Quark Matter 2006.
- [44] H. Fritzsch, *Producing Heavy Quark Flavors in Hadronic Collisions: a Test of Quantum Chromodynamics*, Phys. Lett. B, **67** (1977) 217.
- [45] T. Mannel, *Recent Progress in the Theory of Heavy Flavour Decays*, J. Phys. G **21** (1995) 1007.

- [46] E. Braaten *et al.*, *Color Octet Fragmentation and the Ψ' Surplus at the Tevatron*, Phys. Rev. Lett, **74** (1995) 3327.
- [47] E. L. Berger *et al.*, *Inelastic Photoproduction of J/ψ and Upsilon by Gluons*, Phys. Rev. D, **23** (1981) 1521.
- [48] The ALICE Collaboration, Abelev, B., Adam, J. et al. *Measurement of Quarkonium Production at Forward Rapidity in pp Collisions at $\sqrt{s} = 7$ TeV*, Eur. Phys. J. C **74** (2014) 2974.
- [49] The ALICE Collaboration, Abelev, B., Adam, J. et al. *Inclusive Quarkonium Production at Forward Rapidity in pp Collisions at $\sqrt{s} = 8$ TeV*, Eur. Phys. J. C **76** (2016) 184.

Appendix Appendix A

Table Appendix A.1: Sensors information in the prototype

L	Q	RN	LN	z (mm)	RL (X_0)	Simulation mialignment	
						x (μ m)	y (μ m)
0	0	0	0	2.05	0.03	-106.39	-293.406
	1	1	1	2.05		-106.39	-673.406
	2	2	2	1.90		349.784	-579.372
	3	3	3	1.90		349.784	-199.372
1	0	44	4	5.98	1.00	-21.1856	-36.492
	1	45	5	5.98		-21.1856	-416.492
	2	46	6	5.86		444.458	-578.861
	3	47	7	5.86		444.458	-198.861
2	0	48	8	9.96	1.98	-26.9814	-221.275
	1	49	9	9.96		-26.9814	-601.275
	2	50	10	9.79		468.127	-412.891
	3	51	11	9.79		468.127	-32.891
3	0	92	12	13.90	2.95	-140.161	1.199
	1	93	13	13.90		-140.161	-378.801
	2	94	14	13.77		356.28	-529.463
	3	95	15	13.77		356.28	-149.463
4	0	4	16	17.94	3.92	-369.799	-20.095
	1	5	17	17.94		-369.799	-400.095
	2	6	18	17.70		243.954	-298.952
	3	7	19	17.70		243.954	81.048
5	0	40	20	21.93	4.90	-106.45	-42.281
	1	41	21	21.93		-106.45	-422.281
	2	42	22	21.75		490.487	-350.688

	3	43	23	21.75		490.487	29.312
6	0	52	24	25.92	5.87	-212.518	100.419
	1	53	25	25.92		-212.518	-279.581
	2	54	26	25.74		324.41	-456.048
	3	55	27	25.74		324.41	-76.048
7	0	88	28	29.92	6.85	-251.557	-38.14
	1	89	29	29.92		-251.557	-418.14
	2	90	30	29.73		250.047	-396.42
	3	91	31	29.73		250.047	-16.42
8	0	8	32	33.87	7.82	-243.723	-172.376
	1	9	33	33.87		-243.723	-552.376
	2	10	34	33.73		550.765	-243.459
	3	11	35	33.73		550.765	136.541
9	0	36	36	37.85	8.80	-68.0094	84.951
	1	37	37	37.85		-68.0094	-295.049
	2	38	38	37.68		266.614	-466.782
	3	39	39	37.68		266.614	-86.782
10	0	56	40	41.86	9.77	-74.5208	62.613
	1	57	41	41.86		-74.5208	-317.387
	2	58	42	41.72		278.031	-235.742
	3	59	43	41.72		278.031	144.258
11	0	84	44	45.82	10.74	-211.975	358.99
	1	85	45	45.82		-211.975	-21.0096
	2	86	46	45.73		212.016	-251.561
	3	87	47	45.73		212.016	128.439
12	0	12	48	49.85	11.72	-266.765	165.405
	1	13	49	49.85		-266.765	-214.595
	2	14	50	49.69		276.506	-260.287
	3	15	51	49.69		276.506	119.713
13	0	32	52	53.88	12.69	-227.292	446.01
	1	33	53	53.88		-227.292	66.0103
	2	34	54	53.65		162.987	-207.445
	3	35	55	53.65		162.987	172.555
14	0	60	56	57.83	13.67	-434.54	55.498
	1	61	57	57.83		-434.54	-324.502
	2	62	58	57.69		165.595	-378.194
	3	63	59	57.69		165.595	1.806
15	0	80	60	61.81	14.64	-331.817	143.544
	1	81	61	61.81		-331.817	-236.456

	2	82	62	61.64		291.74	-206.465
	3	83	63	61.64		291.74	173.535
16	0	16	64	65.81	15.62	-408.111	152.645
	1	17	65	65.81		-408.111	-227.355
	2	18	66	65.62		269.492	-132.786
	3	19	67	65.62		269.492	247.214
17	0	28	68	69.78	16.59	-365.362	26.987
	1	29	69	69.78		-365.362	-353.013
	2	30	70	69.61		175.917	-452.257
	3	31	71	69.61		175.917	-72.257
18	0	64	72	73.73	17.56	-358.518	-196.832
	1	65	73	73.73		-358.518	-576.832
	2	66	74	73.65		240.785	-238.045
	3	67	75	73.65		240.785	141.955
19	0	76	76	77.79	18.54	-200	283.382
	1	77	77	77.79		-200	-96.618
	2	78	78	77.60		268.612	-96.618
	3	79	79	77.60		268.612	283.382
20	0	20	80	81.79	19.51	-511.954	-52.552
	1	21	81	81.79		-511.954	-432.552
	2	22	82	81.66		247.604	-317.86
	3	23	83	81.66		247.604	62.14
21	0	24	84	85.86	20.49	-50	364
	1	25	85	85.86		-50	-16
	2	26	86	85.71		-50	-16
	3	27	87	85.71		-50	364
22	0	68	88	109.98	27.17	-414.087	130.087
	1	69	89	109.98		-414.087	-249.913
	2	70	90	109.86		241.386	-146.745
	3	71	91	109.86		241.386	233.255
23	0	72	92	113.94	28.14	-381.302	213.609
	1	73	93	113.94		-381.302	-166.391
	2	74	94	113.91		222.168	-90.9015
	3	75	95	113.91		222.168	289.098

L: Layer number

Q: Quadrant

RN: Readout number

LN: Longitudinal Number

RL: Radiation length

Nederlandse Samenvatting

Introductie

De productie van deeltjes in een botsing tussen twee zware ionen, zoals die plaats vinden bij het ALICE experiment aan de LHC in Genève, is afhankelijk van de verdeling van partonen (quarks en gluonen) in de protonen en neutronen waaruit de ionen bestaan. De verwachting is dat de toename in de partondichtheid, met name die van gluonen met een klein longitudinaal impulsaandeel (Bjorken- x), bij een hoge impulsoverdracht Q^2 , zal leiden tot non-lineair gedrag met als gevolg gluonsaturatie. Deze verwachting wordt al enkele jaren onderzocht, maar er is nog weinig bekend of begrepen van dit verschijnsel.

Door de hoge botsingsenergieën van de LHC zijn daar zeer kleine waarden van x bereikbaar en kan gluonsaturatie tot in detail bestudeerd worden. Directe fotonen bieden een zeer schone methode om gluonsaturatie te meten. Directe fotonen moeten onderscheiden worden van fotonen die ontstaan in het verval van neutrale pionen, die voornamelijk in twee fotonen vervallen. Bij hoge energien van het pion bevinden deze fotonen zich zeer dicht bij elkaar en kunnen verwart worden met een enkel foton.

Een calorimeter in het voorwaardse deel van de ALICE detector, de FoCal, is ontworpen om directe fotonen te kunnen meten, en daarmee ook de gluonsaturatie bij hele kleine waarden van x . Onderscheid tussen directe en vervalsfotonen is mogelijk doordat de FoCal een hele hoge granulariteit bezit en daardoor twee fotonen met maar een hele kleine openingshoek toch individueel kan waarnemen.

Zware quarks kunnen ook gebruikt worden om de verdeling van partonen en gluonsaturatie te meten. De mogelijkheid om quarkonium (een gebonden staat van een zware quark en zijn anti-deeltje) dat vervalst in twee electronen in de voorwaardse richting te meten met de FoCal detector is bestudeerd met behulp van simulaties. Helaas lijkt een quarkonium meting niet mogelijk door de lage opbrengst in de voorwaardse richting en door de aanwezigheid van vervalsfotonen van het neutrale pion, wat leidt tot een lage signaal-achtergrond verhouding. De resultaten van deze simulaties en aanbevelingen om de meting te verbeteren zijn samengevat in paragraaf 7.5.

Prototype

Om het meetprincipe en de mogelijkheden van de FoCal te demonstreren is een volledig digitaal calorimeter prototype gebouwd als R&D project, met state-of-the-art technologie. Het bestaat uit 96 MAPS CMOS sensoren, met een pixel grootte van $30 \times 30 \mu\text{m}^2$, in lagen met daartussen platen wolfram, een materiaal met een zeer hoge dichtheid. Elke gevoelige laag bestaat uit 4 MIMOSA sensoren. Er zijn 3 verschillende typen sensoren in het prototype verwerkt, elk met een andere dikte van de epitaxiale laag. Het prototype heeft 24 lagen en de totale diepte voor electromagnetische showers is $28 X_0$. Het actieve oppervlak is $4 \times 4 \text{ cm}^2$, wat groot

genoeg is om een electromagnetische shower te onderzoeken in de laterale richting, omdat de Molière radius van het prototype erg klein is 11 mm.

Het prototype is getest met kosmische muonen en met deeltjes bundels. Een algoritme om de sporen van minimum ioniserende deeltjes (MIPs) te reconstrueren is ontwikkeld en getest. Een aantal analyses gebaseerd op de gereconstrueerde sporen zijn uitgevoerd:

- Het uitlijnen van de detector is nodig, aangezien de positieonauwkeurigheid na het in elkaar zetten van het prototype enkele honderden micrometers groot kan zijn. Een totaal van 283 vrijheidsgraden zijn bepaald in de uitlijnprocedure. In een iteratief proces worden de verschillen (residuals) tussen de uitgelijnde posities en de gemeten hit posities geminimaliseerd en zijn uiteindelijk kleiner dan $5\ \mu\text{m}$.
- De efficiëntie van de sensoren in het prototype is bepaald met zowel pionen en muonen. Het resultaat hiervan is te zien in Figuur 6.1. De sporen van pionen met een hoge energie geven consistente waarden voor sensoren met dezelfde dikte van de epitaxiale laag. Daarbij is het effect het sterkst te zien aan het begin en eind van het spoor, waar de efficiëntie omlaag gaat. Dit laat de beperking van het sporenreconstructiealgoritme zien.

Data van bundeltesten, uitgevoerd op DESY met elektronen en op CERN met elektronen en pionen, is ook gebruikt om de cascade van deeltjes (showers) te analyseren die zich kan vormen als een elementair deeltje interacties aangaat met het materiaal waar het doorheen beweegt:

- Een unieke methode om een shower te reconstrueren is ontwikkeld en getest. Deze methode gebruikt niet de conventionele methode gebaseerd op de energiedepositie per transversaal segment, maar het gebruikt de digitale informatie van alle lagen tegelijk met een weegfactor die de bijdrage van het centrum van de shower zwaarder mee laat wegen. Door de parameters in Vergelijking 5.2 te optimaliseren kan een positieresolutie kleiner dan $30\ \mu\text{m}$ voor elektronen met een hoge energie bereikt worden (zie Figuur 6.7).
- Een schatting is gemaakt van de contaminatie van pionen in de elektronenbundel. Het aantal pionen is zo klein dat er in de analyse geen rekening mee gehouden hoeft te worden. De verschillen tussen showers van elektronen en pionen zijn vergeleken door naar de longitudinale en transversale richtingen van de shower te kijken in simulaties. Het beginpunt van de shower is bepaald met de methode beschreven in Paragraaf 5.3. Door snedes op de longitudinale en transversale parameters, bij verschillende energieën, kunnen pionen van de elektronen onderscheiden worden (Figuur 6.6). Hierdoor kunnen pionen nog beter onderdrukt worden.
- De selectiecriteria voor de calibratie zijn geoptimaliseerd. De nieuwe calibratiefactoren (Figuur 5.21) verbeteren de energieresolutie voor alle energieën.

Aanbevelingen

Bijna 30% van het detectorvolume is niet bruikbaar door niet functionerende sensoren, kanalen en pixels. Hierdoor is de analyse van de data relatief lastig. De systematische onzekerheid die geïntroduceerd wordt door de data in de niet-functionerende gebieden te extrapoleren, is waarschijnlijk niet te verwaarlozen, maar erg lastig om in te schatten vanwege de fluctuaties

in electromagnetische showers. Ook de ruimte tussen de sensoren in de ene richting, en het overlappende gebied in de andere richting, beïnvloeden het aantal zichtbare hits in de analyse en kunnen ervoor zorgen dat het effectief bruikbare deel van de detector nog kleiner wordt. Om de efficiëntie te berekenen, bijvoorbeeld, moeten deze gebieden uitgesloten worden. Bij het reconstrueren van het centrum van een shower is de nauwkeurigheid in deze gebieden lager, aangezien een deel van de informatie mist (gat tussen de sensoren) of verdubbeld wordt (overlappende sensoren), wat het resultaat kan beïnvloeden. In een verbeterd prototype zouden deze tekortkomingen verholpen kunnen worden.

Muonen laten in een calorimeter alleen maar een spoor achter; ze vormen geen shower. Daardoor kunnen ze gebruikt worden om de calorimeter te testen op het gebied van calibratie, uitlijning en sensor karakterisatie. In de simulaties moet daarom ook een correcte generator van kosmische muonen aanwezig zijn.

De modellen in het simulatieprogramma Geant4 die hadronische processen beschrijven zijn constant in ontwikkeling en worden steeds verbeterd, dit kan de reden zijn waarom er nog verschillen waarneembaar zijn tussen de data van hoog granulaire calorimeters en simulaties. De modellen die electromagnetische processen beschrijven zijn eenvoudiger en beschrijven bestaande data erg goed. Toch zijn er verschillen te zien tussen simulaties en data in de vorm van de showers gemeten met de FoCal, met name in de longitudinale profielen van elektron showers.

Een “physics list” met hogere nauwkeurigheid, FTFP_BERT_EMY, geeft een goede overeenkomst van het maximum van de shower van elektronen in de digitale hadronische calorimeter van de CALICE Collaboratie. Simulaties gebaseerd op deze physics list zouden vergeleken kunnen worden met de uitkomst van de, tot nu toe gebruikte, emStandard lijst.

Het is mogelijk om de gevoeligheid van sommige sensoren in het prototype te tunen. Na het terugwinnen van enige lagen, bijvoorbeeld laag 21, moeten de grenswaarde van de sensoren in deze lagen nog geoptimaliseerd worden. Sommige sensoren bevinden zich in kritische lagen met betrekking tot de ontwikkeling van de electromagnetische shower, maar hebben geen optimale grenswaarden. De sensor in laag 10, positie 0, bijvoorbeeld, heeft een grote invloed op de energieresolutie. Het tunen van de grenswaarde zou de gevoeligheid van deze sensor kunnen verbeteren, en daardoor de totale energiemeting.

De efficiëntie als een functie van de energie, afgebeeld in Figuur 6.1, suggereert dat het type sensor een rol speelt. De gevoeligheid van de sensoren hangt af van de dikte van de epitaxiale laag van de sensor. Dit maakt het tunen van de sensors onstabiel en gecompliceerd.

De ontwikkeling van de showers van hadronen gemeten in het FoCal prototype, kan gebruikt worden voor de ontwikkeling en verbetering van realistische Particle Flow Algoritmes (PFA). Hiervoor is een goed begrip van de interacties van hadronen en het gedrag van de detector onmisbaar.

Het onderscheiden van elektronen en hadronen is bestudeerd. Doordat er voor de SPS data geen efficiënte deeltjesidentificatie aanwezig was, kan de methode maar beperkt getoetst worden. De methode is ook toegepast op simulaties en de resultaten zijn vergeleken met die van de echte data.

Al deze problemen kunnen waarschijnlijk opgelost worden door meer bundeltesten, of door een verbeterd hoog granulair prototype.

Acknowledgments

Time flies! It has been four years since I stayed in this nice and beautiful city. Now the journey of my PhD in Utrecht is close to the end, however, sometimes the first day when I started still comes to my mind.

My deepest gratitude goes first and foremost to my promoter prof. Thomas Peitzmann. Thank you for giving me this opportunity to join the FoCal group to fulfill my dream of developing a state of the art detector. I would like to also thank for your constant encouragement and guidance on the progress of my academic research during these four years.

I would like to express my great thanks to Gert-Jan Nooren, who is my supervisor. I benefited a lot from our regular discussion that we were having during the whole period of my PhD. The discussions were always enjoyable and I was extracting a great deal of useful things from them (not only about the academics, but more from your immense knowledge and experiences in different areas and countries).

Special thanks to the other supervisor Marco van Leeuwen, who has a lot of great ideas (which has been proved in the acknowledgments of all the PhD theses in SAP) to solve no matter academical or technical problems and is always willing to give help and support to me in different situations.

I would like to also thank Ton van den Brink. I would remember all the moments when we were doing the experiments during the test beams at CERN (The training courses for driving and eating “drop”. We went to Mont Blanc, flea markets, and even the “flat tire” of our car). You are not only an excellent technician but also a good friend who can always give the right hand whenever I ask for the help.

Special thanks goes to Martijn Reicher. Thank you for introducing programming to me when I start my studies in this project. I gained a lot from reading the code you wrote for the prototype. All the best my friend.

Elena, it was great to work together with you in the first two years of my PhD. Thank you for your leadership during the test beam and the data which could support my studies go on.

Chunhui, it is hard to find word to describe the friendship between us. I think we will meet each other in the future in China, wish you good luck in your new job my brother.

Naomi, it was really a pleasure to have a officemate like you, although you joined our group during the last a few months of my PhD. I enjoyed a lot to

discuss with you about the problems we found during the analysis and also learned a lot from your experience of working on calorimeter. I would like to thank you for your nice dutch summary!

I would like also to thank people from the ALICE group in Utrecht and Nikhef. Without your help, I would not have been successful to finish my PhD.

回想起来，三十年犹如白驹过隙.....

感谢亲爱的父母三十年来对我的养育、教育。正是这种亲情，凝聚为一种动力，支持我如今能够完成学业。感谢我的岳父岳母，感谢你们对我的支持和包容，感谢我的家人，感谢你们对于后辈的辛勤付出。如今你们已经年过半百，鬓角斑白，而我也初为人父，开始体验到了为人父母的辛劳与点点喜悦。

感谢在Utrecht认识的各位朋友，张育茂、郭勇、孙飞龙、娄博、刘芳、赵玉琰、杨浩然、杨欣、陈晨、袁瑞学、常富强、刘敬洋、毛子丹，正是有了大家的陪伴和鼓励，让我在异国的生活不再孤独。

感谢在Utrecht FC中认识的各位球友，让每周的业余生活充满了期待。感谢陈思毅队长对足球的热情和执着，让这支球队在我们心中拥有了别样的含义。也是在这支球队使我有幸结识了王志雄，牛瑞桃，张曦晨，杨超等几位生活上的朋友。在未来的日子里，我会怀念Lunenten那片绿茵球场和那群训练的背影。

感谢中国原子能科学研究院核物理研究所的各位老师和朋友。尤其感谢黄翰雄、王琦师兄，是你们的担保得以让我顺利出国。感谢阮锡超研究员，聂阳波、刘世龙、张春利师兄，在我博士即将毕业的时候为我的未来的工作出谋划策。感谢鲍杰研究员、苏晓斌、张凯长期以来对我学业的鼓励。

感谢环保部核与辐射安全中心王亮、吴岳雷高级工程师在博士后入站方面为我提供的帮助和支持。正是你们不断的鼓励，让我对未来的工作充满希望。

文永正、孙晨、詹光茂、许世康、周翠进、邹修欢、殷胤、黄伟、李鹏波、余睿、张力、袁国军、查于东、卞伟、韩振义、郭卢阵、李帅、李煦、汪金龙、温凯、郭志文、郑涌、董智勇。感谢各位在四年之中对我的支持和鼓励，我也即将回国与你们并肩奋斗。

王安然，你是我博士期间最大的成果，感谢你带来了这段异国成长的美好回忆，让它伴随我终身。

感谢我的太太纪元，时间让我们彼此成熟了起来，点点滴滴的相伴，星星夜夜的相依，感谢一路有你，也祝福未来的我们。

感谢你们，感谢那些青春里的身影，那些一同为了梦想努力的一幅幅画面，汇成了记忆中最美的电影...

Curriculum Vitae

Hongkai Wang was born on November 4th, 1987 in Jinzhong, Shanxi Province, P. R. China. He developed a strong interest in science since the second year of his high school, then he chose physics as one of the major subjects. In September 2006, he started a bachelor studies in Microelectronics in Sichuan University. In September 2010, he continued the studies at China Institute of Atomic Energy with the master program. During the master program, he focused on fission neutron energy spectrum measurements with nuclear emulsion. After three years, he obtained his master degree in nuclear physics in 2013. He moved to the Netherlands to start as a PhD candidate in the same year under the supervision of Prof. Dr. Thomas Peitzmann, Dr. ir. Gert-Jan Nooren and Dr. ir. Marco van Leeuwen. The results of his research are described in this thesis. On the 15th of January 2018, he will defend the thesis entitled “Prototype Studies and Simulations for a Forward Si-W Calorimeter at the Large Hadron Collider.”.

